



北京大学

# 博士研究生学位论文

**High quantum efficiency photocathode for use  
in superconducting RF gun**

Erdong Wang

Submitted to the Graduate School in partial fulfillment of the  
requirements for the degree of Doctor of Philosophy  
in School of Physics,  
Peking University  
January, 2012

# High quantum efficiency photocathode for use in superconducting RF gun

Erdong Wang (Photocathode and SRF electron gun)

Directed by Prof. Kui Zhao and Prof. Ilan Ben-Zvi

## Abstract

The topic of this thesis is high quantum efficiency photocathode for use in superconducting RF gun. This work was in two areas, studies and tests of cesiated gallium arsenide photocathode in SRF gun and a diamond amplified photocathode. Future particle accelerators, such as the eRHIC and the ILC, require high brightness, high-current polarized electrons. Recently, using a superlattice crystal, the maximum polarization of 95% was reached. Activation with (Cs-O) lowers the electron's affinity and makes it energetically possible for all the electrons excited in the conduction band to reach the surface and escape into the vacuum. Presently, the polarized electron sources are based on DC gun, such as that at the CEBAF at JLab. In these devices, the life time of the cathode is prolonged due to the reduced back-bombardment under their UHV conditions. However, the low accelerating gradient of DC guns leads to poor longitudinal emittance. The higher accelerating gradient of the normal conducting RF gun generates low-emittance beams, but the vacuum cannot meet the requirements of GaAs. Superconducting RF guns combine the excellent vacuum conditions of DC guns with the higher accelerating gradients of RF guns, so potentially providing a long-lived cathode with very low transverse and longitudinal emittance.

The first step undertaken in this research was to prepare a GaAs photocathode with high quantum-efficiency (QE) and long life-time. An ultra-high-vacuum preparation chamber was developed wherein the bulk GaAs was activated. The highest quantum-efficiency attained was 10% at 532 nm. We explored three different ways to activate the GaAs photocathode, and verified that it remained stable for 100 hours in a  $10^{-11}$  Torr vacuum. Passing the photocathode through the low  $10^{-9}$  Torr transfer-section in several seconds caused the QE to drop to 0.8%; this photocathode with its 0.8% QE was suitable for testing with the SRF gun. We also verified the full functionality of the ion back-bombardment in the preparation chamber.

The SRF plug gun was tested first at 2 K without a GaAs photocathode. During the second cool-down, a cathode plug with a GaAs photocathode was inserted in the gun. The Q factor dropped from  $3.0 \times 10^9$  to  $1.78 \times 10^8$  because of the heat losses in the cathode. A model of heat generation is presented; simulating heat flow and the temperature distribution in the working range of the GaAs photocathode reveals that the SRF gun would quench at 6 MV/m. These theoretical results match the experimental measurements well. Following from the findings with the heat-load model, a new cathode holder was designed and fabricated. I discuss a new model, based on the Fokker-Planck equation that estimates the bunch length of the electron beam in the SRF gun. The thesis assessed the temporal response of the GaAs photocathode in the RF field. The tail of the bunch from the GaAs cathode, viz., a critical factor in the performance of a DC gun, can

be ignored in the RF gun. The thesis assessed the effect of ion back-bombardment in the SRF gun that necessitated our developing a new test procedure. The thesis also made a judicious choice of the laser pulse with respect to the RF phase that would minimize the electron back-bombardment.

Assuring a high average-current, high-brightness, and low-emittance electron beam is a key technology for modern accelerator-based science, such as needed for energy-recovery linac light sources, and electron cooling of hadron accelerators. A hydrogen-terminated diamond is a proven efficient electron-emitter that can support the emission of a high average current.

The diamond, functioning as a secondary emitter, amplifies a primary current of a few keV energy coming from a laser-drive photocathode and a DC structure. The surface of one side of the diamond is coated with a metal, like Pt, whilst its other side is hydrogenated to attain a negative electron-affinity surface. Primary electrons penetrate the diamond through the metal coating, and excite electron-hole pairs, the number of which typically is about two orders-of-magnitude more than the number of primary electrons, depending on their energy. Secondary electrons drift across the diamond under an electric field provided by the gun that penetrates the diamond. The secondary electrons reach the hydrogenated surface and exit into the vacuum through the diamond's negative electron affinity (NEA) surface.

My systematic study of hydrogenation resulted in the reproducible fabrication of diamond amplifiers. I compared room-temperature hydrogenation with that at high temperatures and identified the factors leading to the decay of quantum efficiency. The optimum temperature for heat treatment ranged from 400 to 450°C; its superiority was proven in the gain test. Hydrogenated diamond amplifiers exposed to N<sub>2</sub> and air exhibited a good emission after being heated to 350°C; the highest gain we registered in emission scanning was 178. The robustness of the diamond's NEA surface is demonstrated.

Several factors dictate the amplifier's gain: The number of secondary electrons created at their point of entry into the diamond, the fraction of created electrons transmitted to the emitting face, and the fraction of transmitted electrons emitted. I present a model detailing the impact of charge trapping at the surface on the instantaneous electric-field inside the diamond, and its effect on the transmission gain. The ratio of instantaneous emitted electrons to the transmitted electrons depends on the electron's energy distribution and the surface barrier. I calculated the latter by evaluating the magnitude of the negative-electron affinity that is modified by the Schottky effect due to the presence of the external applied field. The instantaneous values then were time-integrated to yield the time-averaged ratio of the number of emitted electrons to the transmitted ones. The findings from the model agree very well with the experimental measurements. As an application of the model, this thesis estimated the energy spread of the electrons inside the diamond from the measured secondary-electron emission.

Key words: GaAs photocathode, SRF electron gun, Particle back bombardment, NEA, Diamond amplifier

## Contents

<b>Chapter 1. Introduction .....</b>	<b>1</b>
1.1. Photocathode polarized electron gun development .....	1
1.1.1. Polarized electron source development .....	1
1.1.2. The requirement of polarized electron source for collider in future.....	2
1.1.3. RF Polarized electron gun development.....	3
1.2. Introduction and development of high current electron source for use in ERL.....	7
1.2.1. The opinion of photocathode for high current electron source .....	7
1.2.2. The concept of diamond amplifier .....	8
1.2.3. Diamond amplifier development.....	10
1.3. The main content and innovations of this thesis .....	11
1.3.1. The purpose of this thesis .....	11
1.3.2. The main content.....	11
1.3.3. The innovations.....	12
<b>Chapter 2. GaAs photocathode activation.....</b>	<b>14</b>
2.1. GaAs photocathode.....	14
2.1.1. GaAs properties.....	14
2.1.2. Negative electron affinity photocathode.....	16
2.1.3. Strained GaAs.....	18
2.2. UHV preparation chamber .....	20
2.2.1 UHV photocathode preparation chamber .....	20
2.2.2 Loadlock system .....	21
2.2.3 UHV achievement.....	23
2.3. GaAs photocathode activation.....	24
2.3.1 Procedures for activating GaAs cathodes .....	24
2.3.2 Photocathode life time measurement.....	33
2.3.3 Ion back bombardment in vacuum chamber.....	35
<b>Chapter 3. The physics of GaAs photocathode SRF electron gun.....</b>	<b>37</b>
3.1. SRF electron gun .....	37
3.1.1. SRF gun properties.....	37
3.1.2. BNL 1.3 GHz SRF plug gun characteristic parameters.....	38

3.1.3.	SRF cavity properties .....	42
3.2.	Heat generation from GaAs photocathode SRF gun.....	47
3.2.1.	SRF gun test in 2 K .....	47
3.2.2.	GaAs crystal heat generation in SRF gun .....	53
3.2.3.	GaAs photocathode holder design.....	57
3.3.	Temporal response of GaAs photocathode in RF gun .....	61
3.4.	Electron back bombardment in RF gun.....	65
3.4.1	Electron back bombardment in RF gun .....	65
3.4.2	Multipacting in BNL plug gun.....	67
<b>Chapter 4 Diamond amplifier fabrication .....</b>		<b>73</b>
4.1.	Diamond amplifier characteristic properties .....	73
4.1.1.	Diamond properties .....	73
4.1.2.	The concept of diamond amplifier .....	75
4.2.	Diamond amplifier preparation.....	77
4.2.1.	Metallization .....	77
4.2.2.	Hydrogenation.....	78
4.3.	Optimized hydrogenation procedure.....	80
4.3.1.	Spectral response of hydrogenated diamond .....	80
4.3.2.	Hydrogen cracker power .....	82
4.3.3.	Surface cleaning.....	82
4.3.4.	High temperature hydrogenation.....	83
4.3.5.	Lifetime measurement .....	85
4.3.6.	Heat treatment.....	88
<b>Chapter 5. Emission mode measurement of diamond amplifier .....</b>		<b>90</b>
5.1.	Measurement setup .....	90
5.1.1.	Primary electron beam.....	90
5.1.2.	Diamond holder .....	91
5.1.3.	HV push-pull switch circuit.....	92
5.2.	Secondary electron beam emission .....	92
5.2.1.	Short pulse measurement.....	92
5.2.2.	Robustness of diamond amplifier.....	98

5.2.3.	Uniformity of secondary electron emission .....	99
5.2.4.	Reproducibility .....	101
5.3.	Secondary electron surface trapping and emission .....	101
5.3.1.	Emission probability.....	101
5.3.2.	Derivation of the time-dependent internal field .....	103
5.3.3.	Transmission gain function.....	104
5.3.4.	Schottky effect on the effective negative electron affinity .....	105
5.3.5.	Energy spread of secondary electron beam .....	108
5.3.6.	Solving the Integral equation .....	110
5.3.7.	The energy spread due to the IMFP .....	113
<b>Chapter 6. Conclusion .....</b>		<b>116</b>

## Chapter 1. Introduction

### 1.1. Photocathode polarized electron gun development

#### 1.1.1. Polarized electron source development

Polarized electrons are used in experiment of high energy physics and studies of surface physics. The ideal polarized electron source's characteristics include high polarization, high average current, excellent beam quality, short temporal response and long life time. Semiconductors of the III-V family such as GaAs can generate high polarization electron beam by illuminating the photocathodes with circularly polarized laser with certain wavelength due to their energy band structure. Cesium GaAs can achieve very high quantum efficiency due to the negative electron affinity surface. The polarized electron beams are accelerated by DC field or RF field to reach enough high energy. The devices provide such beams called polarized electron gun. In recent years, laser induced photoemission from GaAs were widely accepted by big collider accelerator due to its capability to make the production of high intensity, high polarization and low emittance electron beam.

In the beginning of 1970s, the idea of GaAs based polarized electron source was proposed by E. L. Garwin #. Since D. T. Pierce and colleagues built the first such source in the mid 1970s [1], numerous polarized sources for accelerators have grown of this type, such as CEBAF at JLab [2], Bates at MIT [3], ELSA at Bonn Univ. and MAMI at Mainz [4]. Today, only Bonn-ELSA, CEBAF and Mainz microtron continue to provide polarized electron beams. Table 1 shows a list of accelerator-based polarized electron sources past and present.

GaAs photocathodes have a drawback associated with the UHV ( $<10^{-11}$  torr) required for their operation [5]. Presently, the polarized electron sources are based on DC gun. In these devices, the life time of the cathode is extended due to the reduced back bombardment in their UHV conditions. However, the low accelerating gradient of the DC guns lead to poor longitudinal emittance and low peak current. The higher accelerating gradient of the RF gun generates low emittance beams. However, the extremely high vacuum required by these cathodes cannot be met in a normal conducting RF gun. The typical vacuum of the normal conductor RF guns are low  $10^{-10}$  torr due to out gassing from the copper wall.

Table 1.1: The polarized electron sources in the world

Laboratory	Photocathode	Polarization	Voltage	Beam structure	Pulse charge	Average current
JLAB(CW) [6]	GaAs-GaAsP superlattice	85%	100 kV	35 ps @ cw: 1497 MHz	0.13 pc	200 uA
SLAC_SLC	GaAs-GaAsP	86%	120 kV	2 ns pulses	16 nC	2 uA

[7]	superlattice			@ 120 Hz		
MAMI_Mainz [4]	AlGaAs/InAlGaAs superlattice	85%	100 kV	2450 MHz: CW	0.02 pC	50 uA
Bonn-ELSA	AlGaAs/InGaAs superlattice	80%	50 kV	<a href="#">1 us @ 50 Hz</a>	100 nC	5 uA
MIT-BATES [3]	strained GaAsP	70%	60 kV	<a href="#">25 us @ 600 Hz</a>	250 nC	120 uA
Nagoya [8]	GaAs-GaAsP superlattice	92%	200 kV	N/A	N/A	N/A
NIKHEF [9]	Strained InGaAsP	80%	100 kV	2 us pulses @ 1 Hz		0.04 uA

### 1.1.2. The requirement of polarized electron source for collider in future

Future collider accelerators such as eRHIC and International Linear Collider (ILC) require much high brightness polarized electron beam[10, 11].

The ILC is a proposed linear  $e+e^-$  collider for studying new physics beyond the Standard Model. The maximum center of mass energy is 500 GeV. Physics runs are possible for energy range of 200 GeV to 500 GeV. The electron beam's polarization must be larger than 80% and positron source should be able to generate a beam with polarization more than 50%. To achieve the design luminosity of  $2 \times 10^{34} \text{ cm}^{-2}\text{s}^{-1}$ , the nominal beam parameters at the IP listed as follows: normalized emittance at IP is 10 mm-rad (x) / 0.04 mm-rad (y), RMS beam size is 640 nm(x) / 5.7 nm (y), RMS bunch length is 300  $\mu\text{m}$  [11].

The ILC polarized electron beam plan to be produced by a laser illuminating a photocathode in a DC gun. Normal conducting structures are used for pre-acceleration to 76 MeV before accelerating by a superconducting linac. The SLAC polarized electron source developed for the SLC already meets the requirements of ILC for polarization, charge and lifetime. The DC gun creates a 140-160 keV electron beam with charge of 4.5-5 nC with a bunch length of 1 ns. After the pre-acceleration, the normalized RMS emittance of 76 MeV beam is 70  $\mu\text{m}$ -rad. The emittance of the beam is much larger than the one at IP required for luminosity production. So ILC damping ring accept  $e^-$  and  $e^+$  beams with large transverse and longitudinal emittances and produce the low emittance beams. The ILC damping rings include one electron and one positron ring, each 6.7 km long and operating at a beam energy of 5 GeV[11].

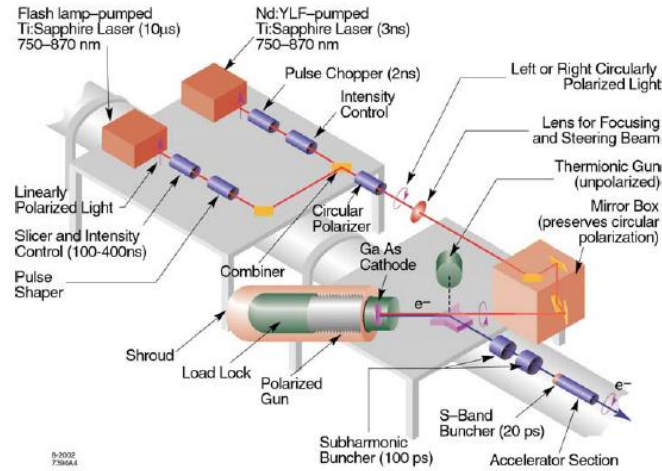


Figure 1.1: The sketch of DC polarized electron gun in SLC.

The RF electron guns can produce much high brightness beams than DC electron guns due to the high field gradient at the emission surface of cathode and could be used as injector for the ILC requiring good emittance. By PARMELA simulation, the RF gun is capable of producing an electron beam with the vertical emittance requirements by a factor of 2 without a damping ring. An ellipsoid charge distribution was used in the simulation [12]. With the RF gun as the polarized electron source, the ILC project saves lots of money if the damping ring can be avoided.

### 1.1.3. RF Polarized electron gun development

The first RF photocathode gun operated at Los Alamos National Laboratory in 1985. In the early 1990s, the SLAC gun test facility was initiated to test and develop the high gradient laser driven RF photoinjector. By collaboration involving BNL, SLAC and UCLA, the 1.6-cell S band RF gun used in the SLAC XFEL operate successfully (Figure 1.2). The measured projected emittance of  $1.2 \mu\text{m}\text{-rad}$  at 1 nC bunch meets the design requirement of LCLS [13].

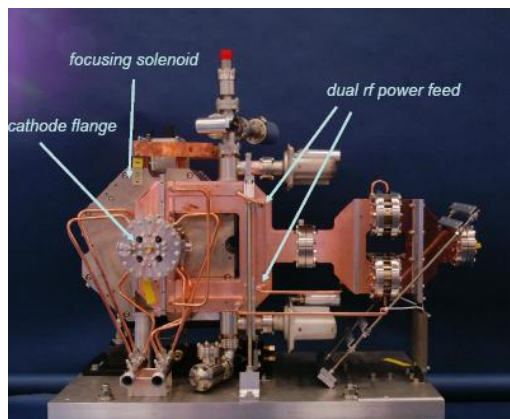


Figure 1.2: BNL/SLAC/UCLA 1.6-cell S band normal conducting RF gun.

A first RF gun with GaAs photocathode was built and tested at Novosibirsk. The large dark current observed is very high in the experiment. The initial QE of GaAs photocathode in the RF gun is 0.94%. Lifetime of a cathode is only 10s of pulses when the repetition rate of RF pulses is 0.5 Hz. The scientists consider that back bombardment of a cathode in RF gun combined with large secondary electron yield from NEA surface can be responsible for the short lifetime. The intense gas release from metal is also responsible in the process [14].

Two different methods may improve the vacuum close to the photocathode. One is to increase the conductance for pumping or other way to improve the operating vacuum closed to the photocathode in normal conducting RF gun. Another way is to improve the vacuum by using the superconducting RF (SRF) gun due to cryogenic pumping.

To reduce the out gassing from RF gun, the scientists from Fermi Laboratory cooled the RF gun to liquid nitrogen temperature [15]. The vacuum pressure measured  $5.8 \times 10^{-10}$  torr in the cold gun when RF was applied. The gun outgases a factor of five less when compared to the warm gun. But still didn't meet the requirement of GaAs photocathode operation. Very high dark current also observed in the test.

The plane wave Transformer (PWT) gun provides a large vacuum conductance and strong cell to cell coupling [16]. The accelerating cell consists of iris loaded disks suspended by cooling pipes in a large cylindrical tank to increase vacuum conductance (Figure 1.3). The  $10^{-11}$  torr vacuum level and its ability to provide excellent beam quality at low accelerating gradient make the PWT gun another choice for a normal conducting RG polarized electron gun for ILC. The simulation by ASTRA shows the normalized transverse emittance is 1.7  $\mu\text{m}\text{-rad}$  when the bunch charge is 3.2 nC.

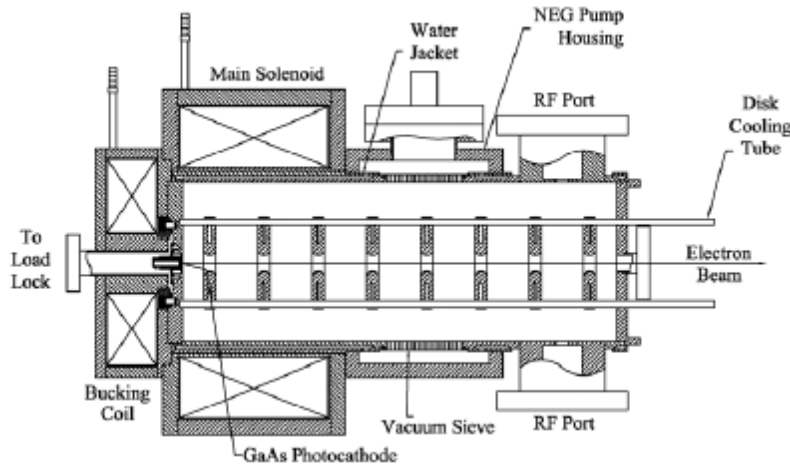


Figure 1.3 Schematic of an L-band PWT polarized electron photoinjector

J. W. Wang and coworkers presented a new RF design which incorporates a higher order mode (HOM) structure for an L-Band normal conducting RF gun for the ILC polarized electron source (Figure 1.4). The gas conductance is improved by adopted a single cell operated in a HOM TM012 which is effectively the RF equivalent of a 1.5 cell structure but without the internal iris. The shape of the gun is shown in Figure 1.3. The beam properties simulation and gun design optimization is still undergoing [17].

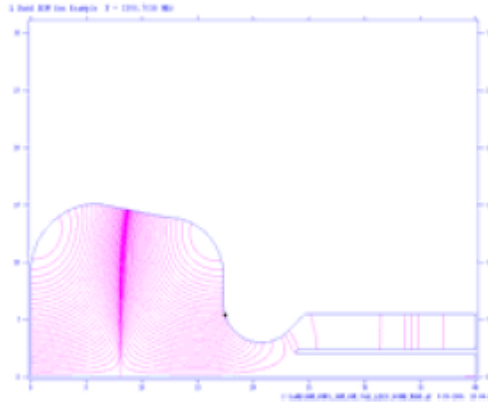


Figure 1.4 Design example for an HOM RF gun

Besides three types of normal conducting RF gun described above, SRF gun can achieve very good vacuum due to increase pumping speed in cryogenic temperature. The superconducting Nb cavity wall absorbs residual gas such as hydrogen in 2 K. In the ultra high vacuum system such as  $10^{-11}$  torr vacuum level, the hydrogen occupy more than 90% of the residual gas. Figure 1.5 shows the variation of vapor of hydrogen with temperature [18]. The limitation of hydrogen vapor pressure is lower than  $5 \times 10^{-15}$  torr, when the temperature cool down to 2 K. With a appropriate vacuum system design, the vacuum in the SRF gun is much better than required for GaAs long lifetime operation. Meanwhile, the advantages of SRF injector are high average current due to continuous wave (CW) mode operation, low emittance due to very high gradient on the cathode.

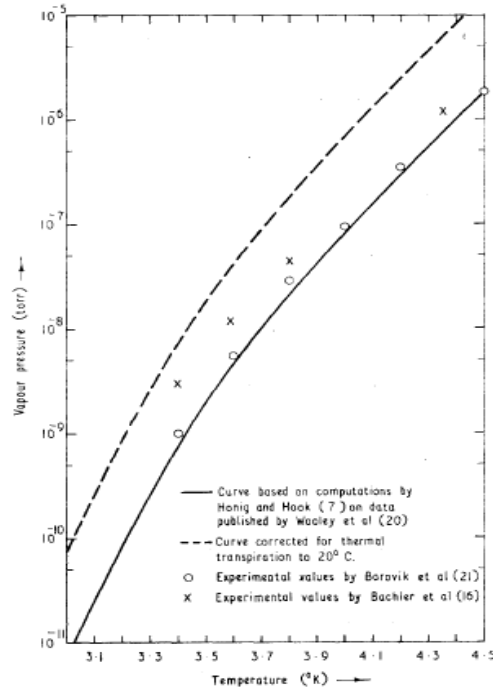
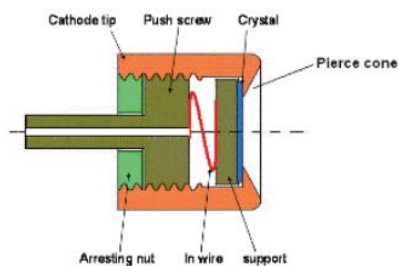
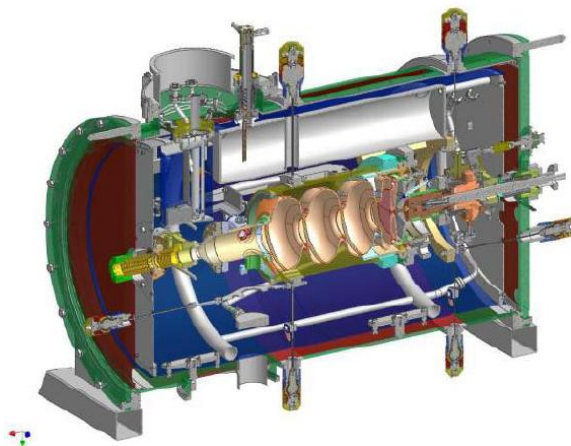


Figure 1. Variation of vapour pressure of hydrogen with temperature.

Figure 1.5 Variation of vapor pressure of hydrogen with temperature

The 1.3 GHz 3.5-cell SRF photoinjector has been tested and operated at FZD successfully.  $\text{Cs}_2\text{Te}$  is used in the FZD SRF gun for requirement of high bunch charges and high average current [19]. A choke cavity is adopted to insulate the thermal conduction between normal conducting photocathode and superconducting cavity. The photocathode is cooled by liquid nitrogen individually (Figure 1.6). FZD SRF gun with a GaAs type photocathode for polarized/non-polarized electron beam also proposed. The simulation shows the RMS normalized emittance is  $1.4 \mu\text{m}\text{-rad}$  when the bunch charge is  $0.77 \text{ nC}$ . The vacuum of preparation chamber has to be improved to suitable for GaAs photocathode activation.



The new cathode head design for GaAs. Image courtesy of FZD

Figure 1.6: Left - the 3D model of FDZ SRF gun; Right - cathode head design for GaAs.

## 1.2. Introduction and development of high current electron source for use in ERL

### 1.2.1. The opinion of photocathode for high current electron source

Assuring a high average-current, high-brightness, and low-emittance electron beam is a key technology for modern accelerator-based science, such as ultra-high-power free electron lasers [20], energy-recovery linac light sources, and electron cooling of hadron accelerators [21, 22]. Thermionic cathode such as  $\text{CeB}_6$  is chosen to generate electron beam for many FEL facilities [23]. The advantages of thermionic cathode are very stable against contamination and uniform emission density. However, the bunch from the thermionic cathode has a long tail. The gradient and the temperature limit the emission current. So the peak current and longitudinal emittance cannot meet the requirement of high current ERL. The photocathode electron gun already demonstrated to provide high brightness, low emittance electron beam. Obtaining high average currents from the photocathodes, such as metallic- and semiconductor-photocathodes requires a high QE and/or very powerful lasers. The metallic photocathodes such as copper and magnesium used in normal conducting RF gun to provide high peak current, low average current and femtosecond electron beam for FEL [24]. The QE of metallic photocathode is lower than 0.2% and only excite by the UV laser. It is hard to realize high average current electron beam due to limitation by the laser power. High QE semiconductor photocathodes such as  $\text{Cs}_2\text{Te}$ ,  $\text{K}_2\text{CsSb}$ , V-III semiconductor must be prepared and maintained in an ultra-high-vacuum system. Even a photocathode with an extremely good QE of 10% places several practical demands on a powerful drive laser; thus, 10s of watts of average power at visible and near-IR wavelength spectrum are needed, along with a pulse duration of sub-picoseconds to tens of picoseconds, and a pulse-recurrence frequency ranging from hundreds of kHz to hundreds of MHz. Even now, it is hard to accommodate such power levels on the drive lasers along with the requirement for a high repetition rate ( $\sim\text{GHz}$ ). Figure 1.7 shows the different cathodes and laser power response to the requirement of average current [25].

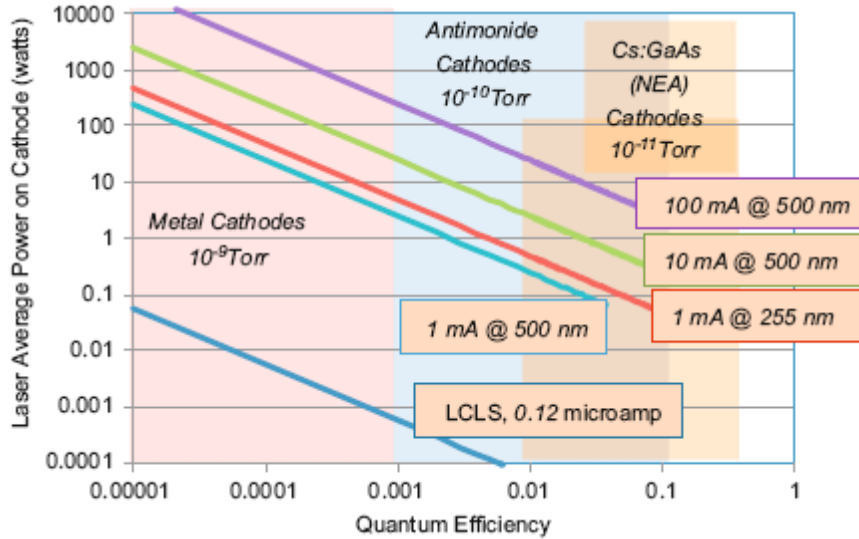


Figure 1.7: The average laser power vs quantum efficiency to produce various average current.

To achieve 100 mA average beam current for ERL, Only Cs:GaAs or  $K_2CsSb$  can be chose but didn't be demonstrated yet. Table 1.2 shows the parameters of photocathodes for high average electron beam current.

Table 1.2: Photocathodes for high average current photoinjector

	Laser (nm)	QE	Vacuum (torr)	Thermal emittance (um-rad)	Laboratory	Gun type
$K_2CsSb$	543	10%	$10^{-10}$	0.4	BNL, ANL, JLAB, Cornell, LANL, Boeing	RF / SRF / DC
GaAs (Cs, F)	532	15%	$10^{-12}$	0.8	JLAB, Cornell, ALICE, BNL	DC
Diamond Amplifier	N/A	Gain>100	$10^{-9}$	N/A	BNL, LBNL	RF / SRF

### 1.2.2. The concept of diamond amplifier

The diamond amplifier was first proposed by Dr. Ilan Ben-Zvi in 2004 [22]. It is a novel electron source which may provide a high average current, low emittance beam with long operation lifetime. The diamond, functioning as a secondary emitter, amplifies the primary current of a few keV energy that come from a laser-driven photocathode and a DC structure. The surface of one side of the diamond is coated with a metal, like Pt, whilst its other side is hydrogenated to attain a negative electron-affinity surface. Primary electrons penetrate the diamond through the metal coating, and excite electron-hole pairs, the number of which typically is about two orders-of-magnitude more than the number of

primary electrons, depending on their energy. Secondary electrons drift across the diamond under an electric field provided by the gun's electrical field that penetrates the diamond. The holes drift back to the metal side and are absorbed by the ground as the secondary electrons reach the hydrogenated surface and exit into the vacuum through the diamond's negative electron affinity (NEA) surface. Assuming the average primary current is 10mA, the average secondary electron current achieve 1 A if the gain of diamond amplifier is higher than 100. Figure 1.8 shows one capsule design of the diamond amplifier with photocathode which provides the primary current.

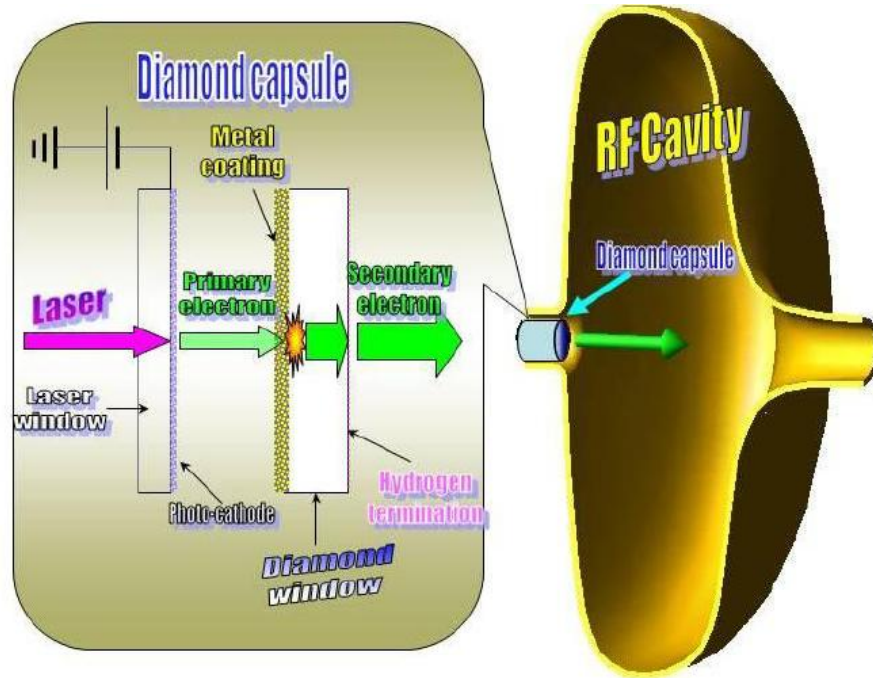


Figure 1.8: One capsule design of diamond amplifier with photocathode.

The advantages of diamond as the secondary emit are listed as the follows [26]:

1. Wide band gap and indirect band gap

Diamond is an indirect band gap semiconductor with a band gap of 5.47 eV. The probability of electron in the conduction band annihilates a hole in the valence band dramatically reduce due to the indirect band gap. The semiconductor with larger band gaps can hold very strong electric field. The diamond can hold up to 2 GV/m electric field, so it is a candidate material to use in RF gun. The high electric field also prevents recombination between electrons and holes, meanwhile, speeds up the electron to saturate velocity. With hydrogenation, the diamond surface forms a NEA mono-layer without heave *p*-dope.

2. Rigidity

The SRF cavity is sensitive to the contaminations from the photocathode. The rigidity of diamond allow it insulate the vacuum between cavity and photocathode as a thin window.

3. Very high thermal conductivity

Several heat sources deposit the power on the diamond amplifier such as primary electron bombardment, dielectric heat load from diamond, electron phonon scatter, RF field shielding on the metal layer and resistive heating from metal layer. As a very good thermal conductivity material, the power deposited on the diamond can easily flow out without large temperature change.

4. Very high mobility

The saturate drift velocity of the electrons on conduction band in diamond is  $1.5 \times 10^7$  cm/s and relatively independent of temperature when the inner electric field above 1 MV/m [27]. the characteristic of high drift velocity is indispensable for high radio frequency application.

1.2.3. Diamond amplifier development

The experiments demonstrated the high gain secondary electrons generation and electrons transport in the diamond done by Dr. X. Chang and Dr. W. Qiong [28]. In transmission mode measurement, the diamond amplifier was coated with 40nm metal layer on both sides. One side metal coating is connected to the ground through a current meter. Another side metal coating is connected to a high voltage power supply. Primary electrons beam are generated from a thermionic gun. The transmission gain was measured as a function of the electric field for a few primary electron energies. The setup of transmission mode measurement is shown in figure

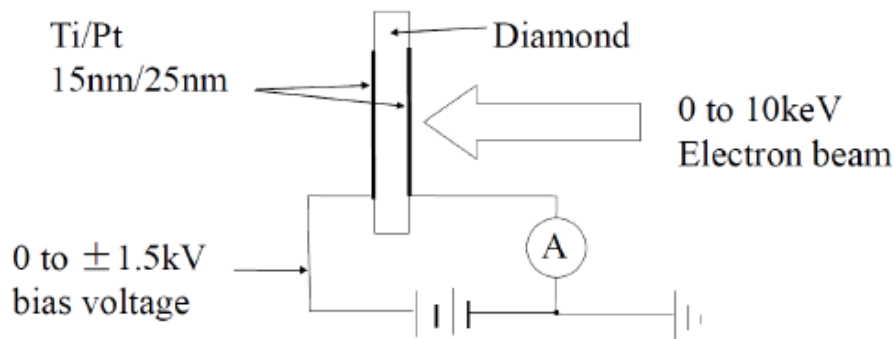


Figure 1.9: Sketch of the transmission mode measurement setup.

The secondary electron yield for transmission mode measurement provides the value of the average energy of the primary electrons required to generate one electron hole pair on the diamond. The gain is more than 200 for 4.7 keV primary electrons above 1 MV/m of gradient inside the diamond. The gain diamond is independent of the density of primary

electrons. By replacing the primary electron beam with an X ray beam, the diamond can deliver up to an average current density more than  $100 \text{ mA/mm}^2$ . The peak current density in X ray transmission mode measurement was larger than  $400 \text{ mA/mm}^2$  [29]. These values are enough for most applications that require a high brightness and high average current source.

In their basic emission mode measurement, a secondary electron yield of 20 was got in very short period. These results show good trend toward high emission gain electron source.

### 1.3. The main content and innovations of this thesis

#### 1.3.1. The purpose of this thesis

Based on the requirement of ILC project, several laboratories are developing the GaAs photocathode RF gun. But none of them are successful. The photocathode RF gun group of Brookhaven laboratory proposed generating the polarized electron beam from GaAs based on the superconducting RF gun. The 1.3 GHz 0.6-cell SRF plug gun with GaAs photocathode was tested and the performance was analyzed in this thesis.

There are several issues mentioned about GaAs photocathode used in a SRF gun [30].

1. Maintain the vacuum inside the gun better than  $10^{-11}$  torr to reduce the intense of ion back bombardment.
2. Reduce the dark current due to the field emission.
3. The bunch tail may damage the photocathode due to the electrons in back bombardment phase.
4. The heat load from the GaAs in RF field.
5. The welding material such as indium may affect the performance of SRF cavity.

High average current and high brightness electron source is one of the most difficult parts in development of ERL facility. However, there have been few improvements in photocathode technology in recent years. The diamond amplifier has big progress since it was proposed. There are several issues such as fabricate procedure, emission theory and beam quality still have to study.

Based on the background introduced above, issues generated from the GaAs photocathode combine with SRF gun are studied in this thesis. Meanwhile, the beam energy spread from diamond amplifier is estimated. The treatments developed by this thesis result in a reproducibly better performance of diamond amplifiers.

#### 1.3.2. The main content

Chapter 1 reviews the polarized electron sources in the world and list four different places developing the GaAs RF gun. Also included in this chapter are review the high average current electron source and introduce a novel photocathode diamond amplifier. Then this chapter describes the content and innovation of this thesis

Chapter 2 describes GaAs properties relevant to photoemission and a preparation chamber for GaAs photocathode activation. This chapter discusses the different procedure to activate the GaAs photocathode and QE life time measurement in the different situation.

Chapter 3 studies the issues generated from the combining of GaAs photocathode and SRF gun such as the heat load in the RF field and multipacting due to the electron back bombardment. The temporal response of GaAs photocathode is estimated by a drift diffusion equation in this chapter.

Chapter 4 starts the discussion of the diamond properties and diamond amplifier fabrication procedure. Special emphasis is placed on the hydrogenation optimization. The residual gas affects on the life time of diamond amplifier also studied in this chapter.

Chapter 5 includes results of diamond amplifier continuous emission test. The secondary electron surface trapping mechanism also discussed. The emission probability of the diamond amplifier as a function of the external field is measured and the process with the resulting changes in the vacuum level due to the Schottky effect is modeled in this chapter. The effective NEA is deduced from the model and measurements. As an application of the model, this chapter estimate the energy spread of the electrons inside the diamond from the measured secondary-electron emission.

Chapter 6 summarizes the results of this thesis.

### 1.3.3. The innovations

The innovations of this thesis are listed as the follows.

1. The author tested the SRF gun with GaAs photocathode in 2 K and did simulations of various heat load mechanisms when the cathode is placed in the strong RF field. Design a photocathode base to eliminate the heat generation from the GaAs photocathode.
2. The author calculated the limitation of the temporal response of the GaAs photocathode in RF field.
3. The author wrote a program to simulate the multipacting mechanism due to the electron back bombardment.
4. The author studied the hydrogen termination process of diamond systematically that led to diamond amplifier fabrication high gain and reproducible

The author tested several high gain diamond amplifiers in emission mode and calculated the surface barrier by evaluating the magnitude of the NEA that is modified by Schottky effect due to the presence of the external applied field. The electron spread was estimated by the emission model that developed by author.

## Chapter 2. GaAs photocathode activation

### 2.1. GaAs photocathode

Laser drive photocathode electron gun has been demonstrated to generate electron beam with low emittance, high brightness and short bunch length[31]. The photocathode is the key part for the photocathode electron gun.

Semiconductors of the III-V family have ability of high photo absorption rate, long diffusion length, so these semiconductors are one of the best electron emitter. After P doped of III-V family semiconductor, the impurities to the semiconductor changes the surface potential a lot. The Fermi level of semiconductor which depends on the doping concentration will be close to the valence band after heavy P doping. In particular, GaAs is one of the most widely used photocathode due to its large direct bandgap. The theoretical maximum polarization obtainable from GaAs is 50% driven by 1.42eV right or left hand circular polarized laser[1]. Nakanishi concluded that optimized strained GaAs resulted in an 86% polarization in 1990[32]. The KEK/Nagoya group tested a superlattice GaAs also generated more than 80% polarization electron beam[33].

#### 2.1.1. GaAs properties

The GaAs is a compound of the elements gallium and arsenic. It has a zincblende lattice structure. Table 2.1 shows some reference values of the GaAs.

**Table 0.1 The reference values of GaAs[34]**

Gallium	Z=31, III
Arsenic	Z=33, V
Lattice constant	5.65Å
Angle between bonds	109.47°
Density	5.32g/cm <sup>3</sup>
Atomic density	4.5×10 <sup>22</sup> 个/cm <sup>3</sup>
Specific heat capacity	0.327J/g-K
Relative permittivity	12.85
Band gap	1.42eV

Thermal conductivity	0.55W/cm-°C
Melting point	1238°C

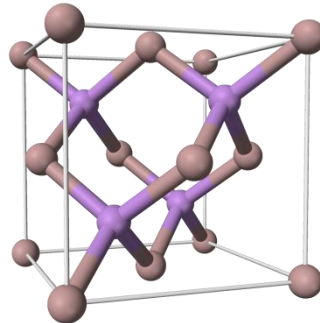


**Figure 2.1 GaAs crystal lattice**

In solid state physics, the band theory models the behavior of electrons in solids by the existence of energy bands. Most semiconductors include conduction band and valence band. The region between these two bands is forbidden to exist any states. The gap between the low point of conduction band and the high point of valence band called band gap. The electrons excited to the conduction band can current flow in the crystal[35]. Figure 2.2 shows the energy band diagram for GaAs[34].

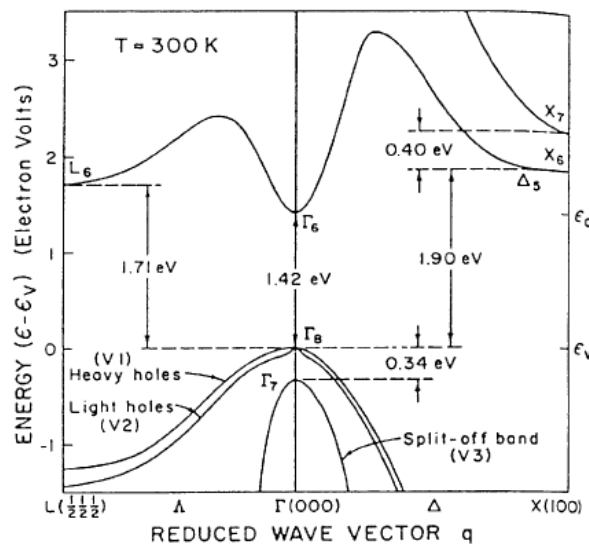


**Figure 2.2 GaAs energy band diagram**

**Figure 1.2 shows the top of the valence band and the bottom of conduction band occur at the  $\Gamma$  point in GaAs. It is a direct band gap semiconductor. The top two valence bands known as the heavy hole band and light hole band are degenerate. It leads to a fact that the GaAs generate theoretical 50% polarization electron beam.**

The band gap energy in semiconductor is related to the temperature. This relativity affect the drive laser wavelength which excite the polarized electron beam. The dependence of band gap energy on the temperature is given by[36]

$$E_g(T) = E_g(0) - \frac{\alpha T^2}{T + \beta} \quad (2.1)$$

where T is the temperature of the GaAs. For GaAs,  $\alpha$  is  $5.4 \times 10^{-4}$  and  $\beta$  is 204. In the room temperature, the energy band is 1.422eV. In 2K, the energy band of GaAs is 1.519eV.

The superconducting RF gun usually operate in the temperature of 2K, the driven laser should be different with DC gun.

#### 2.1.2. Negative electron affinity photocathode

The electrons emission from photocathode can be explained and formalized by the three step model developed by W. Spicer in 1960s. The three steps consist of electron excitation to conducting band, electrons transport and electrons emission to vacuum[37].

In the first step, the photos with energy above the band gap of semiconductor can excite electrons from valance band to the conduction band. The number of electrons excited at various depths from the surface is proportional to the intensity of driven light.

In the second step, the electrons excited to the conduction band scatter with phonons and thermalize as they approach the surface. To increase the quantum efficiency, the long scattering distance material is chosen such as GaAs. The electron-electron scattering is significant in metal photocathode but negligible in semiconductor photocathode. The second step determines the response time for photocathode due to long time required by electron transport.

In the third step, the electrons that reach the surface with sufficient energy have a certain probability of emission. Here, we define the electron affinity as the energy difference between the vacuum energy and the conduction band minimum. The probability of emission of electrons is increase by electron affinity drop. For the vacuum level lies under the conduction band minimum semiconductor such as GaAs, the emission probability can achieve 100%. Furthermore, we define the work function as the energy difference between the Fermi level and vacuum level. The electrons on the Fermi level can excited to the vacuum level by thermal activation. The dark current is relative to the work function. The ideal photocathodes have small electron affinity with large work function. Fig 2.3 shows the three step model in solid.

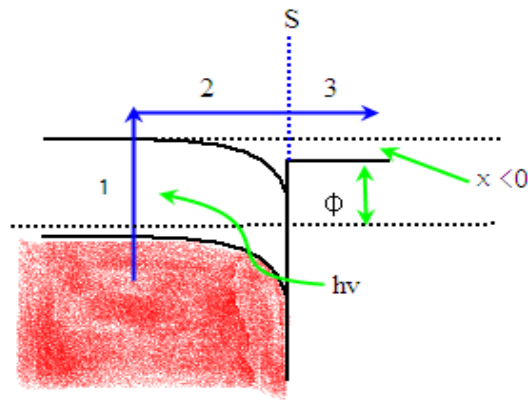


**Figure 2.3 The three step model use in NEA photocathode**

In the three step model, the third step is relative to photocathode surface. The emission probability is determined by two conditions after electrons transport to emission surface.

1. Band bending region at surface

The Fermi level is pinned at the surface near the middle of the bandgap by surface states causing a band bending region to be formed. The depletion region thickness is determined by [38]

$$l = \sqrt{\frac{2\varepsilon V_{bb}}{qN_a}} \quad (2.2)$$

Where  $V_{bb}$  is potential of energy bending,  $\epsilon$  is permittivity and  $N_a$  is the impurity concentration. The wide depletion region reduces the probability of escape during photoemission due to electron phonon scattering rate increase. The depletion region can be short by increase doping concentration. The high doping concentration reduces the diffusion length and cause electron spin relaxation. To find the balance, the typically p doping level is in the range of high  $10^{18}$  to low  $10^{19}$   $\text{cm}^{-3}$  so that the resulting depletion region thickness at the surface is  $100\text{\AA}$  or less [38].

## 2. Cesium oxide layer

Apply monolayer quantities of cesium to a clean GaAs surface can reduce the electron affinity. J. Scheer and J. Laar first got nearly zero electron affinity from GaAs (110) surface by Cs activation at 1965[39]. Even lower electron affinity can be obtained by using addition of oxidant such as oxygen or  $\text{NF}_3$ . A. Sommer found the negative electron affinity from cesium oxider monolayer activated GaAs sample at 1970. The heavily p type doping GaAs is required for above process. Figure 1.4 shows the bend structure near GaAs surface.

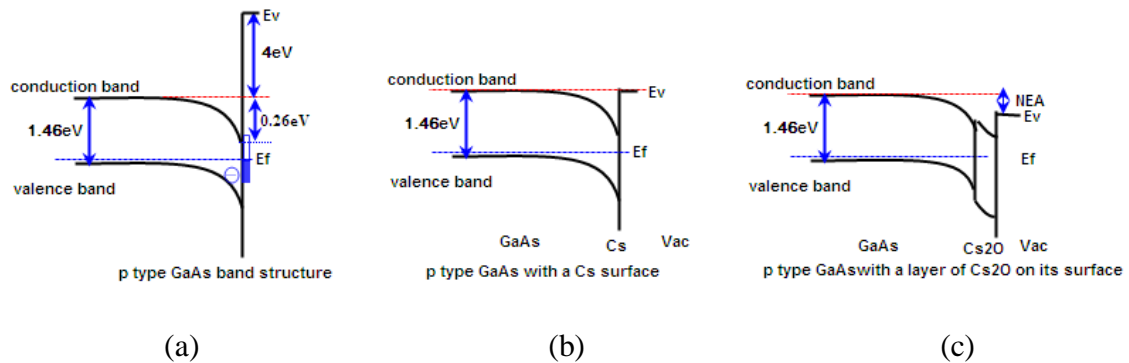


**Figure 2.4 The band structure of GaAs near the surface. a) Heavily p doped GaAs. b) Zero electron affinity surface of cesiated GaAs. c) Negative electron affinity surface of GaAs with  $\text{Cs}_2\text{O}$  monolayer.**

### 2.1.3. Strained GaAs

The first polarized source based on photoemission from GaAs was developed by Sinclair at SLAC[1]. The band structure of GaAs shows the spin-orbit coupling splits the valence band into  $p_{3/2}$  and  $p_{1/2}$  with a residing band  $\Delta=0.34\text{eV}$  at the  $\Gamma$  point. Electrons are considered polarized when the two possible spin states along a particular direction are not evenly populated. The selection rules for right and left hand circular polarized light incident to the GaAs surface are  $\Delta m_j=+1$  and  $-1$ , respectively. The band gap of GaAs is  $E_g=1.46\text{eV}$ . If the GaAs is illuminated with circularly polarized light of an energy between  $E_g$  and  $E_g+\Delta$ , the polarized electron will occur.

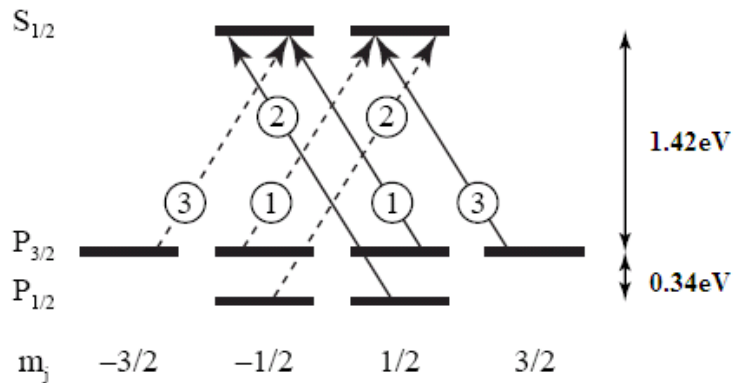


**Figure 2.5 The energy level diagram of GaAs with electromagnetic transitions. The number in the circles shows the relative probabilities of the transitions. The solid and dashed lines distinguish transitions made by different polarized direction light.**

Figure 2.5 shows the relative probabilities of the transitions which are given by Clebsh-Gordan coefficient. For the bulk GaAs, the ideal polarization of electrons excited to the conduction band is  $(3-1)/(3+1)=50\%$ . The lattice imperfections and inelastic scattering of polarized electrons result in depolarizing effects, generally limit the polarization to around 40%[40]. Even higher polarizations can be achieved by strain the GaAs crystals mechanically. The strain break the degeneracy of heavy hole states and light hole states in the  $P_{3/2}$  valence band and generate one type of spin state. The ideal polarization of electrons from strained GaAs is 100%[32].

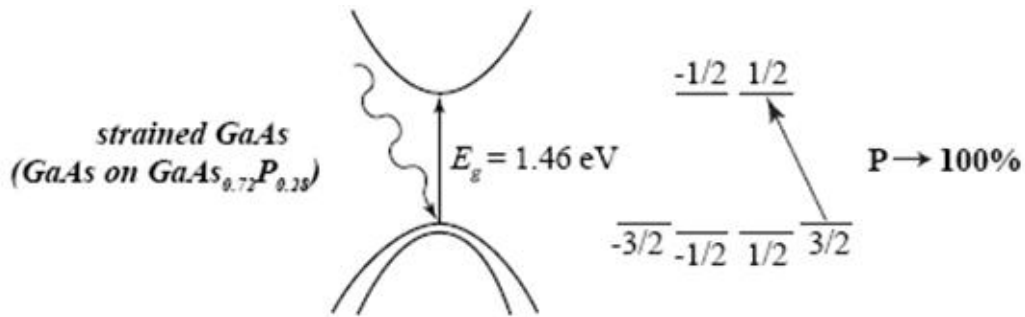


**Figure 2.6 The energy level diagram of strained GaAs with electromagnetic transitions.**

Figure 2.6 shows the electromagnetic transitions of strained GaAs. The energy split of HH and LH is 65 meV, typically. Strained-layer superlattices GaAs also generate high polarized electron beam. The polarization achieved 86% [41].

## 2.2. UHV preparation chamber

The process of GaAs photocathode preparation is including welding the sample to Nb plug, high temperature surface treatment; evaporate cesium and oxygen and cathode transferring. The Cs-O monolayer is very sensitive to the residual gases such as oxygen and water. The vacuum chamber design is one of the significant steps.

The requirements of UHV chamber design is

- 1) The background vacuum of preparation chamber and transferring line is under  $10^{-11}$  torr.
- 2) The water vapor and oxygen partial pressure is lower than  $10^{-12}$  torr.
- 3) The GaAs sample can be heat to 610 °C and the temperature fluctuation less than 30 °C.
- 4) The gauge can measure the vacuum range around  $10^{-11}$  torr
- 5) The GaAs photocathode keep under 10-11 torr vacuum in storage and transferring.

### 2.2.1 UHV photocathode preparation chamber

The preparation chamber is a 10 inch diameter spherical vacuum vessel with 8 inch vacuum port and 8 inch viewport and ten small feedthru ports. The hydrogen is higher than 90% when the chamber base pressure in the  $10^{-11}$  torr scale. To achieve  $10^{-12}$  torr UHV, the hydrogen level have to be suppression. The entire UHV chamber baked to 400 °C to degas the hydrogen. The pumps consist of a 270 L/s ion pump with TSP

which has effective pumping speed of 1000 L/s. The spherical chamber has one RGA feed through for detect the residual gases partial pressure, one window for laser, one cold cathode gauge with americium which can test the UH vacuum and can be restarted at low  $10^{-11}$  torr, one leak valve to regulate the oxygen pressure. A 1 inch diameter anode with 0.3 inch internal diameter anode was designed to collect the emission electrons. The Cs source above the anode evaporates the Cs through the hole to the GaAs.

The stalk heater connects a copper sleeve to heat the Nb plug with GaAs sample to 580 °C to 610 °C. The temperature of stalk heater can reach to 720 °C. With ANSYS simulation, the GaAs sample can be heat to 630 °C.

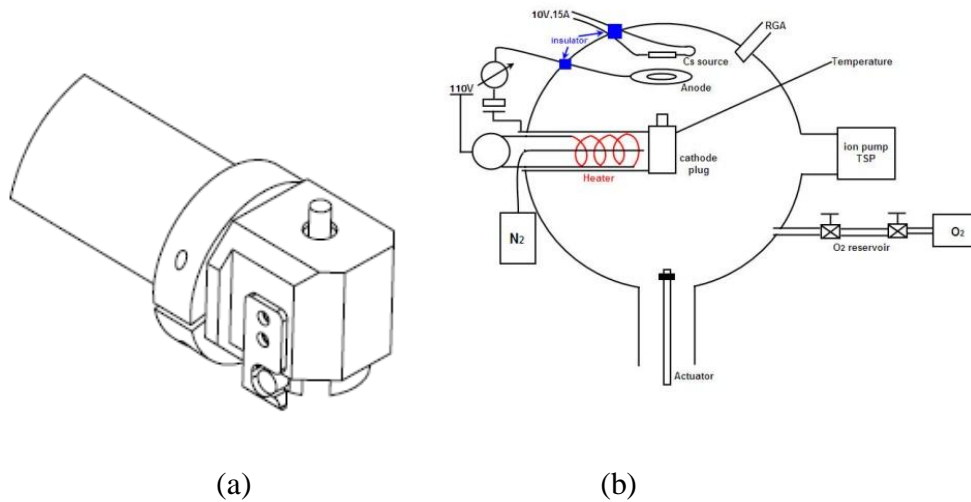


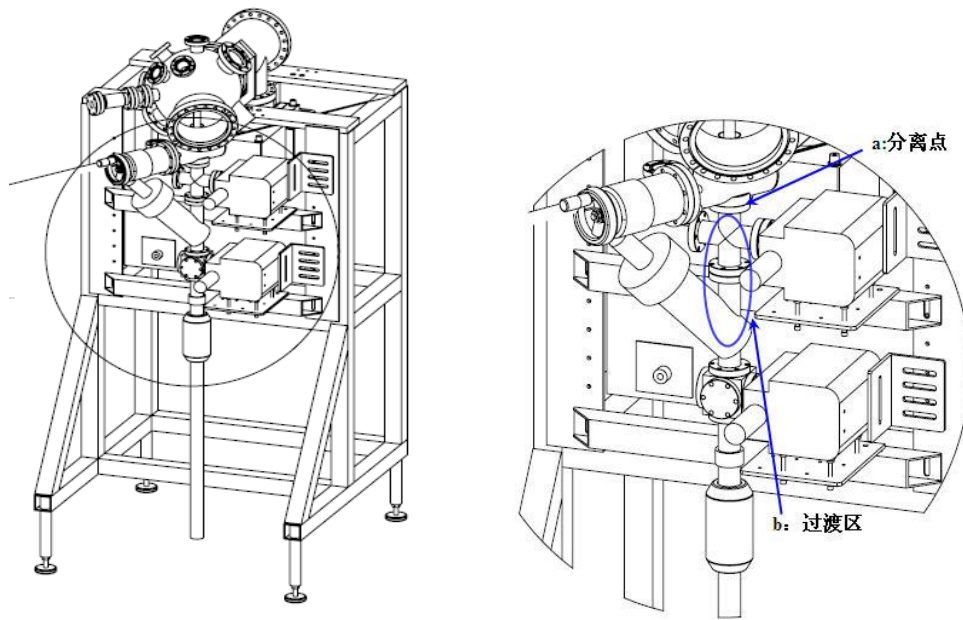
**Figure 2.7 (a) Stalk heat with Nb plug;(b) The sketch of the GaAs preparation chamber**

### 2.2.2 Loadlock system

Transport assemblies is planned for initial cathode pump down and then for cathode insertion through a load lock arrangement into either the preparation chamber or the SRF cavity. The transporter uses a magnetically coupled actuator to extend the cathode through the load lock valves. A ¼-turn bayonet style attachment mechanism is integrated into the end of the actuator. This arrangement enables detachment and retraction of the actuator from the cathode after placement into either the process chamber or SRF cavity. Once the actuator is retracted, the transporter can then be removed from the SRF cavity string in preparation for cavity testing.

The transport assembly includes a 6 way cross for mounting a vacuum ion pump, NEG pump along with a viewports and vacuum gauging. The base vacuum achieved to  $2 \times 10^{-11}$  torr. The arrangement of the transport with preparation chamber assembly is shown in figure 2.8(a). The transporter separates from the preparation chamber from point “a” of figure 2.8 (a) with two metal valves closed.

A clamp system is used to secure the cathode into the SRF cavity socket during operation. The clap system arrangement is capable of securing the cathode into the gun cavity while maintaining beam line cleanliness required for SRF operation. Figure 2.8(b) shows the sketch of clamp system. Mounting provisions are incorporated in the clamp to attach a load lock arrangement for cathode insertion using the cathode transport assembly. The thermal contact resistance between the cathode and the cavity was simulated by ANSYS assuming 10 psi pressure across the RF seal. The thermal conduction is satisfied by this design.



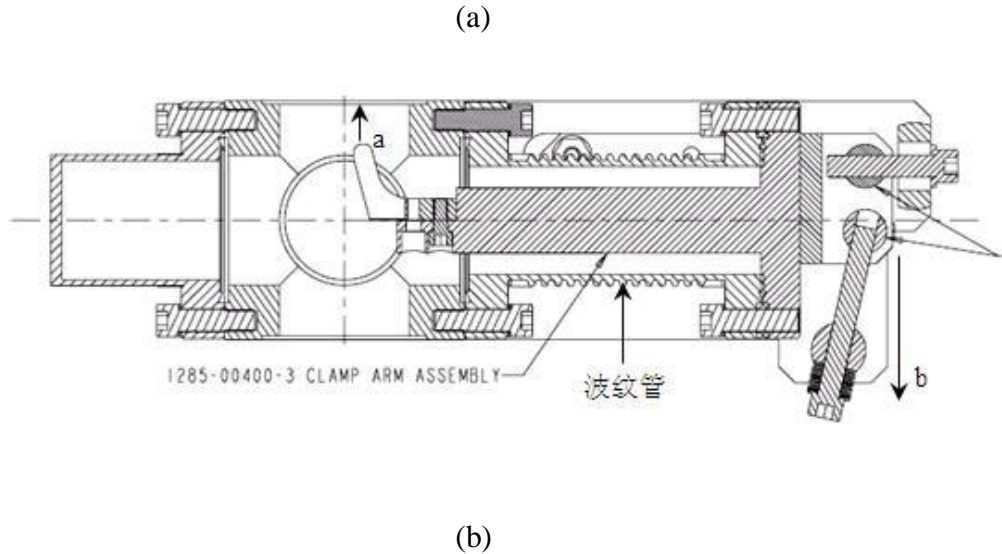


**Figure 2.8 (a) Transporter and preparation chamber assembly ,(b) Cathode clamp system**

### 2.2.3 UHV achievement

The procedure of pumping is listed as follows.

- 1) The turbo pumps the preparation chamber's vacuum to  $10^{-6}$  torr.
- 2) Bake the entire chamber to  $190\text{ }^{\circ}\text{C} \pm 10\text{ }^{\circ}\text{C}$ . 20 thermal couples measure the location temperature.
- 3) After bake 100 hours, heat the stalk heat and Cs source to  $300\text{ }^{\circ}\text{C}$  for 2 hours. Meantime, degas the RGA detector and ion pump. Activate the NEG pump.
- 4) Move the magnetically coupled actuator while separate baking the transporter for 24 hours.
- 5) Cool down the system to  $60\text{ }^{\circ}\text{C}$  and evaporate the Titanium while the Cs source and GaAs sample keep in  $200\text{ }^{\circ}\text{C}$ .
- 6) Turn on the ion pump and turn off the heater for Cs source and GaAs sample.
- 7) The vacuum of preparation chamber achieve to  $7 \cdot 10^{-11}$  torr when the chamber reach to room temperature.
- 8) After 24 hours, the vacuum reach to  $10^{-12}$  torr scale and the cold cathode gauge shut off automatically.

Table 2.2 shows the residual gases partial pressure in main chamber measured by RGA.

**Table 0.2 The residual gases partial pressure in preparation chamber**

Mass	Pressure (torr)	Gas
2	8.10E-11(88.7%)	H <sub>2</sub>
18	5.01E-12(4.4%)	H <sub>2</sub> O
28	2.60E-12(2.04%)	Air/N <sub>2</sub> /CO
17	1.91E-12(1.54%)	H <sub>2</sub> O
44	1.54E-12(1.12%)	CO <sub>2</sub>
36	1.11E-12(0.925%)	HCl
16	1.02E-12(0.719%)	O <sub>2</sub>
20	8.11E-13(0.434%)	Ar
27	7.60E-12(0.402%)	HC <sub>x</sub>

The 4% water vapor is the main factor of degrade quantum efficiency of GaAs photocathode. The signal of CO<sub>2</sub> or CO may come from the RGA probe. We turn off the RGA to suppress CO<sub>2</sub>/ CO before activate the GaAs.

### 2.3. GaAs photocathode activation

#### 2.3.1 Procedures for activating GaAs cathodes

The NEA surface of GaAs is normally formed by cesium and oxygen in ultra high vacuum. The p-type, Zn doped GaAs crystal was used as cathode sample. Our GaAs sample is provided by AXT.Corp. To minimize the emittance, the emission surface is chemical polished. The 100um GaAs piece was chosen to decrease the RF loss on the photocathode. Table 2.3 shows the GaAs sample parameters.

**Table 0.3 GaAs sample specification**

	Guaranteed
Doping	GaAs-Zn
Diameter	50±0.5mm
Orientation	100±0.5
Carrier Conc	3E18~6E18atom/c.c
Resistivity	1.1E-2~1.7E-2 Ohm.cm

<b>Mobility</b>	93~119 $\text{Cm}^2/\text{v.s}$
<b>Thickness</b>	75~125 $\mu\text{m}$
<b>Surface Finish</b>	Side 1:Polished Side2:Etched

The GaAs crystal is 5cm diameter. It was cut into 2.2mm\*2.2mm small pieces along 001/010 surface in glove boxes. Keep the emission surface away from any metal tools. The small GaAs sample was soldered onto a high RRR Nb plug shows in Figure 2.9.



**Figure 2.9 Four high RRR Nb plugs**

Indium and lead are good choice for soldering the GaAs to other metal. Indium is usually used for soldering the GaAs in DC gun. The melting point of indium is 157 °C and superconducting critical temperature is 3.14K. The melting point of lead is 327 °C and superconducting critical temperature is 7.2K. The Q fact of SRF gun can be improved if the lead can be used as the soldering material. We clean the Nb plug surface with HCl and acetone and then move the Nb plug into glove box which filled with  $\text{N}_2$ . The welding temperature keeps at melting point plus 30 °C for 5 minutes and then cools down in general. Both Indium and lead can solder the GaAs on the Nb. To test the solder robustness, we cool down the soldered GaAs with Nb plug into  $\text{LN}_2$  in 1 second and heat it with a heater gun. After repeat 3 times, the GaAs strip down from the Nb with lead soldering. The indium soldering piece is still robust.

There are two kinds of cesium source provide cesium atom in evaporate. One source provide by Alvatec is the desired alloy containing the cesium in a small stainless steel tube which is gas-tight sealed by a pressed indium sealing. Another choice is cesium chromate source provided by SAES getter. The  $\text{Cs}_2\text{CrO}_4$  with ZrAl sealed in a stainless

steel tube. Comparison with two kinds of sources shows the first one release ultra pure cesium vapor. However, the Alvatec source evaporates indium to the GaAs surface in the source activation. The Alvatec source has to keep in vacuum after the indium sealed open. For our chamber design, Alvatec source is unsuitable for GaAs activation. The SAES getter source (figure 2.10) is used for activation successfully. The source current and temperature dependent is shown on figure 2.10(b). The cesium starts to evaporate when the temperature reach to 550 °C which response to 4A of current. The source have to degas in 400 °C prior activation.

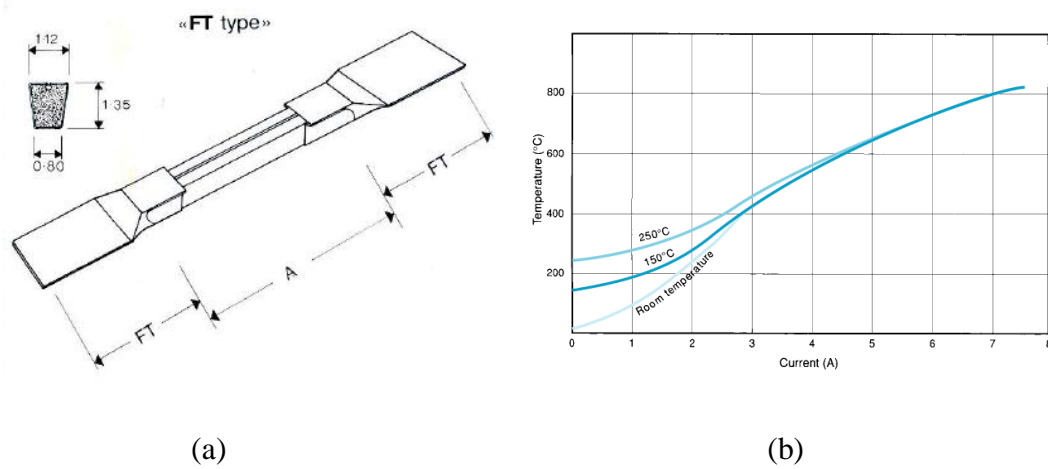


**Figure 2.10 a) SAES getter Cs source; b) The current and temperature dependent of source**

To achieve high quantum efficiencies, the NEA surface must be prepared on an atomically clean surface. There are two ways to achieve a surface free of oxides and carbon related contaminants. One is heat the GaAs to 580 °C to 600 °C for about 45 minutes. Another way is atomic hydrogen cleaning which is a technique for removing oxides at relatively low temperature of 450 °C. For polarized source, high temperature treatment results in the reappearance of the surface charge limit so high temperature treatment is avoided. Our first step is generating non-polarized beam with bulk GaAs. The high temperature clean technique is much more convenient than atomic hydrogen cleaning. The most critical step is maintaining the temperature at certain value. The crystal lattice can be damaged when the temperature higher than 620 °C. We carefully calibrate the temperature between GaAs and thermal couple on the stalk heater. Figure

2.11 shows the the GaAs crystal temperature dependent on thermal couple reading. The GaAs temperature is estimated by this figure in activation.

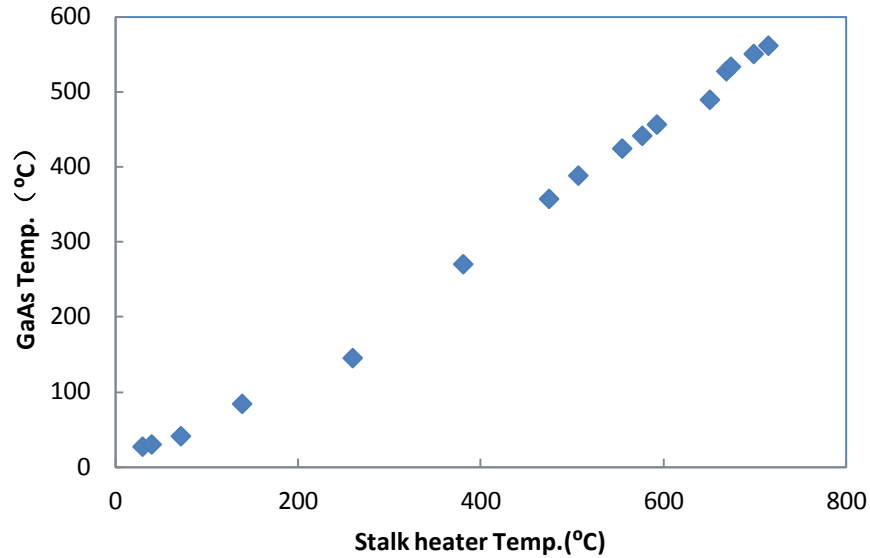


**Figure 2.11 The calibration of GaAs temperature in high temperature surface cleaning.**

The smallest energy gap of GaAs is 1.42eV which response to 871nm of the light wavelength. We use 543nm HeNe laser as driven laser source. The bias on cathode is -50V, so the laser filter is used to avoid the space charge limite effect. The laser is focused on the 2.2mm\*2.2mm GaAs sample. The laser FWHM size is 140um (Figure 2.12). The laser size and power is important to GaAs life time.

The photocurrent is measured by a Keithle pico-current meter and read by Labview through a GPIB card.

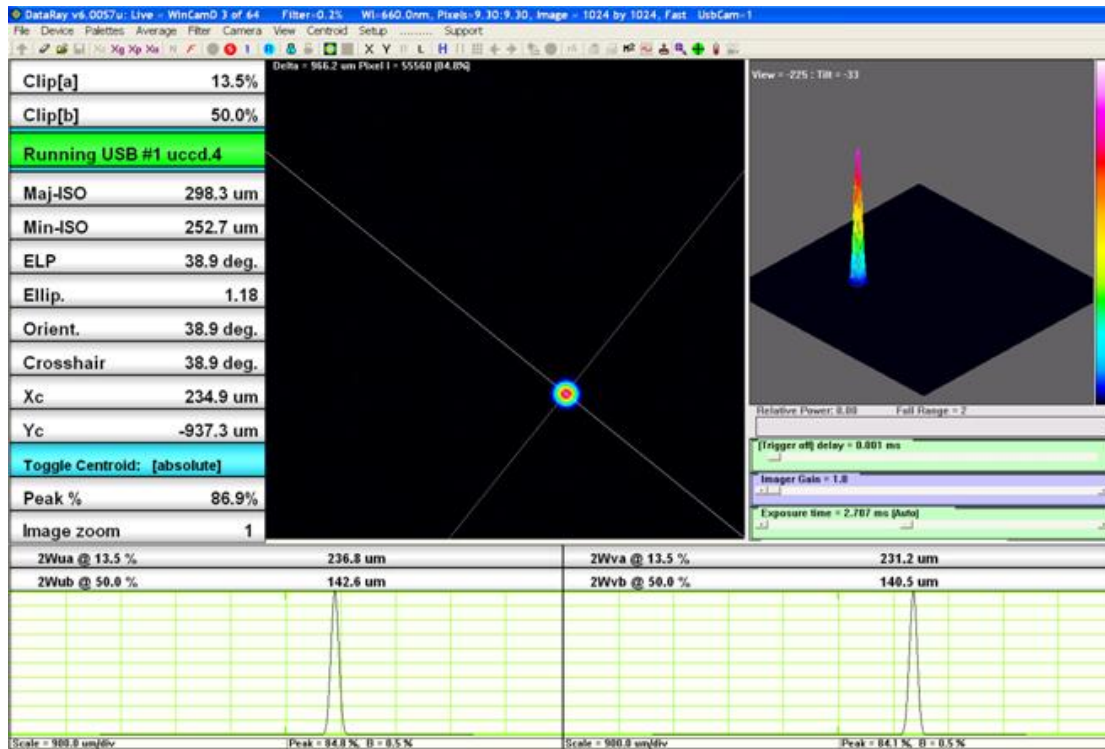


**Figure 2.12 Laser spot illuminate on the GaAs**

The activation process is extremely important for assuring the stability and long lifetime of the polarized electron beam. We employed three different activation methods: The yo-yo process with an excess of oxygen; the yo-yo process with an excess of caesium; and full saturation with both. In the typical yo-yo process, the sources of oxygen and caesium are opened and closed periodically. In the saturation process, caesium and oxygen are introduced continuously into the chamber to attain a maximum current. The most suitable time to begin to activate the GaAs is after the temperature of the wafer falls below 30°C. The SAES getter's Cs dispenser is degassed while heat-cleaning of the GaAs is underway.

The background vacuum of the preparation chamber is better than  $1 \cdot 10^{-11}$  Torr. During the yo-yo process, when the source of oxygen is open, that of caesium should be closed, and vice versa. Figure 2.13(a) shows typical experimental results from the yo-yo process. In the yo-yo process with excess oxygen, the photocurrent fell when the oxygen flowed into the chamber and correspondingly, the photocurrent increased whilst the Cs evaporated. The final peak photocurrent was reached in one hour and 20 minutes with

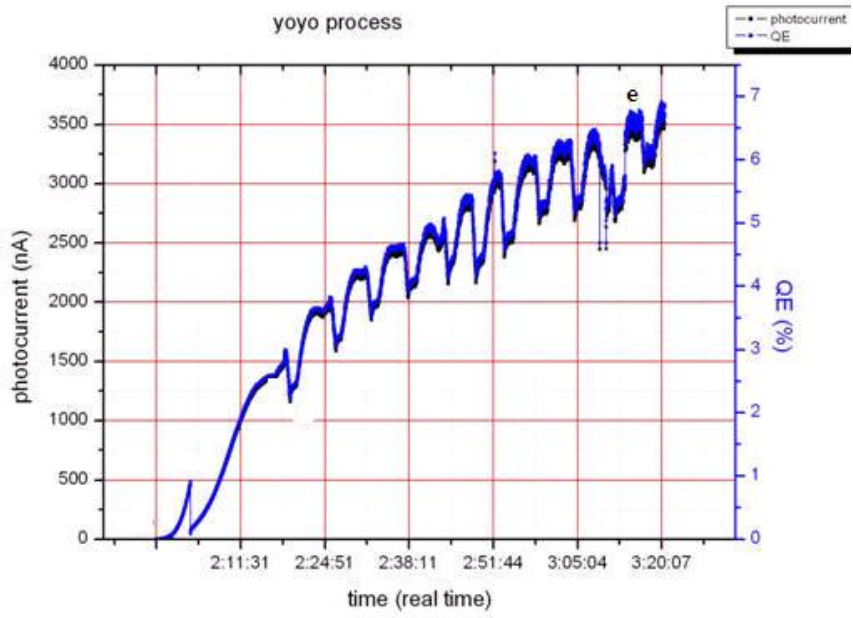
excess oxygen. In the yo-yo process with excess Cs, the photocurrent decreases while the Cs was evaporating, and then increases when oxygen was let into the chamber (Figure 2.13(b)). The oxygen partial pressure was  $2 \cdot 10^{-9}$  Torr. The photocurrent is very sensitive to the amount of oxygen, so the rise in the photocurrent was much quicker than when oxygen was in excess. The final peak photocurrent was reached in one hour with excess Cs. We routinely obtained a quantum efficiency above 8% at 544nm from a 100um bulk CVD GaAs sample. For the saturation process (Figure 2.13(c)), the oxygen's partial pressure and Cs's evaporation rate must match very well. In our system, the preparation chamber oxygen pressure is  $(2.2 \pm 0.2) \cdot 10^{-10}$  Torr while the Cs source current is 6 A. The photocurrent increases constantly at first and then becomes a little unstable. Though vernier regulation, we matched the oxygen leak-valve to the rate of evaporation of Cs; then, the photocurrent attained its maximum. The total process took 35 minutes and the quantum efficiency was 9% at 544nm.

Comparing the two yo-yo processes and saturation condition, the following differences are apparent:

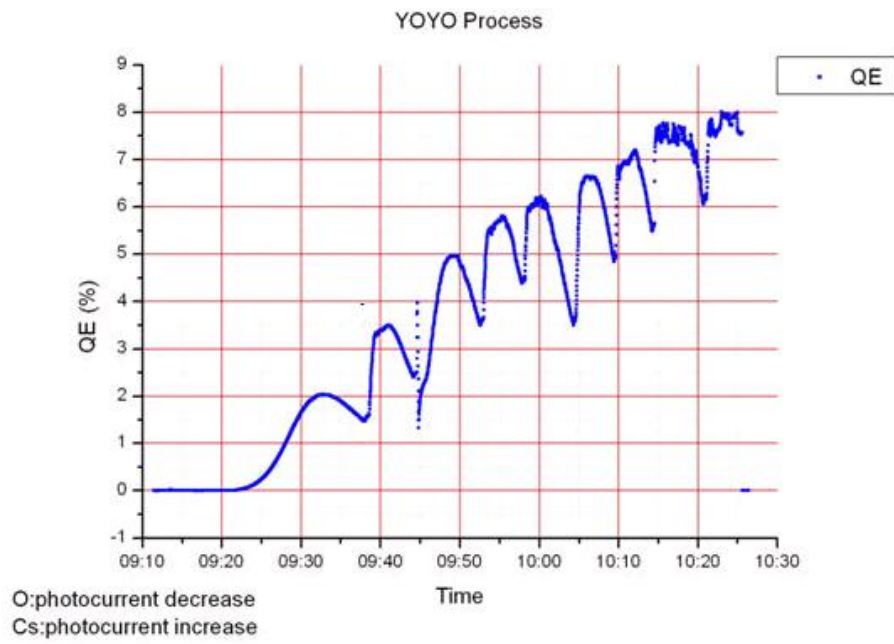
At each peak in the yo-yo process, there is not a sufficient NEA effect on the GaAs surface due to the lack of caesium/oxygen in the chamber after opening oxygen/caesium, so the photo current experiences a slight temporary decrease. This does not occur in the saturation process, where the amounts of oxygen and caesium are matched well.

The saturation process has the advantage of lessening activation time. Thus, the cost of the process in time is less than half that of the yo-yo process.

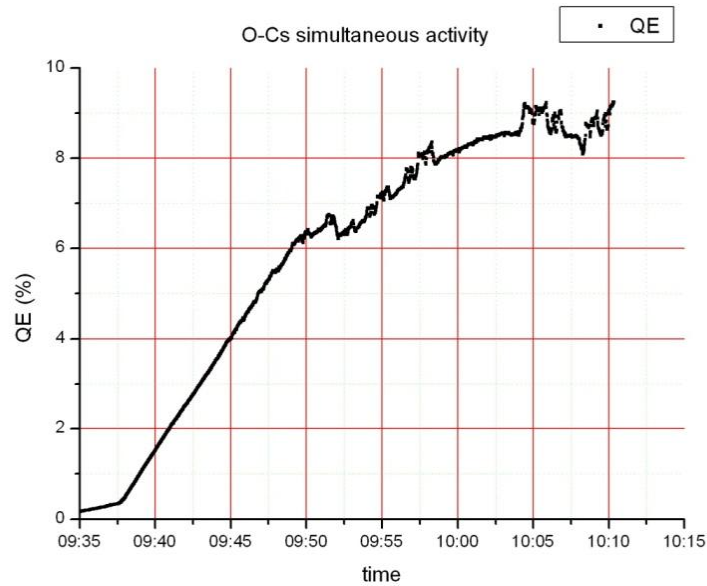
The saturation process is difficult to control. The speed of the Cs evaporation and the oxygen flow rate must be carefully monitored and regulated throughout the procedure.



(a)



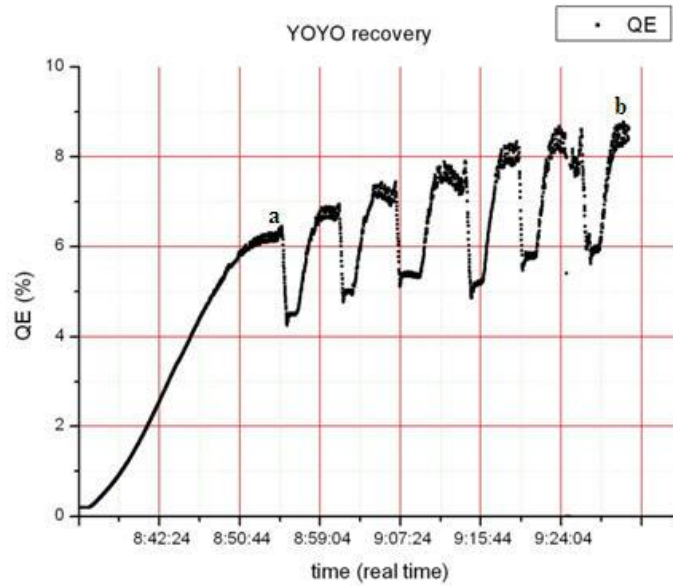
(b)



(c)

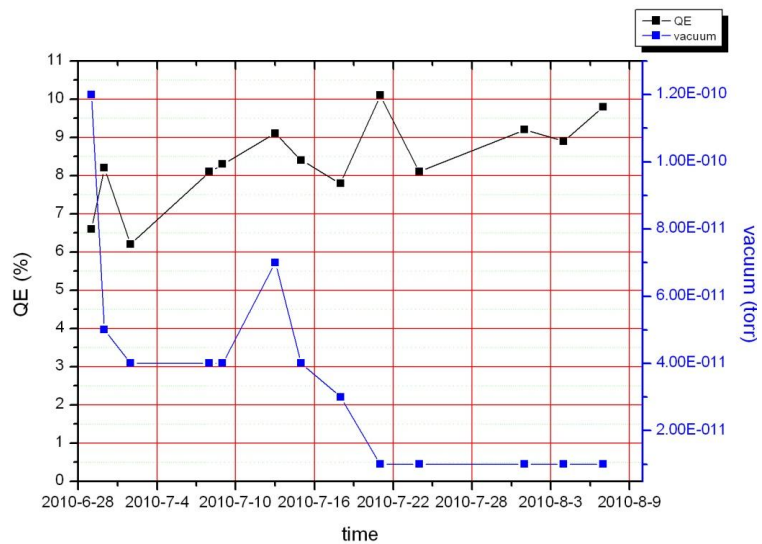
Figure 2.13 GaAs photocathode activation (a) is the yo-yo process with excess oxygen; (b) is the yoyo process with excess Cs; and, (c) is the saturation process

After the GaAs used a while, the quantum efficiency decrease can be recovery by yoyo process. Figure 2.14 shows the yoyo recovery photocurrent curve. The quantum efficiency achieve to 6.2% after cesium evaporate. It seems most cesium leave the GaAs surface but most oxygen still stay on the surface. With yoyo process, the final peak achieve to 8.5% in one hour.



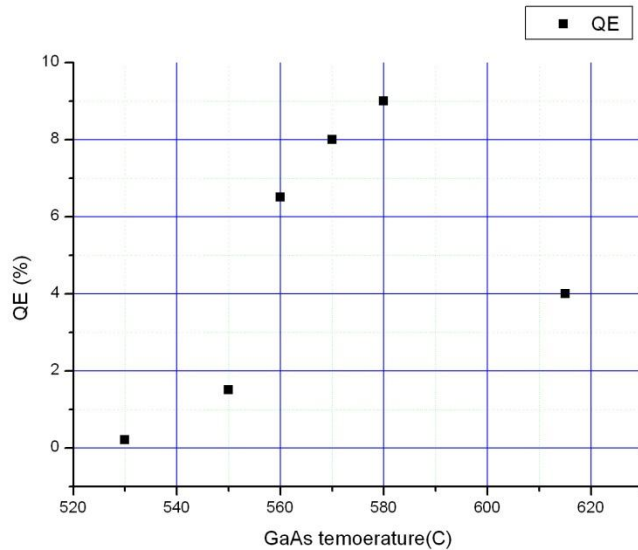
**Figure 2.14 GaAs re-activation by yoyo process**

Figure 2.15 shows the results of the quantum efficiency of 13 times GaAs activation dependent on vacuum. The quantum efficiency achieve to higher than 8% when the base vacuum reach into  $10^{-12}$  torr scale.



**Figure 2.15 The quantum efficiency of cathodes (bark point) and vacuum values (blue point).**

The oxides can be desorbed from the GaAs surface under heat cleaning. We activate the GaAs after heating the sample to each of different temperature for 45 minutes. All samples activated by the yoyo process and the results shows in Figure 2.16



**Figure 2.16 The quantum efficiency dependent on heat cleaning temperature**

The highest quantum efficiency of 9% was obtained as a result of heating sample at 580 °C. After heating to 618 °C, the quantum efficiency drop to 4%. Such sample can be recovered to higher quantum efficiency. The quantum efficiency reduce is the result of excessive heating temperature which damages the GaAs lattice.

### 2.3.2 Photocathode life time measurement

One of the important parameter of the photocathode in the SRF polarized gun project is the dark lifetime. The time delay between cathode preparation in the preparation chamber and its use in the SRF gun is expected to be ~ 36 hours determined by the bake and cool off time of the load-lock section. The quantum efficiency of the photocathode is degraded by the internal instability of the activation layer and by the residual gas in the vacuum system. Figure 2.17 shows the quantum efficiency decay in the dark room. The quantum efficiency is 0.5% after 100 hours. The 1/e decay time is 28 hours. The quantum efficiency decay is due to the residue gas poison and cesium left the surface.

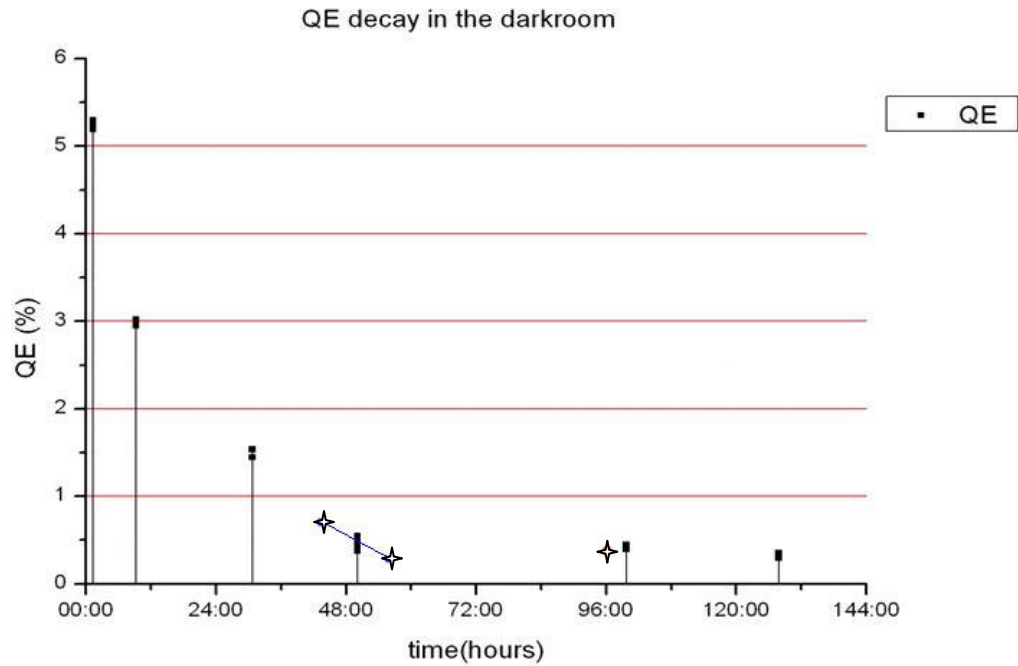


**Figure 2.17 The quantum efficiency decay in the darkroom. Dark points are obtained from cathode in main chamber and star point was obtained from cathode in transferring line.**

Quantum efficiency decay in cathode transferring is due to the vacuum deterioration while the magnetic couple move. When the GaAs photocathode is transferred from the preparation chamber to the storage cube, the vacuum of the transferring line is a low  $10^{-9}$  Torr. Experiments show that the lifetime of the GaAs photocathode is less than 10 minutes in this vacuum. Slowly moving of magnetic-coupled transfer rod preserves the vacuum at this level. In our load-lock system, the middle section is opened to the atmosphere when connecting the storage cube to the gun. We found the heat developed while baking the middle section and during pumping through the gate valve destroys the Cs-O layer of the GaAs photocathode. So the middle-section baking process is avoided. The GaAs must pass through the middle section in seconds, so that the time they spend in the bad vacuum is as little as possible. In a dry run, the quantum efficiency of GaAs remained at 0.7% when it was stored in the cube for 50 hours after moved through the vacuum in the middle section. This test proved that the quantum efficiency of the GaAs is

more than 0.7% after the SRF gun cooled down, a value that is sufficient for the lifetime test of the GaAs in the gun.

Figure 2.18 shows the photocurrent decay of photocathode in operation. Three samples activated by different ways were compared. The sample activated by saturation process shows longer lifetime than the sample with yoyo process.

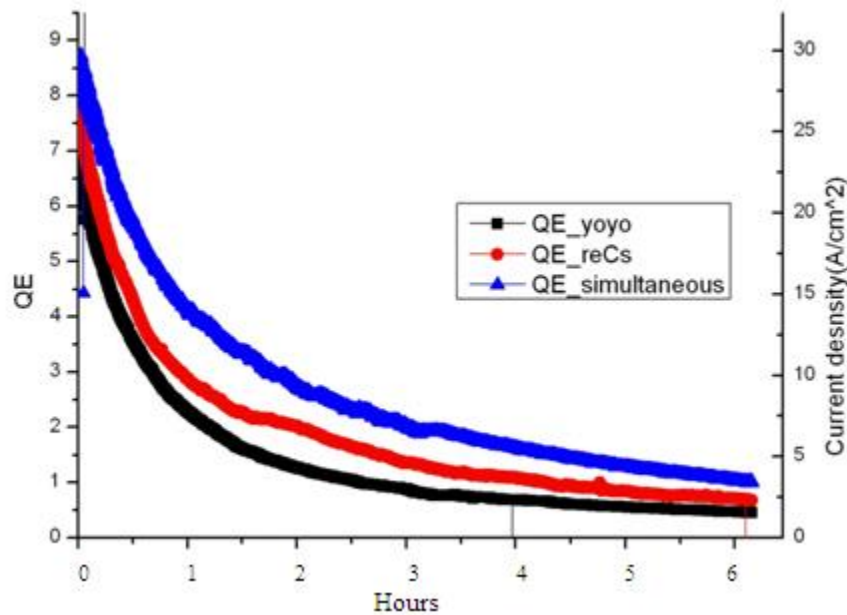


**Figure 2.18 The lifetime three samples activated by saturation process, yoyo process and re-caessation process.**

### 2.3.3 Ion back bombardment in vacuum chamber

The cathode operation life time is much shorter than the dark room life time. It is difficult to explain by residual gas poison or laser heating. In the DC gun, the ion back bombardment is the main cause of degradation of quantum efficiency of GaAs photocathode[42]. On the electrons path, electrons ionize residual gas and produce low energy ions. In our preparation chamber, 88% of residual gas is hydrogen. The electron hydrogen cross section is zero when the electron energy less than 10eV[43]. The ion back bombardment would not be happen if the bias of cathode is 10 volts. The quantum efficiency has nothing to do with ion back bombardment.

We obtained same decay time from three times re-activated GaAs samples with the bias of -50 volts. Then, we reduce the bias voltage to -10 volts and reduce the laser power to  $0.95 \mu\text{W}$  to avoid space charge limitation. After 24 hours, the quantum efficiency decrease from 5.7% to 2%. With the same laser power and increase the bias voltage to -50 volts, the photocurrent decrease from 6.3% to 1.5% in 24 hours. Figure 2.19 shows the comparison of photocurrent decay of GaAs photocathode with different bias in 24 hours.

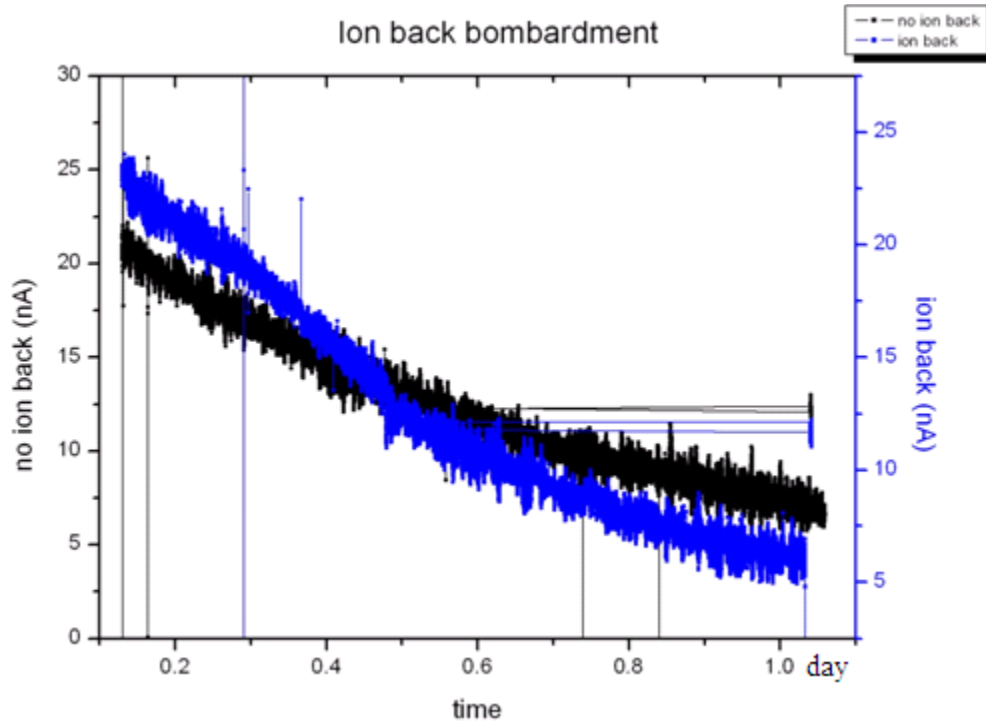


**Figure 2.19** The comparison of photocurrent decay of GaAs photocathode with different bias in 24 hours. The dark curve was measured when the cathode biased to -10 volts and blue curve was measured in -50 volts.

The photocurrent decay measured in cathode biased to -10 volts is comparable to the photocurrent decay in the dark room. The ion back bombardment is a main factor of reducing the quantum efficiency when the laser power is very low in the preparation chamber. The rates of ion bombardment in the RF gun and in the DC gun are similar[44].

## Chapter 3. The physics of GaAs photocathode SRF electron gun

### 3.1. SRF electron gun

#### 3.1.1. SRF gun properties

The normal conducting RF guns were demonstrated to produce high quality beam with low duty cycle. By combining with the normal conducting RF gun and superconducting material, the dissipated RF power of the gun can be reduced and CW operation for high average current and low emittance can be realized [45].

The characteristics of SRF gun is listed as follows:

i. High peak field on the cathode

With the RF technology, the peak field of SRF gun is much higher than DC gun. The maximum peak field on the photocathode is limited by the quench field of superconductor cavity. The peak fields of BNL 1.3 GHz plug gun reached 56 MV/m without photocathode in 2 K. The  $Q$  factor decrease when insert the normal conductor photocathode into the gun due to heat. The heat generation from the photocathode also decreases the field limitation of quench. With RF choke filter structure, the thermal flow between photocathode and cavity can be insulated while prevents the RF power from leaking out of the cavity. With such design, the peak field of FZD 3.5-cell SRF gun achieved 18 MV/m in a stable CW operation [46].

ii. High repetition frequency or CW operation

The SRF cavities are made from high RRR bulk niobium. The dissipated RF power is reduced by several orders of magnitude compare with normal conducting RF gun. Therefore one advantages of SRF gun is CW or high repetition frequency operation for generation high average current beam.

iii. Ultra high vacuum around cathode

With cryogenic pumping of cavity wall, the vacuum in SRF gun has ability to reach  $10^{-12}$  torr vacuum. The good vacuum decrease the ion back bombardment rate and prolong the life time of photocathode.

iv. Secondary electron back bombardment

The multipacting may happen on the photocathode due to secondary electron back bombardment in RF gun. The photocathode with monolayer activation is very sensitive to the secondary electron back bombardment

v. Emittance compensation

In contrast to normal conducting RF guns, the emittance compensation by solenoid placed around cavity is impossible due to superconductivity breakdown by magnet field. A solenoid placed at the SRF gun exit and RF focusing by recess cathode was used to minimize the emittance [47].

### 3.1.2. BNL 1.3 GHz SRF plug gun characteristic parameters

The BNL's plug gun is a 0.6 cell 1.3 GHz SRF gun. It got its name from a removable niobium plug, located in the back of the gun, which holds the GaAs cathode. Earlier, the suitability was tested of BNL's 1.3 GHz half-cell SRF gun for the Nb photocathode [48]. The gun consists of a niobium cavity, single beam pipe port and two couplers for RF input and signal pickup. The unmodified cavity is shown in Figure 3.1. The modification of this SRF gun was developed to incorporate a socket to its back face for normal conducting cathode insertion.



**Figure 3.1 Unmodified BNL 1.3 GHz gun cavity.**

Modified SRF gun will be a test bed for various cathode. It will be tested for GaAs photocathode at first. The socket design features enable insertion and positioning a plug style cathode base with a RF face seal. The piece of activated GaAs photocathode placed on the high RRR niobium plug. A conflate flange is incorporated for vacuum sealing. This

gun is suitable for the low current due to without choke structure. Figure 3.2 shows the dimensions of the modified gun.

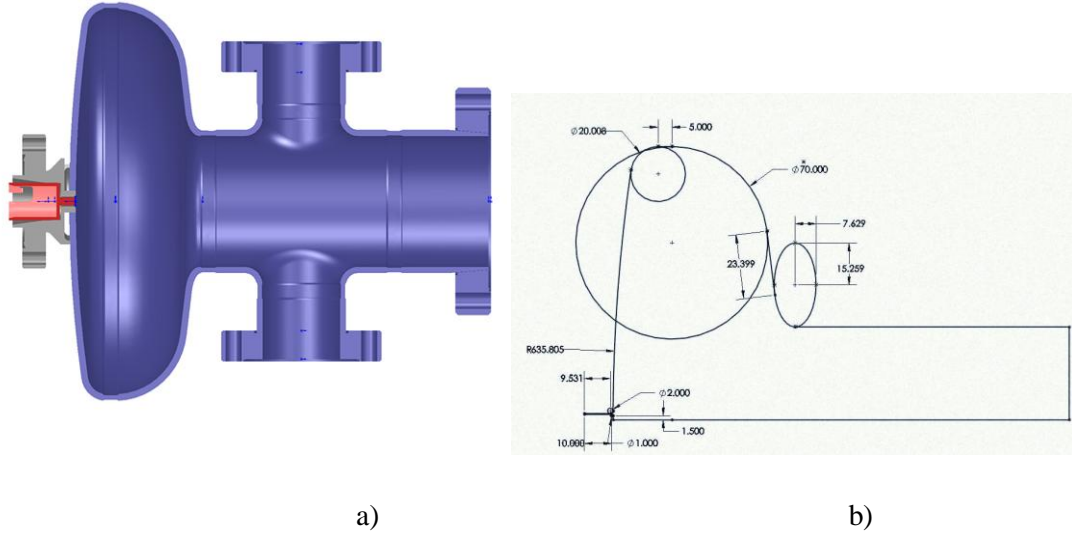


**Figure 3.2 BNL 1.3 GHz SRF plug Gun: a) the cross section of modified gun; b) the dimensions of the cavity structure.**

The modified gun was simulated by Superfish and Figure 3.3 shows the electromagnetic field inside the gun.

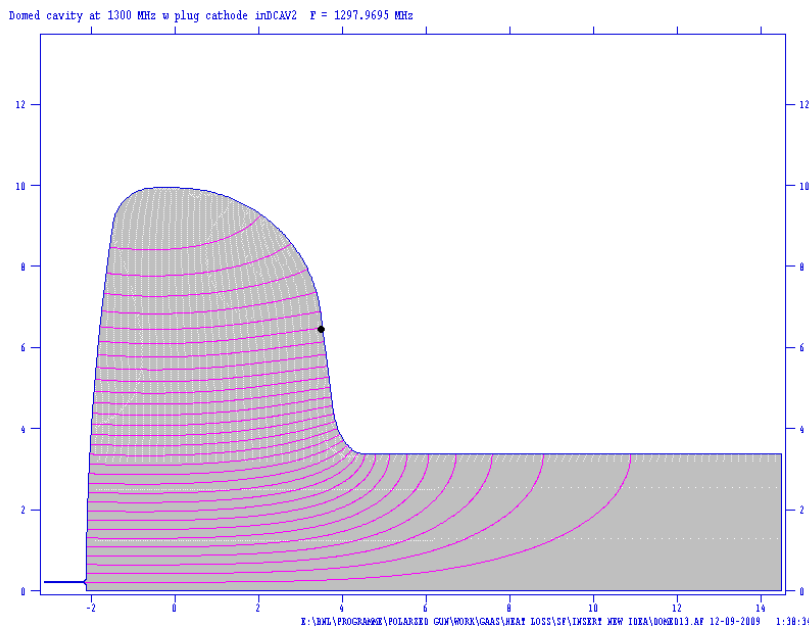


**Figure 3.3 The electromagnetic field in the gun simulated by Superfish.**

The RF parameters of the gun are listed in Table 3.1.

**Table 3.1 The parameters of the gun**

Frequency	1297.97 MHz
Temperature	2 K
$Q_0$	$7 \times 10^9$
$B_{peak}/E_{peak}$	1.787
$E_{peak}/E_0$	2.6
Peak field	15 MV/m
Storage Energy	0.48 Joules
$\kappa$	21.34 [MV J <sup>-1/2</sup> ]

In the Table 3.1, the parameter  $\kappa$ , independent of the surface resistance and cavity size, is defined as

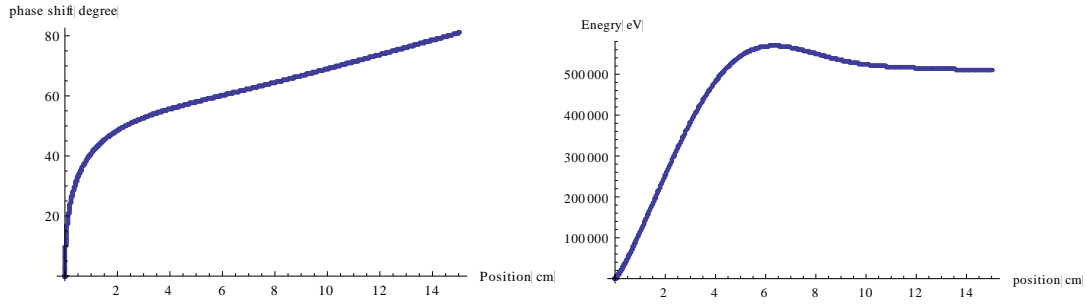
$$E_{peak} [MV] = \kappa \sqrt{U_0 [J]} \quad (0.1)$$

Larger  $\kappa$  gives higher peak field on the cathode for the same storage energy. The beam quality is related to the peak field.

The gun operation parameters are listed in Table 3.2.

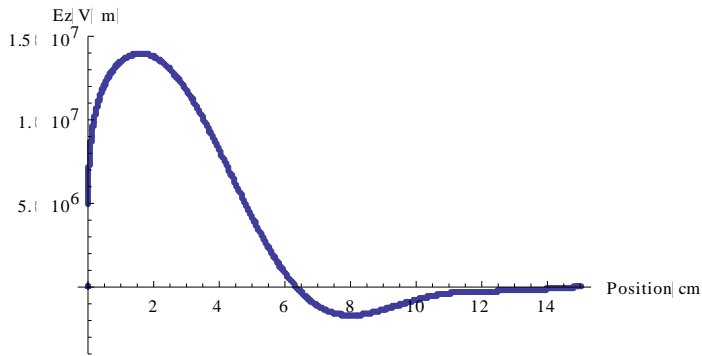
**Table 3.2 Gun operation parameters**

Repetition frequency	81.25 MHz
Laser wavelength	532 nm
Pulse length	10 psec FEHM
Fluctuation	2.4% pk-pk measured
Spot size	2 mm (diameter)
Laser Power	2 mW
Bunch length	10 ps
Bunch charge	0.12 pC
Average current	10 uA
Initial RF phase	20 °
QE	0.1%-0.6%



(a)

(b)



(c)

**Figure 3.4 Single particle simulation when the initial phase is 20 degree in the gun: a) The phase shift between particle and RF field; b) The Energy of particle in the gun; c) The electric field meet by the particle in the gun.**

The phase of electrons shifts with the RF field due to low energy of particles in the half cell. The beam quality and energy is dependent on the initial phase. The Figure 3.4 shows the single particle tracking by program Parmela with the parameter listed in Table 3.2. The length of half cell cavity is 6 cm and the beam pipe is connected on the gun. Figure 3.4c shows the electrons meet decelerate phase in the beam pipe.

In the gun test setup, the plug gun is coupled to a beam transport, which includes a non evaporable getter, followed by a solenoid focusing magnet and then a dipole magnet, which directs the beam into a faraday cup, which measures the current. The energy spread of the beam will expand the beam size after the electron beam passes through the dipole magnet. The energy spread is minimized by choosing the initial phase to eliminate possibility of the beam hitting the pipe. Figure 3.5 shows the beam energy spread at gun exit relative to the initial phase.

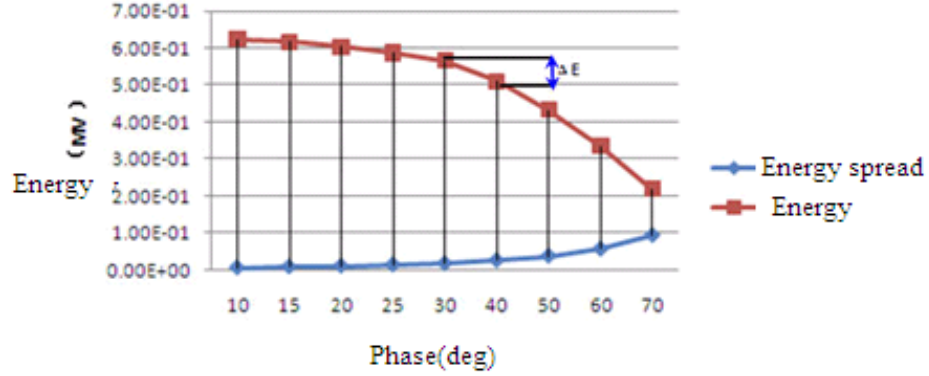


**Figure 3.5** The beam energy spread at gun exit relative to the initial phase.

The energy spread is minimum when the initial phase is  $0^\circ$  which corresponds to the electric field of 0 MV/m. To extract all the photocurrent from the cathode, the electric field have to be high enough to overcome the space charge effect. Based on Parmela simulation, we chose  $20^\circ$  as the initial phase that achieves 5 MV/m at the cathode emission surface.

### 3.1.3. SRF cavity properties

Following the book [49], I describe the SRF cavity properties in this section. The RF cavity is a resonant waveguide with closed boundaries. The storage energy is coupled to the particle when the particle goes through the cavity.

The voltage gained by the particle passing through the cavity is given by

$$V_{acc} = \left| \frac{W}{q} \right| = E_{acc} \times l = \left| \int_{z=0}^{z=l} E_z e^{i\omega_0 z/c} dz \right| \quad (0.2)$$

Where  $W$  is the energy gain of the particle and  $q$  is the particle charge. The average of the field along the axis is given by

$$E_0 = \frac{1}{l} \int_{z=0}^{z=l} E_z dl \quad (0.3)$$

The particle takes a finite time to traverse the cavity, leading to energy gain reduction which can be described by the transit time factor

$$T = \frac{E_{acc}}{E_0} \quad (0.4)$$

To characterize the losses in a cavity, the shunt impedance is defined by

$$R_{sh} = \frac{V_{acc}^2}{P_{loss}} \quad (0.5)$$

For one accelerating mode, the shunt impedance gets large when the dissipated power is minimized.

The total storage energy in the cavity is given by

$$U = \frac{1}{2} \epsilon_0 \int_V |\vec{E}|^2 dv = \frac{1}{2} \mu_0 \int_V |\vec{H}|^2 dv \quad (0.6)$$

The time averaged energy in the electric field is equal to that in the magnetic field. One more parameter of a resonant cavity is the quality factor, which is defined as

$$Q_0 = \frac{\omega_0 U}{P_{loss}} \quad (0.7)$$

Combining 3.5 – 3.7, a parameter independent of the surface resistance and cavity size can be defined as

$$\frac{R_{sh}}{Q_0} = \frac{V_{acc}^2}{\omega_0 U} = \frac{(\int \vec{E} dl)^2}{\frac{1}{2} \omega_0 \epsilon_0 \int_V |\vec{E}|^2 dV} \quad (0.8)$$

Eqn. 3.8 also can be expressed as

$$V_{acc}^2 = \frac{R_{sh}}{Q_0} \cdot Q_0 \cdot P_{loss} \quad (0.9)$$

Eqn. 3.9 shows the power dissipation relate to the cavity material, which is characterized by  $Q_0$ , and the cavity geometry, which is characterized by  $R_{sh}/Q_0$ . For the superconducting cavity,  $Q_0$  is of the order of  $10^{10}$ , so the dissipated power is no longer a major issue. Reduction of the  $R_{sh}/Q_0$  can drop the beam interacts with the cavity and improve the beam quality.

Substituting Eqn 3.9 into 3.2, the average accelerating electric field is expressed as

$$E_{acc} = \frac{1}{l} \sqrt{\frac{R_{sh}}{Q_0}} \sqrt{\omega U_0} = \frac{1}{l} \sqrt{\frac{R_{sh}}{Q_0}} \cdot \sqrt{Q_0 P_{loss}} \quad (0.10)$$

Eqn. 3.10 is usually used in cavity tests.  $R_{sh}/Q_0$  is obtained from Superfish simulation.  $Q_0$  and  $P_{loss}$  can be calculated from measured decay time, frequency, input power, pickup power and reflected power.

The peak field is of interest in gun tests, so Eqn. 3.10 can be changed to

$$E_{cathode} = \kappa [MVm^{-1} J^{-1/2}] \sqrt{U_0} = \kappa [Vm^{-1} W^{-1/2}] \sqrt{\omega U_0} \quad (0.11)$$

The  $\kappa$  is obtained from Superfish simulation. The  $\kappa$  is equal to 21.34 [MV m<sup>-1</sup> J<sup>-1/2</sup>] or 238.5 [Vm<sup>-1</sup> W<sup>-1/2</sup>] for BNL 1.3 GHz plug gun.

#### 3.1.4. Antenna couplers

The power coupler serves to transfer RF power from the RF power source to the cavity and to the beam. The input coupler helps to match the impedance of cavity with beam to the impedance of RF power source. Usually, the SRF cavity is equipped with the input coupler, pick up coupler and HOM coupler for high current operation. For the BNL 1.3 GHz gun, which operate at low current, HOM coupler is dispensable. The couplers used in BNL 1.3 GHz gun are shown on Figure 3.6.



**Figure 3.6 The input coupler and pickup coupler for the gun.**

For the gun without beam loading, the input power ( $P_{in}$ ) will be the sum of the power dissipated in the cavity wall, the power reflected from input coupler ( $P_r$ ) and the power that leaks out the pick up coupler ( $P_t$ ).

$$P_{in} = P_{loss} + P_r + P_t \quad (0.12)$$

We define loaded quality factor, input coupler external quality factor and pick up coupler external quality as

$$\begin{aligned} Q_L &= \frac{\omega U}{P_{in}} \\ Q_e &= \frac{\omega U}{P_e} \\ Q_t &= \frac{\omega U}{P_t} \end{aligned} \quad (0.13)$$

Substituting Eqn. 3.13 into Eqn. 3.12, one obtains an expression

$$\frac{1}{Q_L} = \frac{1}{Q_e} + \frac{1}{Q_0} + \frac{1}{Q_t} \quad (0.14)$$

Then the coupling parameter can be defined as

$$\begin{aligned} \beta_e &= \frac{Q_0}{Q_e} = \frac{P_e}{P_{loss}} \\ \beta_t &= \frac{Q_0}{Q_t} = \frac{P_t}{P_{loss}} \end{aligned} \quad (0.15)$$

$\beta$  describe how strong the couplers interact with the cavity.

For the input coupler, the reflection coefficient is

$$\Gamma = \sqrt{\frac{P_r}{P_i}} \quad (0.16)$$

The coupling parameter of the input coupler is given by

Undercoupled:  $\beta = \frac{1-\Gamma}{1+\Gamma}$

Overcoupled: 
$$b = \frac{1+G}{1-G} \quad (0.17)$$

From 3.16 and 3.17 we can see when  $\beta = 1$  the cavity perfectly matched to the coupler due to zero reflection.

The state of cavity wall changes from normal conducting to superconducting when the SRF gun is cooling down. The dissipated power in the gun is decreased dramatically and  $Q_0$  is increased. Meanwhile, the length of the coupler antenna is constant, so the power leak out from the coupler is constant. The external  $Q$  is same while the gun is cooling down.

$$Q_e P_e = Q_0 P_{loss} \quad (0.18)$$

In the SRF gun, the input coupler usually sits on the beam pipe. The beam pipe cut off frequency is above the fundamental mode and the cavity's impedance is closed to zero. With such design, the impedance of RF source is matched to the impedance of combined gun and beam pipe.

The voltage of the gun is 0.6 MV for the parameter listed on Table 3.2. The beam load power is 3 W. Based on the 2 K test result, the  $Q_0$  of the gun is in the range of  $2 \cdot 10^8$  to  $6 \cdot 10^8$ . The input power for the beam load test is 6.5 W calculated with the parameters listed on Table 3.1. The external  $Q$  of the input coupler was chosen  $1 \cdot 10^8$ .

The Figure 3.7 shows that the external  $Q$  of input coupler is exponentially changes with the length of antenna.

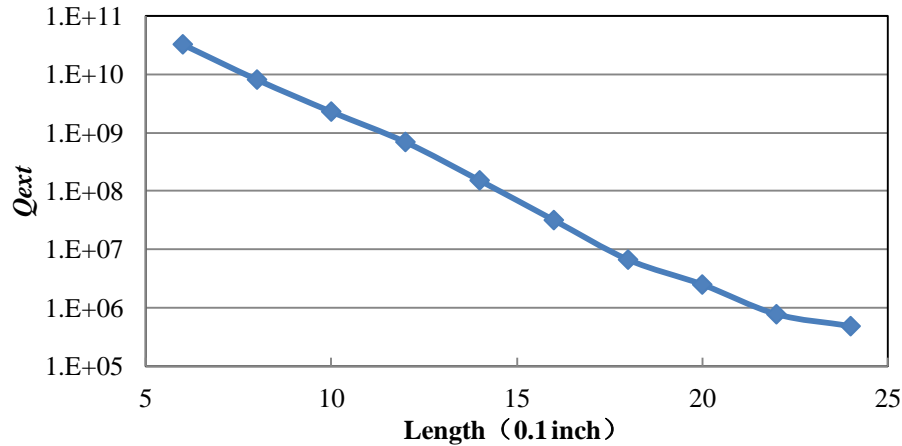


**Figure 3.7** The external  $Q$  of input coupler changed by the length of antenna.

The antenna's length change ranges from 1.3 inches to 1.7 inches which response to the range of external  $Q$  of input coupler from  $5 \times 10^8$  to  $1 \times 10^7$ . The input coupler was set to 1.4 inches which response to  $1 \times 10^8$  of  $Q$  external. The pickup antenna's length was set to 0.3 inches which response to  $2 \times 10^{11}$  of  $Q$  external.

## 3.2. Heat generation from GaAs photocathode SRF gun

### 3.2.1. SRF gun test in 2 K

The heat load of GaAs photocathode in RF field is significant when operated in the SRF gun. Particularly, the heat generation from the cathode will quench the gun without the choke filter. The characteristics of heavily  $p$  doped GaAs photocathode in RF guns haven't been studied yet. The gun was tested at 2 K at JLab. We compared the  $Q_0$  of the SRF gun with or without the GaAs crystal to study the heat generation from the GaAs.

The SRF gun was treated following the steps listed below:

1. Buffered chemical polishing:  $\text{HNO}_3:\text{H}_3\text{PO}_4:\text{HF} = 1:1:1$ ; temperature: 21 °C; cavity wall was etched 10  $\mu\text{m}$ ; GaAs holder was etched 20  $\mu\text{m}$  due to contaminated; coupler pins were etched 5  $\mu\text{m}$ .
2. High pressure ringing: 1 hour.
3. Dried the gun in a class 10 clean room for 24 hours.
4. Assemble the photocathode holder and couplers in the clean room. The  $Q_e$  of the pickup coupler is  $1 \times 10^{12}$  and the  $Q_e$  of input coupler is  $1 \times 10^9$ .

5. Leak detection and pump the vacuum of the gun to  $10 \times 10^{-9}$  torr.
6. Cool down.

The  $Q_0$  of SRF gun is usually higher than  $10^9$ , so the bandwidth is very small. The fundamental frequency would be changing due to Lorentz force effects and microphonics. There are two different ways to provide a low level RF drive signal to the gun. The first way is tuning the mechanical length of the gun by piezo crystals or a motor with the fixed RF system frequency. The second way is to make use of a LLRF system to track the cavity frequency [50]. The LLRF system tracks the frequency shifts and the cavity gradient is always maximum for given forward power. The voltage controlled oscillators configured in a phase locked loops (VCO-PLLs) system is used in the vertical test lab at JLab. Figure 3.8 shows a block diagram for the VCO-PLL system.

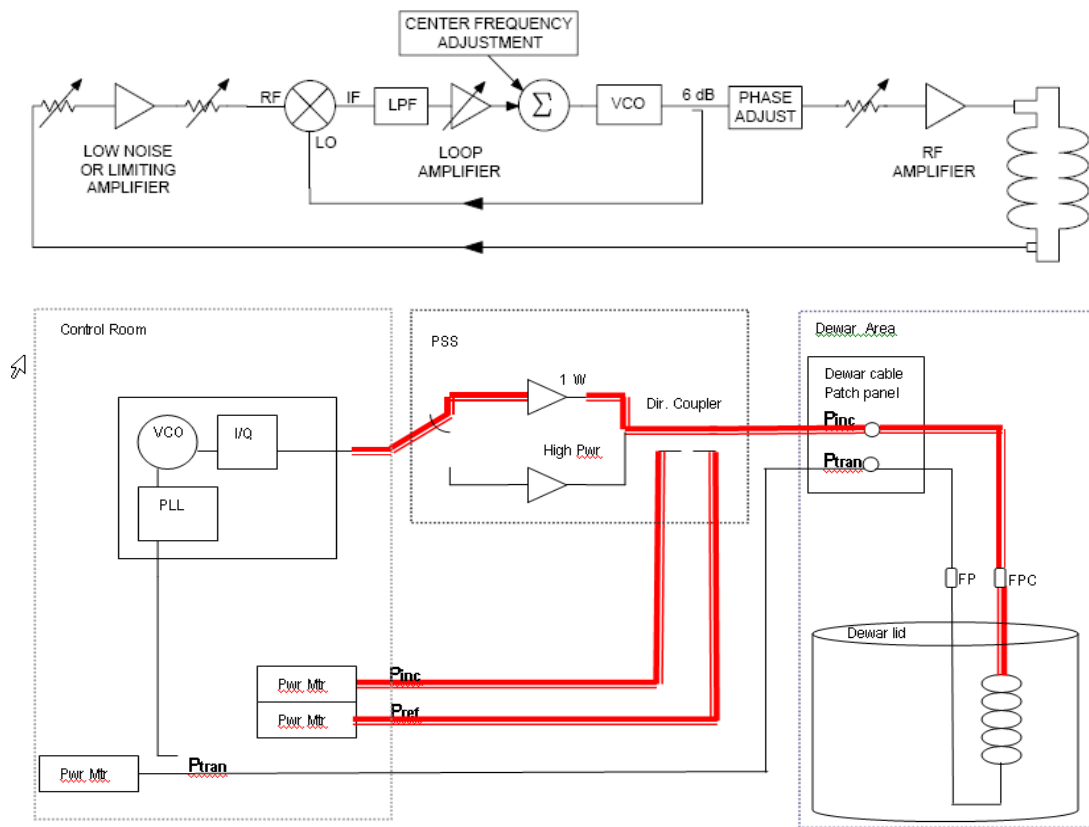


**Figure 3.8 a) Block diagram of the VCO-PLL system used at JLab [50]; b) Block diagram of the RF circuits for gun testing**

The LLRF loop includes a phase shifter, variable attenuator, mixer, low noise amplifier, low pass filter and VCO, which is provided by an RF signal source such as Agilent

E4422B. Three power meters are used for the input power, pickup power and reflection power measurement. The decay time is measured from an oscilloscope trace of a crystal detector signal. The frequency is read from a RF frequency counter.

The power measured by the power meters is not the true power at the cavity, all the cables have to be calibrated due to power dissipation. The correct power is obtained from the measured power times to the calibration factor. The approximate frequency is measured by a network analyzer.

$$\begin{aligned}
 P_{in\_correct} &= P_{in\_measure} \times C_{in} \\
 P_{re\_correct} &= P_{re\_measure} \times C_{re} \\
 P_{t\_correct} &= P_{t\_measure} \times C_t
 \end{aligned}
 \tag{0.19}$$

The decay measurement is used in BNL plug gun test. The steps are listed as follows.

1. Adjust the central frequency to the frequency measured by the network analyzer.
2. Adjust the phase shifter until the reflection power is minimum and lock the RF phase.
3. Pulse the RF power on and off to determine if the gun is over coupled or under coupled. For a rectangular driver pulse, the first peak is higher than second peak and the reflection power doesn't go to zero when the gun is under coupled. The first peak is lower than second peak when the gun is over coupled. When the gun is critically coupled, the leading and trailing peaks are of equal magnitude and the reflected power goes to zero.
4. Increase the input power by tuning the variable attenuator and log the data such as frequency, forward power, pickup power, reflection power.
5. Cut off the switch and obtain the decay curve from scope.
6. Calculate the external  $Q$ . Given the constant external  $Q$ , increase the input power and calculate the peak field.

The decay measurement formulas are presented as follows.

From Eqn. 3.17, the coupling of input coupler ( $\beta_e^*$ ) looking from input coupler to the cavity is given by

$$\beta_e^* = \frac{Q_0^*}{Q_e}$$

$$Q_0^* = \frac{\omega U}{P_{loss}^*} = \frac{\omega U}{P_{loss} + P_t} = \frac{Q_0}{1 + \beta_t} \quad (0.20)$$

The power loss includes the dissipated power and power leaking from pick up  $P_t$ .

Combine Eqn. 3.14 and Eqn. 3.20,  $Q_L$  is presented by

$$\frac{1}{Q_L} = \frac{1}{Q_e} + \frac{1}{Q_0^*} = \frac{1}{Q_0^*} (1 + \beta_e^*) \quad (0.21)$$

Substitute Eqn. 3.20 into Eqn. 3.21

$$Q_0 = Q_L \times (1 + \beta_t) \times (1 + \beta_e^*) = Q_L \times (1 + \beta_e^* (1 + \beta_t) + \beta_t) \quad (0.22)$$

Where  $\beta_t$  and  $P_{loss}$  are obtained from Eqn. 3.12 and Eqn. 3.15. Eqn. 3.22 shows how to obtain  $Q_0$  from  $Q_L$ . Drive from Eqn. 3.20, we can get

$$\beta_e^* (1 + \beta_t) = \frac{Q_0}{Q_e} = \frac{P_e}{P_{loss}} = \beta_e \quad (0.23)$$

So Eqn. 3.22 is simplified to

$$Q_0 = Q_L \times (1 + \beta_e + \beta_t) \quad (0.24)$$

Decay time is obtained by fitting the decay curve by

$$P_t(t) = P_t(0) \exp\left(\frac{-\omega \times t}{Q_L}\right) \quad (0.25)$$

When the  $P_t$  decrease to half of the maximum, the time is  $\tau_{1/2}$

$$P_t(\tau_{1/2}) = \frac{1}{2} P_t(0) = P_t(0) \exp\left(\frac{-\omega \times \tau_{1/2}}{Q_L}\right) \quad (0.26)$$

Then

$$Q_L = \omega \frac{\tau_{1/2}}{\ln(2)} \quad (0.27)$$

the  $Q$  factor can be obtained from Eqn. 3.24 after we know  $Q_L, \beta_e, \beta_t$ . Eqn. 3.11 can be rewritten as

$$E_{cathode} = \kappa \sqrt{\omega U} = \kappa \sqrt{P_t Q_t} = \kappa \sqrt{P_{loss} Q_0} \quad (0.28)$$

For BNL plug gun, the maximum field on the axis is on the photocathode. So  $E_{cathode} = E_{peak}$ .

The input coupler used in BNL plug gun was indentified as under coupled. The measured data is presented below.

1. Calibration

$C_{in}$	$C_{re}$	$C_{tr}$
1290	904	28.5

2. Reading from power meters, frequency counter and scope.

$P_{in}$	$P_r$	$P_t$	$F$ (MHz)	coupling	$\tau$
5.61E-4W	2.58E-4W	3.29E-4W	1298.94	Under coupled	0.297s

3. Correct power and calculated QL and power dissipated

$P_{in\_c}$	$P_{r\_c}$	$P_{t\_c}$	$Q_L$	$P_{loss}$
0.72 W	0.23 W	0.01 W	2.87E9	0.48 W

4. Calculated coupling, external Q, Q factor and peak field

$\beta^*$	$\beta_e$	$\beta_t$	$Q_t$	$Q_0$	$E_{peak}$
0.275	0.28	0.0196	1.9E11	3.73E9	9.89 MV/m

The gun without GaAs was tested at 2 K initially. Figure 3.9 shows the  $Q_0$  response to  $E_{cathode}$ .

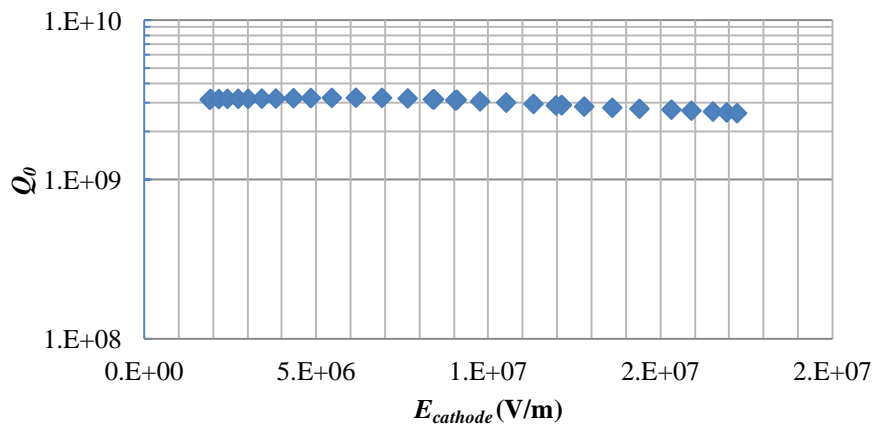
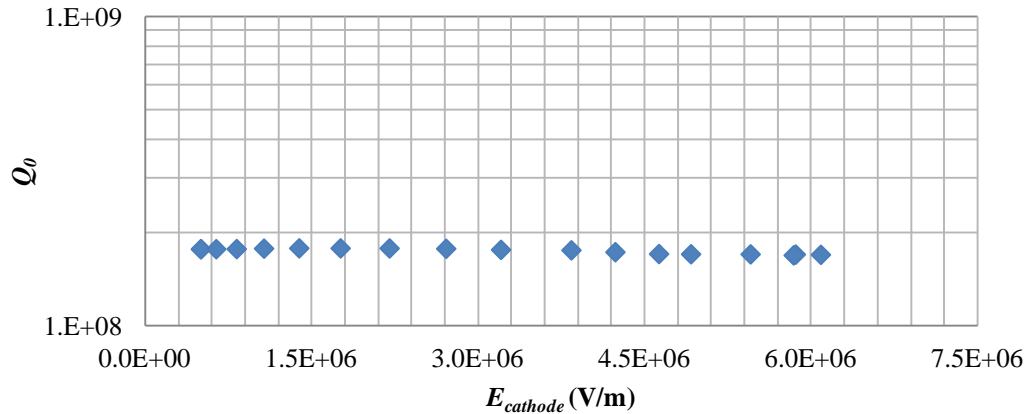


Figure 3.9 The  $Q_0$  response to  $E_{cathode}$  when the plug gun without GaAs.

A 2.2 mm \* 2.2 mm heavy  $p$  doped GaAs crystal is welded on the Nb plug and inserted into the gun. Figure 3.10 shows the GaAs with the plug.



**Figure 3.10 GaAs crystal welded on the plug by indium.**



**Figure 3.11 Quality factor vs. gradient of BNL plug gun with GaAs at 2 K.**

During the second cool-down, a GaAs cathode in size of 2 mm \* 2 mm \* 0.6 mm was used, and the  $Q_0$  dropped from  $3 \cdot 10^9$  to  $1.78 \cdot 10^8$ . In the DC gun, the temperature rising of the GaAs photocathode comes from the laser power. In the RF gun, not only does the laser power induce the heat rise, but also the electric field penetrates into the GaAs cathode, causing dielectric losses, the magnetic field will induce the surface current to generate the heat. That is the reason why  $Q_0$  is low in the SRF gun with the GaAs crystal. The flatness of the  $Q_0$  curve with the GaAs cathode indicates that the cavity and plug did not quench in the field lower than 7 MV/m. However, the drop was much larger than initially estimated. A careful analysis is necessary.

### 3.2.2. GaAs crystal heat generation in SRF gun

The GaAs crystal used for the photocathode is a zinc doped ( $p$  type) one with a heavy doping of  $3 \cdot 10^{18} \text{ cm}^{-3}$  to prevent the build-up of charge on the surface, viz., NEA surface. The GaAs wafer has an active area of 2 mm by 2 mm and is of 0.6 mm thick. The resistive heat load of the GaAs crystal cannot be neglected due to the high  $p$ -doping of the crystal. The dissipated power per unit area due to Joule heating is

$$P_c = \frac{1}{2} R_s \int_s |H|^2 ds \quad (0.29)$$

The surface resistance  $R_s = \frac{1}{\sigma \delta}$  can be calculated from the skin's depth  $\delta = \sqrt{\frac{2}{\sigma \mu \omega}}$  and the resistivity of GaAs. To model the heat load from the GaAs crystal correctly it is essential to know the resistivity of GaAs at 4 K. The manufacturer specifies it as  $3.4 \cdot 10^{-2} \Omega\text{-cm}$  at 290 K. The GaAs photocathode resistivity measurement was done by the Magnet Division at BNL. The four point probe which avoids the impedance of the connection of the probe to the GaAs wafer is a simple apparatus for measuring the resistivity of GaAs samples. By passing a current through two side probes and measuring the voltage through the inner probes allows measuring substrate resistivity [51]. Figure 3.12 shows the home made four point probe measurement device.

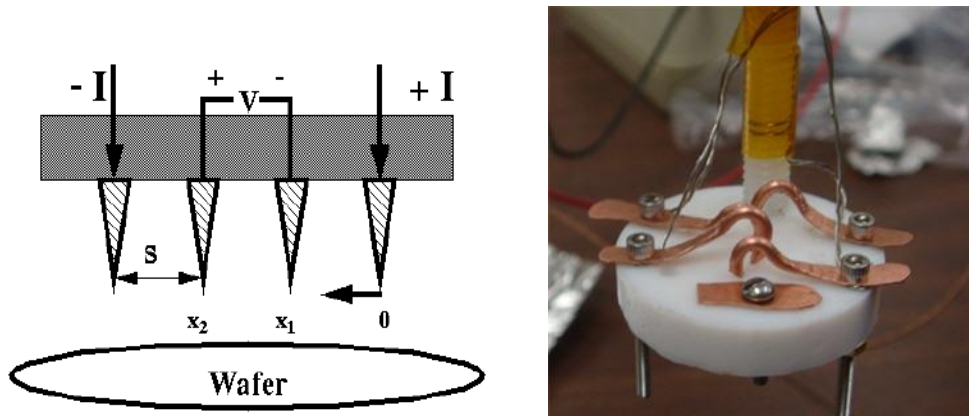


Figure 3.12 The four point probe resistivity measurement device

By using the four point probe method, the semiconductor sheet resistivity can be calculated by

$$\text{Resistivity}[\Omega - m] = \text{Geometry Factor}[m] \times \frac{U[V]}{I[A]} \quad (0.30)$$

Where  $U$  is the voltage reading from the voltage meter,  $I$  is the current carried by the current carrying probes. Geometry factor is independent on temperature. The geometry factor was obtained by measuring the resistance via our device and the resistivity in room temperature which provided by the sample vendor specification. The resistivity of GaAs is  $3.4 \times 10^{-4}$  Ohm-m. The resistance measured in room temperature is 0.126 Ohm. Then we obtain that the geometry factor is 0.27 cm. Figure 3.13 shows the resistance measurement and measured resistivity during the cool-down to 4 K.

To get an accurate result, the temperature of GaAs is dropped very carefully. The temperature drop from 300 K to 4 K takes 6 hours, and the temperature rises through all the night. The result measured during cool down has vibration because of difficult control. Then the GaAs resistivity curve was measured when the temperature rises.

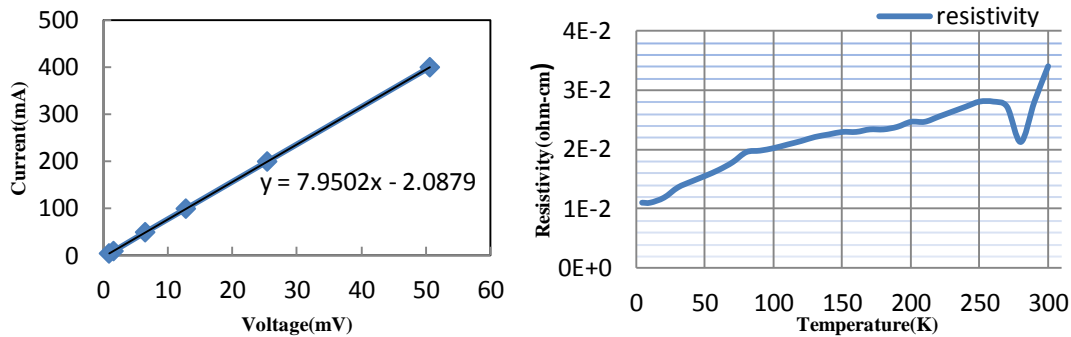


**Figure 3.13 The GaAs resistivity vs. the temperature from 300 K to 4 K. At 300 K, the resistivity of  $3E18$  Zn doped GaAs is  $3.4E-2$   $\Omega$ -cm. The resistivity of GaAs decreases to  $1.1E-2$   $\Omega$ -cm at 4 K.**

Figure 3.13 shows the measured resistivity during the cool-down to 4 K. As the doping increases, a larger number of holes are forbidden to participate in hole-electron scattering because the Fermi level moves deeper into the valance band with most states below the Fermi energy being occupied. There is little variation with the temperature, as in GaAs the Fermi level is below the valance level. At 4 K, the resistivity is  $1.1 \times 10^{-2}$   $\Omega$ -cm.

Knowing the resistivity of the gun's boundary and gun's geometry, the surface magnetic field can be calculated using the computer code SUPERFISH. To compare these findings

with the experimental ones, the peak field is normalized to 5 MV/m. Table 3.3 shows the GaAs parameters used in the simulation and calculation.

**Table 3.3 GaAs photocathode parameters.**

Parameter	Value
Thickness	0.6 mm
Carrier concentration	$3 \cdot 10^{18}/\text{c.c}(\text{Zn})$
Surface Peak Field	5 MV/m
Size	2 mm*2 mm
Loss tangent	0.06
Permeability	12.9
Permittivity	12.36

The magnet field simulated by the Superfish is shown on Figure 3.14. The resistivity of surface of GaAs crystal is set to  $1.1 \cdot 10^{-2}$  Ohm-cm. The edge 1 and 2 in Fig 3.14a is set as GaAs surface. Meanwhile, the edge 3 and 4 it set as normal conductor Indium and the resistivity of indium is  $8.6 \cdot 10^{-6}$  Ohm-cm. The other part of the gun is set as superconducting niobium.

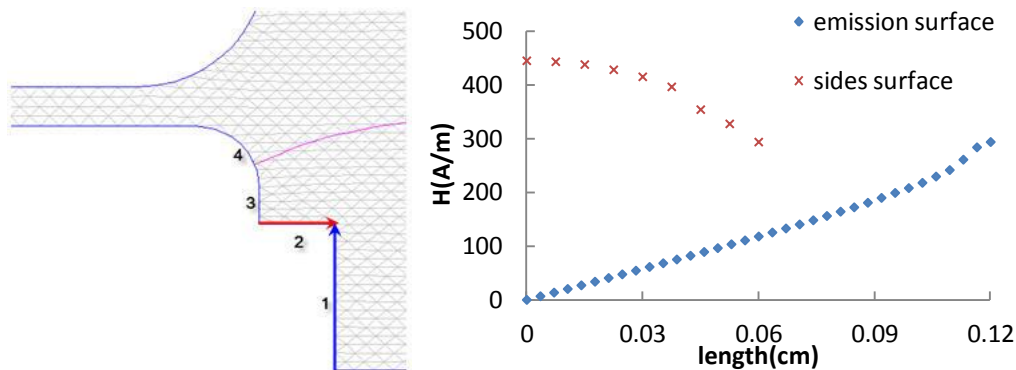


**Figure 3.14 a) The model simulated by Superfish; b) the magnet field magnitude obtained from Superfish. The side surface response to arrow 2 in a) and emission surface response to arrow 1 in a).**

The magnet field increases linearly from the center of crystal to its edges. With the value of the magnetic field and surface resistance, the resistive heat load is calculated and finds that a 200 mW heat load is generated from the emission surface of GaAs crystal and 1 W from its

edge. The GaAs surface heat load in the RF field depends on the doping level. The total heat generated from the GaAs surface is 1.2 W when the gun's peak field is 5 MV/m. The heat load from four edges is listed in Table 3.4.

**Table 3.4 The heat load from four segments defined in Superfish**

Segment	Power (mW)
1	196.8
2	928.1
3	4.389
4	14.25

GaAs experiences a dielectric loss (independent of the doping level) when the RF field penetrates into the crystal [52]. So the heat load due to dielectric loss is called body heat load.

The power loss in the semiconductor body is [53].

$$P = \int \omega \cdot \varepsilon \cdot A \cdot E(x)^2 \cdot \frac{\varepsilon_1}{\varepsilon_2} dx \quad (0.31)$$

where  $A$  is the area and  $d$  is the thickness of the GaAs surface.  $E$  is the electrical field,  $\omega$  is the frequency of the field,  $\varepsilon_1/\varepsilon_2$  is the loss tangent of GaAs and  $x$  is the field location in the depth of GaAs. There also is a magnetic component to the power loss, but it is much smaller than the electric part in the photocathode location. So it can be neglected. The electrical field drops exponentially with the depth:

$$E(x) = E_0 e^{-\frac{x}{\delta}} \quad (0.32)$$

with the photocathode peak field  $E_0 = 5$  MV/m and the parameter in Table 1, 230 mW of heat will be generated inside the GaAs wafer. The total heat load due to resistive and dielectric losses in GaAs is 1.43 W at 5 MV/m. The gun's stored energy is 3.25E-2 J, so  $Q_0$  will drop to 1.8E8, which matches the test results well. The detail heat load results are shown on Table 3.5.

**Table 3.5 Heat load from the SRF gun with GaAs.**

	Resisivity (Ohm-cm)	Simulated heat load with GaAs (mW)	Heat load measurement with GaAs (mW)	Heat load measurement without GaAs (mW)
GaAs emission surface	1.10E-02	196.8	1868	
GaAs side	1.10E-02	928.1		
GaAs body	N/A	231		
Nb		89	132	132
In	8.60E-06	18		
total		1462	2000	132
frequency				1.30E+09
$Q$		1.82E+08	1.78E+08	3.00E+09

From this table, one can see that the heat generated by the GaAs edge is dominated in the gun heat load as the model. The emission surface heat generation occupied 13% of total heat load and this part of heat load have to be existed. The heat load comes from the edge of GaAs occupied 63% which can be eliminated by improve the photocathode holder. Decrease the heat load from the photocathode is a major step to test the SRF gun.

### 3.2.3. GaAs photocathode holder design

There are two methods to eliminate the heat generation from the GaAs. One is using thin GaAs wafer. Another is designing a GaAs holder which can shield the magnetic field on the GaAs.

Table 3.6 shows the heat load from various thickness diamonds when the peak field is 5 MV/m. The heat generation from side edge of GaAs crystal doesn't dominate when adopt a piece with 0.1 mm thickness. We used 0.1 mm GaAs samples which are the thinnest piece AXT. Crop can provide at later experiment.

**Table 3.6 The heat generation from various thickness diamonds**

	Heat load (mW) 0.6 mm	Heat load (mW) 0.3 mm	Heat load (mW) 0.1 mm

emission	196	143	124
side	928	234	112
dielectric	231	188	161
$Q_0$	1.81E+08	3.95E+08	5.26E+08

The model shows that a large part of the heat load comes from the edge of GaAs crystal. The plug therefore can be improved by shielding the crystal's edges from the RF fields. In our new design, the GaAs crystal is recessed into the niobium plug. The recess was machined into the plug's surface by Electron Discharge Machining. The GaAs crystal is mounted on the plug with a small amount of Indium solder, carefully limiting it to the back side of the crystal so that no indium is exposed to the RF field.

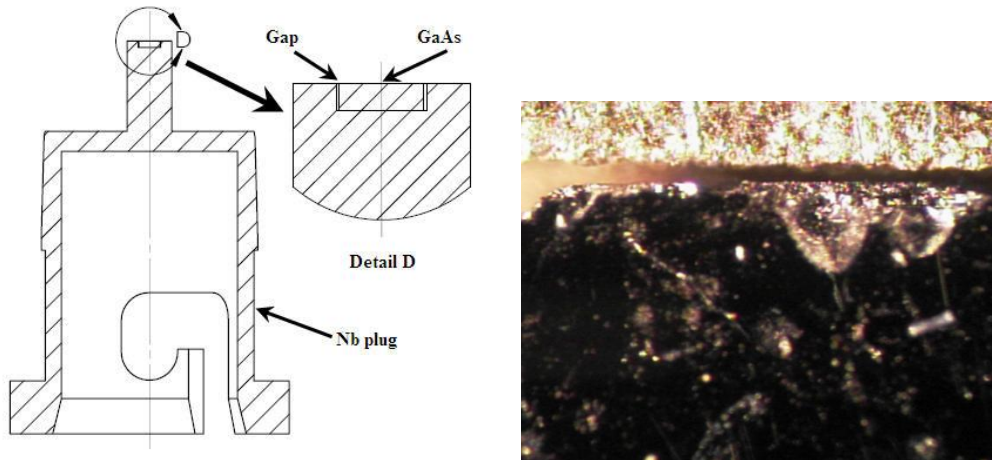


**Figure 3.15 a) The drawing of Nb plug with GaAs photocathode. The upper right corner of the drawing is the detail of recess structure. There is a 200  $\mu\text{m}$  gap left between the GaAs edge and niobium due to the machine tolerance; b) The photo of the gap between GaAs and Nb.**

Because of machining tolerances, there is a small gap remaining between the edge of the crystal and the niobium. Depending on the gap's size, the magnetic field exists there and generates heat. The simulation estimated the heat load due to the machine tolerance. Figure 3.16 shows the magnetic field on the GaAs simulated by Superfish and Figure 3.17 shows the heat generation response to length of gap. The best method is first to cut the GaAs crystal and then machine the recess to match the crystal size. In this way the gap can be as small as 200  $\mu\text{m}$  and  $Q_0$  can reach  $6 \cdot 10^8$ . The procedure of plug making has been proved.

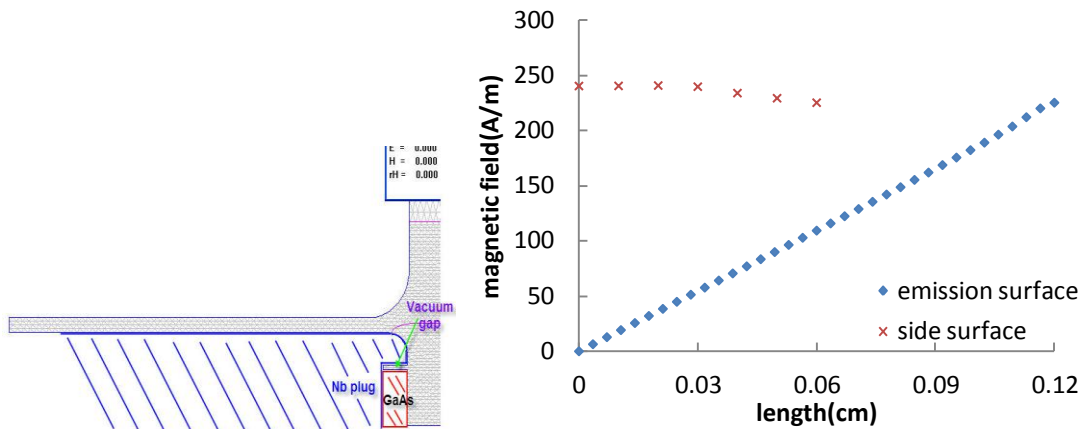


**Figure 3.16** The recess structure of GaAs holder and magnetic field on the GaAs surface. The side surface response to arrow 2 in a) and emission surface response to arrow1 in a).

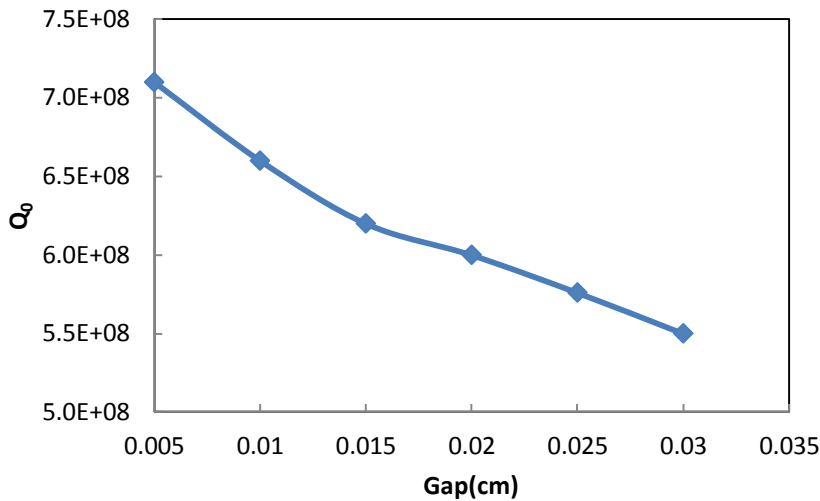


**Figure 3.17** The  $Q$  of the gun response to the gap between Nb and GaAs.

For the SRF gun, the gradient at the cathode is limited by the superconductor quench around the cathode. The cathode's emission surface has high electric field that generates the heat power on the photocathode, as discussed earlier. The heat from the cathode flows to the Nb plug, if the plug temperature rises above the critical temperature,  $Q_0$  will drop. If the heat power from the GaAs cannot be absorbed by the LHe effectively, the quench area will be increased and the whole gun will be quenched.

The calculations showed that the power absorbed by the GaAs crystal dominates the heat load. Accordingly, the plug must be cooled sufficiently. The path length from the cathode to the liquid helium is about 1 cm. A thermal finite element analysis (FEA) using ANSYS 10.0 is undertaken to evaluate the relationship between the thermal flow to plug and the gun's geometry.

Since the RF loss on the cavity wall is 7% of the loss in the GaAs crystal, the former in the simulation is ignored. The heat load from the GaAs crystal depends on the stored energy in RF field. The FEA model included the cathode, half of the SRF cavity, and the geometry of the cathode's socket geometry. A mechanical clamp pressed the cathode plug against the cavity, the thermal contact resistance is existent between the cathode and the cavity, assuming a pressure of 10 psi on the contact surface.

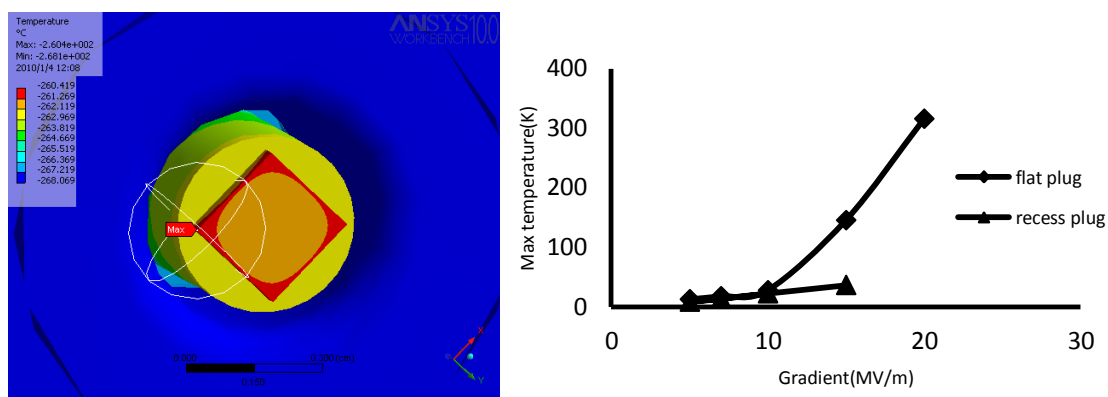


**Figure 3.18 The GaAs crystal temperature simulation with two kinds of plug designing. The square curve shows the GaAs's peak temperature of the original plug design. The GaAs peak temperature reaches 150 K at 15 MV/m which is the design peak field. The triangle curve is the peak temperature of recess structure design. The GaAs peak temperature is 38 K at 15 MV/m.**

The analysis indicates that at the temperature of 4 K, the original plug design will quench when the cathode is above a 6 MV/m peak field. The new, recessed cathode plug can operate up to 13 MV/m, which is the design gradient for this experiment (Figure 3.18). For higher gradients, a gun with a choke structure should be used, it allows the cathode to reach higher temperatures and be cooled with liquid nitrogen. However, the choke joint structure design is still ongoing. Multipacting effect occurring in the choke joint is a barrier for use in BNL 1.3 GHz SRF gun.

### 3.3. Temporal response of GaAs photocathode in RF gun

The temporal response of photocathode is very important in the applications of an SRF gun. The simulation shows the 10 ps response time makes the efficient acceleration in a 1.3 GHz gun [54]. The time response is determined by the time spread between photo excitation and emission of electrons into the vacuum. In a photo cathode with a very short active region, the electrons produced by the laser pulse have a very small probability of interacting with each other before they are photoemitted. The escape of electrons from deeper in the material is due primarily to diffusion. However, in the RF gun it is sped up by the RF field penetrating into the cathode. Hartmann and his colleagues formulated a diffusion model to explain the bunch length in the DC gun [55]; that agreed well with the measurements and showed that the emission has a long [56]. In RF gun, the field-driven drift must be considered in describing its motion. The Fokker-Planck equation yields solution including both the drift and diffusion.

Electrons that are free to move in the conduction band of the cathode in the RF gun experience several forces such as temperature gradient, RF fields and gradients in charge density.

The average particle's current density due to electric fields and diffusion is given by

$$\vec{J} = pq\mu\vec{E} + qD\nabla p \quad (0.33)$$

Where  $p$  is the average electron's density,  $q$  is the electric charge,  $\mu$  is the electron's mobility,  $D$  is the diffusion constant and  $E$  is the electric field in the crystal.

With the three-step model, the movement of electrons in semiconductor is described by

$$\frac{\partial p(r,t)}{\partial t} = G(r,t) - \frac{p(r,t)}{\tau} + \frac{\nabla \cdot \vec{J}}{q} \quad (0.34)$$

The first term on the right side is a generation term. The crystal absorbs an incident laser pulse of intensity  $I_0$  and Gaussian temporal shape.

$$G(z,t) = (1-r)I_0 e^{-[t-t_0/\tau_0]^2} e^{-\alpha z} \quad (0.35)$$

$\alpha$  determines the absorption coefficient of the crystal.  $I_0$  is the intensity of the laser pulse incident in the semiconductor. The second term represents electron annihilation wherein  $\tau$  is the electron's lifetime. The third term describes the electron displacement of electrons by diffusion and drift. The  $\alpha$  and diffusion constant depend upon temperature and doping concentration of wafer.

Making the following simplifications and assumptions gives us an equation with the initial and the boundary conditions. 1) The diameter of laser spot at the cathode usually is larger than absorption length. So, a one-dimensional model describes the diffusion and drift. 2) The electron's recombination lifetime is orders of magnitude larger than the bunch length  $\frac{p(r,t)}{\tau} \ll 1$  [57]. 3) In regions of no generation, the photo generation term is 0. In other places, it is expressed as the initial condition:  $p(x,t=0) = p_0 e^{-\alpha x}$  for  $x \in [0,h]$  (0.36). 4) Negative electron affinity photoemitter with a band bending region at its activated surface.

Due to the surface effect, either most electrons that reach the semiconductor's surface lose energy in the bending region, becoming trapped at the surface or they are emitted from the cathode. However, they cannot diffuse back into the bulk. This fact can be taken into account by assuming a layer of limited thickness  $h$  with  $p(x,t)=0$  on both surfaces of the layer.

$P = 0$  for  $t > 0$  and  $x = 0$  and  $x = h$

Then the simplified equation can be expressed as

$$\frac{\partial p(r,t)}{\partial t} = -\frac{\partial}{\partial r} [\mu(r)E_r p(r,t)] + D(r) \frac{\partial^2 p(r,t)}{\partial r^2} \quad (0.37)$$

Where  $\mu(r)$  is the function of field and  $E_r$  is the field magnitude meet by the electrons. The first term is the drift term and second is the diffusion term. It is a diffusion equation with an additional first order derivative with respect to  $x$ .  $\varphi$  is the initial RF phase at the emission surface.

The drift velocity response to field is shown on Figure 3.19.

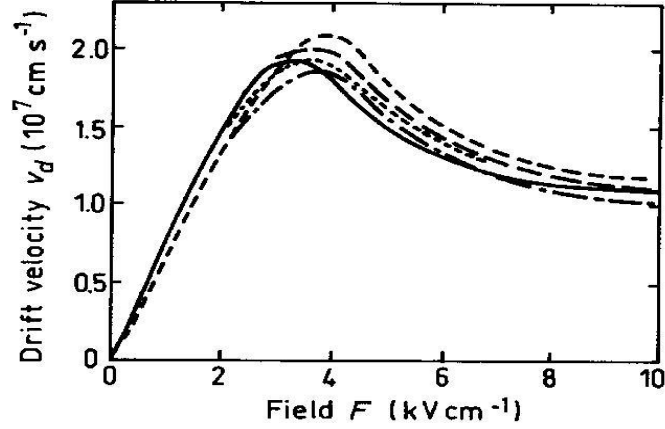


**Figure 3.19** The drift velocity response to the electric field in GaAs. The different curves are from data obtained by different person [58, 59].

In the low field, the drift velocity is multiplied by the electric field with mobility. However, in the high field, the relationship of drift velocity and electric field is non-linear.

By polynomial fitting, the electric field response to the drift velocity is given by

$$\begin{aligned} \mu E_x &= 0.0217 + 0.4839E_x + 0.4978E_x^2 - 0.2706E_x^3 + 0.518E_x^4 \\ E_{in} &= \frac{E_{peak}}{\varepsilon} \\ E_x &= E_{in} e^{-\frac{x}{\delta}} e^{i(\omega t + \phi)} \end{aligned} \quad (0.38)$$

We obtain the total number of electrons concentrated in the layer by integrating the electron destiny distribution. Assuming the entire electron that reaches the surface of crystal leave it because of NEA the emitted photocurrent is determined via the differentiation of the number of electrons in the crystal with time.

$$\begin{aligned} N(t) &= \int_0^h p(x, t) dx \\ I(t) &= \frac{\partial}{\partial t} N(t) = \frac{\partial}{\partial t} \int_0^h p(x, t) dx \end{aligned} \quad (0.39)$$

To numerically solve the Equation, we used the initial conditions shown in the Table 3.7.

**Table 3.7 GaAs Parameters**

Laser absorbtion	7000 cm-1
------------------	-----------

coeffiention (780 nm)	
Electron mobility	2000 cm <sup>2</sup> /v.s
Diffusion coeffiention	30 cm <sup>2</sup> /s
Thickness	100 um
Frequency	1.3 GHz
$E_0$	15 MV/m
Permittivity	12.36
Resistivity in 4 K	1.1E-2 Ohm-cm
Permeability	12.4

In the RF gun, the coefficient of first term of Eqn. 3.37 is in order of  $10^7$  cm/s and the coefficient of the second term is 30 cm<sup>2</sup>/s. So we can conclude that the drift dominates the electrons' movements in a RF gun. Applying the Eqn. 3.39 we find that the temporal response of the GaAs photocathode is in the hundreds of femtoseconds for a delta function laser pulse (Fig 3.20). The heave  $p$  doped GaAs crystal, the electron mobility achieve the maximum at 100 K. The electron mobility in 4 K is higher than which in room temperature. The electron mobility used in this model is obtained from room temperature measurement. The tail of electron bunch should even small in cryogenic, particular in SRF gun.

We show for the first time a sub-ps electron bunch can be created from a GaAs cathode in an RF gun. The ultra-short time response of GaAs photocathode in the RF gun eliminates the bombardment and minimizes both the bunch energy spread and emittance. Another advantage is the bunch can be shaped by the laser pulse very easily to minimize the space charge effect. Therefore, the electron beam generation from RF gun based on GaAs photocathode may be another opinion for high power FEL.

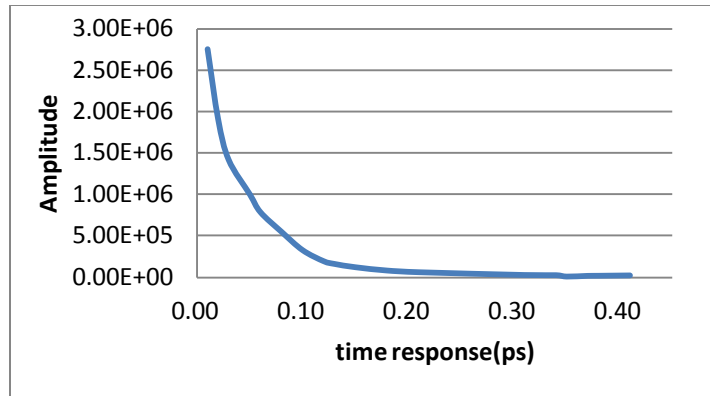


**Figure 3.20 The temporal response of GaAs photocathode for use in 1.3 GHz gun at room temperature.**

### 3.4. Electron back bombardment in RF gun

#### 3.4.1 Electron back bombardment in RF gun

The electron back bombardment is usually happened in RF gun. In the RF gun, the electron are emitted in one half of an RF cycle, those emitted near the other half become back streaming before they exit the gun due to the electron phase shift response to RF phase. These back streaming electrons hit the cathode emission surface, over heating the cathode such as thermionic gun resulting in a rampant emission or break the emission surface such as photocathode gun resulting in decrease cathode lifetime [60]. The NEA photocathodes usually have very high secondary electron emission, so multipacting may happen on the photocathode surface and killing the cathode. The GaAs cathode's lifetime was 10 seconds in the experiments at BINP. The analyze show such short lifetime is due to the multipacting.

The longitudinal motion of an electron in an RF gun depends on its initial emission phase leaving the cathode. Fig 3.21 shows the traces of electrons in RF gun with different intial phase simulated by CST Particle Studio.

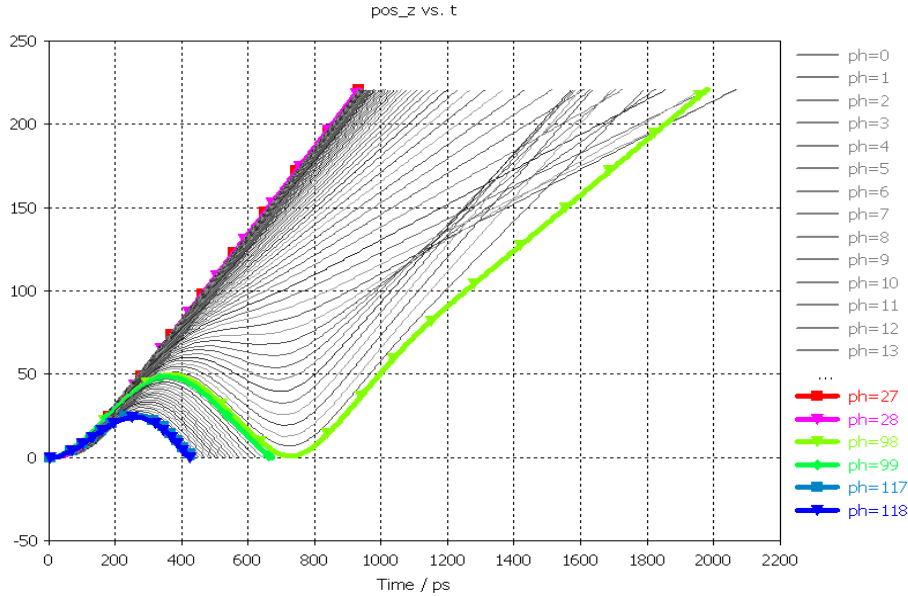


**Figure 3.21 Longitudinal trace of single particles showing the forward and backward streaming in the gun response to the different initial phase.**

The simulation started with electron emission from cathode and ended with electron exiting the gun or hitting the cathode. Fig 3.21 shows that the electrons emitted over the phase range from  $0^\circ$  to  $98^\circ$  can be accelerated out of the gun. And some of them experience an oscillation between forward and backward motion while through the gun. For the electrons emitted over the phase range of  $98$  to  $180$ , they experience less acceleration than deceleration and back bombard to the cathode. These electrons would not only break the Cs-O monolayer of GaAs photocathode but also generate the secondary electrons in the GaAs and damage the cathode. The secondary electrons generation is dependent on the energy of initial back bombardment electrons.

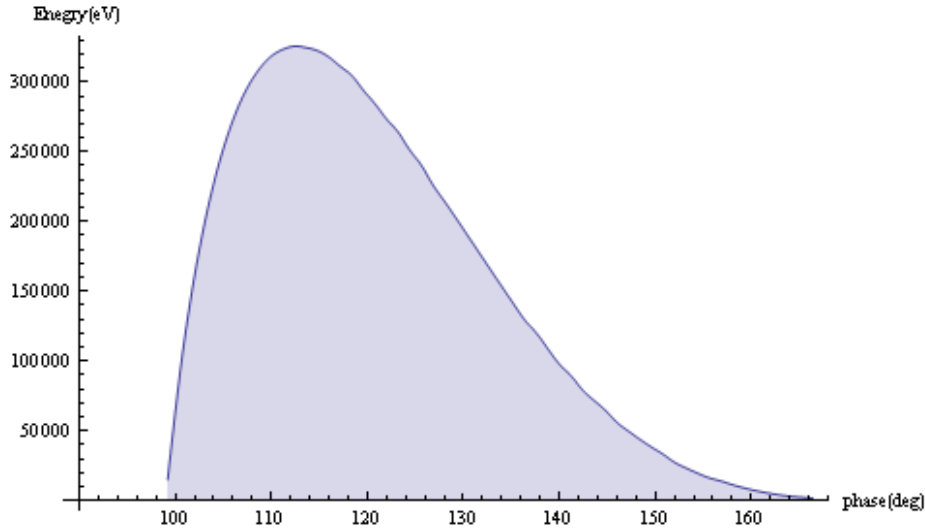


**Figure 3.22 The Energy of back bombardment electron response to the initial RF phase.**

Fig 3.22 shows the phase dependent of back bombardment electron energy when the peak field is 15 MV/m. The maximum energy is 0.33 MeV when the initial phase is  $112^\circ$ . There are two methods to decrease the back bombardment phase of the RF gun. One is increase the storage energy of the gun. When the peak field of the gun increase to 30 MV/m, the electron back bombardment phase range is decrease to  $108^\circ$  to  $180^\circ$ . Another way is change the cavity geometry. Figure 3.30 shows that the initial phase range of back bombardment is  $160^\circ$  to  $180^\circ$  when the peak field is 15 MV/m.

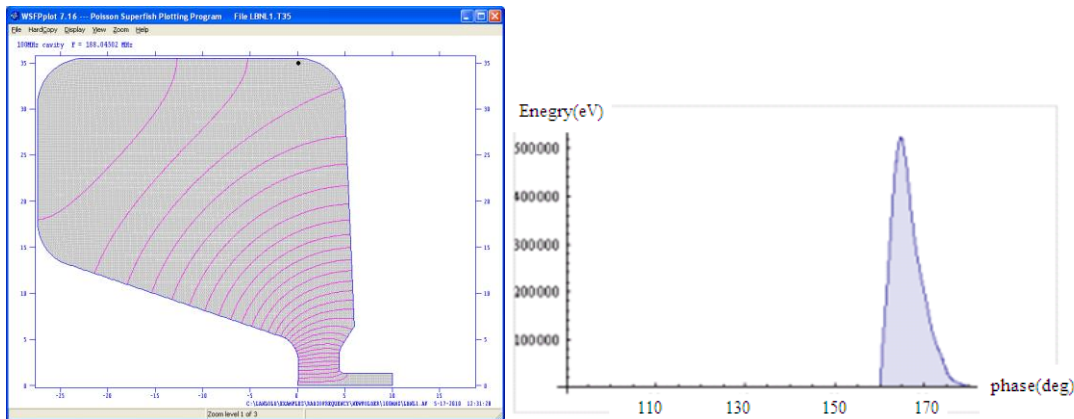


**Figure 3.23 a) The geometry of the LBNL VHF gun [61]; b) The back bombardment phase range.**

### 3.4.2 Multipacting in BNL plug gun

Multipacting on the photocathode is a characteristic phenomenon in RF gun. W. Hartung first obtained the electron multipacting at A0 system at FermiLab in 2001 [62]. J. H. Han studied the secondary electron emission from Cs<sub>2</sub>Te photocathode in a RF gun. He ignored the phase delay between incidence and emergent electron [63]. The film photocathodes such as Cs<sub>2</sub>Te and multi-alkali are not sensitive to the electron back bombardment. However, the NEA photocathode such as GaAs does due to the Cs-O monolayer damaged. For the block GaAs photocathode, the phase delay has to be considered. The secondary electrons generate inside the GaAs drift to the emission surface. If some electrons drop into the back bombardment phase, these back streaming electron would hit into the photocathode and generation the secondary electron again. Figure 3.24 shows the interaction of the back bombardment electrons and the photocathode.

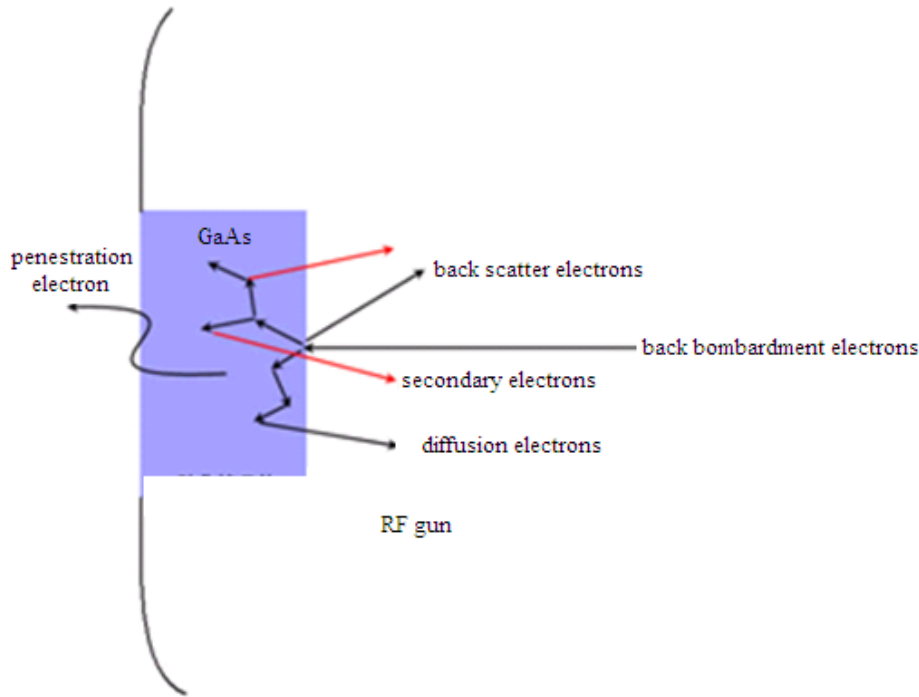


**Figure 3.24 The interaction of back bombardment electrons and photocathode.**

In order to understand the role of secondary emission in this performance, a program was written to simulate the motion of a single electron in the gun and inside the GaAs crystal.

It reads the field files from Superfish program. The initial secondary electron distribution data come from Monte Carlo simulation using CASINO.

To simplify the process of secondary electron generation and motion, the assumptions are listed as follows.

1. The program doesn't consider the number of secondary electrons generation. The program assume the yield is larger than 1.
2. When secondary electron arrives at surface, it can be emitted if it is in accelerating phase. The electrons don't be trapped on the surface due to NEA surface
3. The program only considers the drift motion. The diffusion motion is ignoring. The reason is declared at previous section.

According to this simulation, if the primary electron trajectory is such that it returns back to the GaAs, its trajectory in the GaAs can be divided into three groups: most of the energy deposited close to the surface (Region I), most of the energy deposited in the middle of the GaAs (Region II) and most of the energy deposited near the back surface of the GaAs (Region III). The secondary electrons from Region I see a acceleration RF phase and hence are emitted exit the gun. Figure 3.25a) shows the electrons trajectory for this scenario. The secondary electrons generated in Region III stay within GaAs for more than one RF cycle and hence oscillate back and forth within GaAs and are not emitted either (Figure 25c). However, the secondary electrons generated in Region II can be emitted and can contribute to multipacting. Figure 3.25b describes the electron trajectory for this scenario, as a function of the RF phase and shows emission of the secondary electron from the GaAs. The location of this region within the GaAs is a strong function of the RF phase and the RF field. Figure 3.26 illustrates the location of this Region II (section between the red and blue curves) within GaAs as a function of the RF phase for our 1.3 GHz gun operating at a field gradient of 15 MV/m. Since the laser pulse to be used for these experiments is ~10 ps, irradiating the cathode at the RF phase of 20 degrees to maintain low energy spread, the source for the secondary electrons is primarily the dark current form the cathode, emitted at random phases. Figure 3.26 indicates that at zero phase where the RF field and the dark currents are maximum, the region II lies 10-20 microns below the surface and could contribute to secondary electrons.

The problem about which we still have concern is the number of times that electrons encounter back-bombardment. Figure 3.26 shows the different positions of the secondary electrons' effect for the GaAs cathode. Only in the zone II does electron bounce back twice as in the Figure 3.25b. The second electrons produced at the position of zone III oscillate in the GaAs for hundred nano seconds and then run out of GaAs from the behind, as depicted in Figure 3.25c.

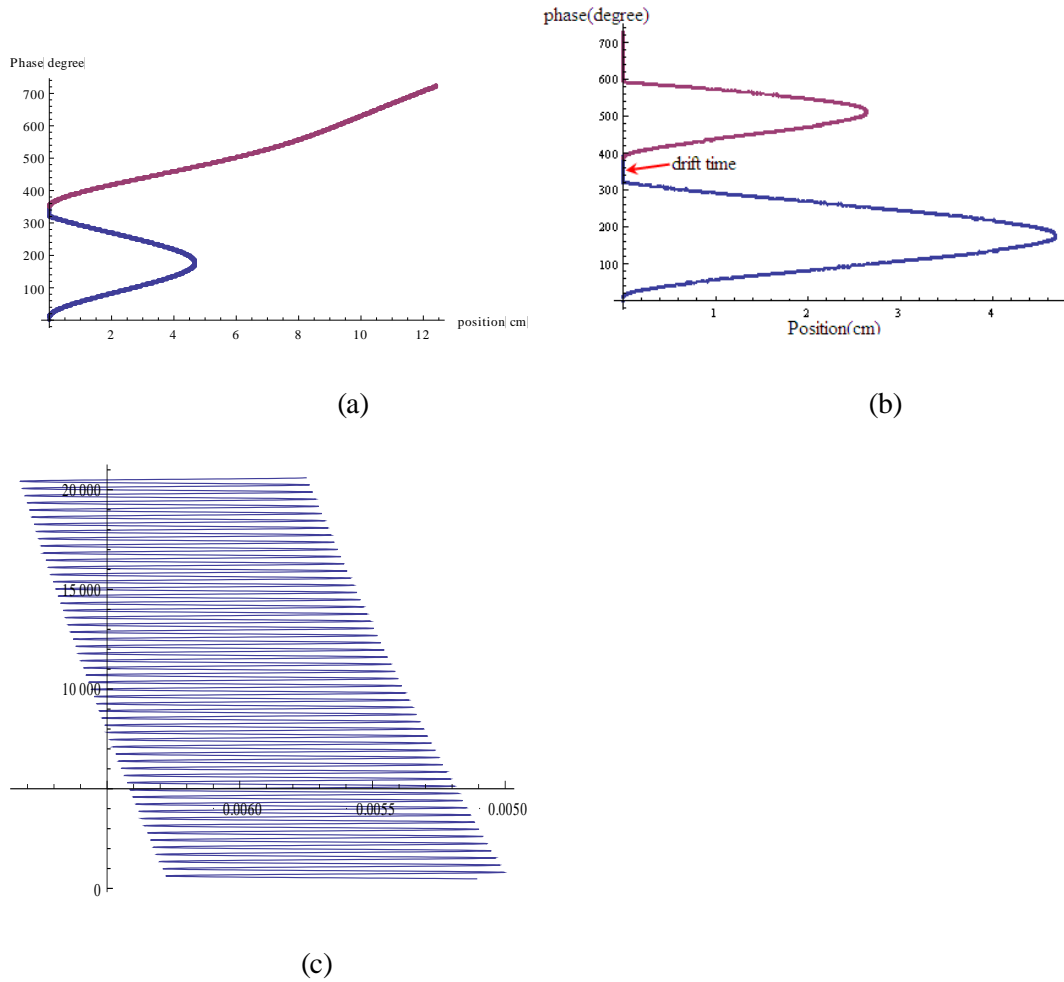


**Figure 3.25 a) The curve depicts the trajectory an electron that has twice moved back to the gun; b) Electrons oscillate in the GaAs.**

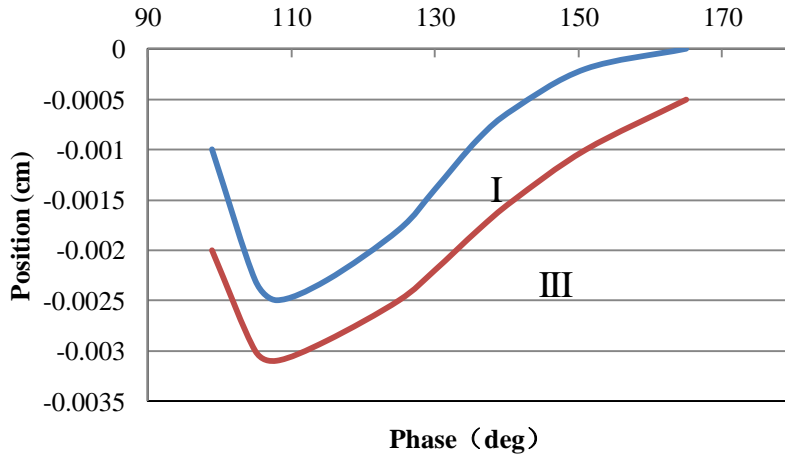


**Figure 3.26 The secondary electron generate zone in GaAs.**

Based on the BINP's experiment and the electron back-bombardment-induced multipacting simulation, it appears that the electron back-bombardment is the main cause of degradation of the GaAs in the RF gun [14]. Judicial choice of the laser pulse with respect to the RF phase is critical to minimize the back bombardment and x-ray generation. The zero RF phase have to be found initially.

In order to achieve this experimentally, we propose the following procedure to find the zero RF phase: When the peak electric field reaches 15 MV/m at the photocathode's emission surface, the simulation shows that those electrons that are emitted from the photocathode in the RF phase between  $98^{\circ}$  to the  $180^{\circ}$  are in the back-bombardment range, and the highest backward-oriented energy is 300 keV. To minimize the number of emission electrons, 1 uW laser power at wavelength of 532 nm is adopted. The 2 nA of average current can be obtained if the QE of photocathode achieve 0.5%. Based on the simulation, the back bombardment electron hit point is offside 50% more than initial emission point offside [64]. So the laser illuminate on the edge of emission surface would lead the backward electron hit outside of the photocathde.

The electron bombardment triggers X-ray radiation from the gun due to bremsstrahlung radiation. A radiation detector mounted at the outside of the dewar close to the gun detects these X-rays when the energy of the electrons back-bombardment is higher than

120 keV. The gun is insulated by a DC block and a ceramic break so that one can measure the electron emission current.

The low-power laser will be used to drive the GaAs photocathode. If electrons are emitted in the phase range between  $0^{\circ}$  to  $98^{\circ}$ , the photocurrent can be measured, but no x rays are generated. If the electron is emitted in the phase range between the  $100^{\circ}$  to the  $180^{\circ}$ , X-rays are detected but the photocurrent does not escape the gun and cannot be measured. For electrons emitted in the phase range between  $180^{\circ}$  and to the  $360^{\circ}$ , there is no photocurrent and no X-rays.

After identifying the initial phase of the laser, the  $0^{\circ}$  critical RF phase can be searched for without staying too long in the back-bombardment phase range.

## Chapter 4 Diamond amplifier fabrication

### 4.1. Diamond amplifier characteristic properties

#### 4.1.1. Diamond properties

Diamond is a transparent crystal of tetrahedrally bonded carbon atoms. Diamond is an allotrope of carbon, where the carbon atoms are arranged in a face centered cubic crystal structure [65]. Figure 4.1 shows the diamond crystal structure [66] and Table 4.1 shows the reference values of diamond.

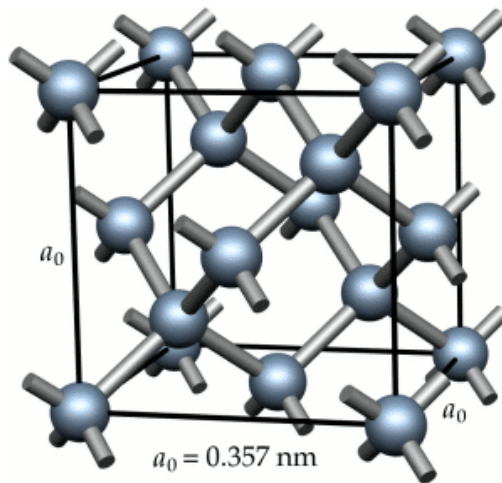
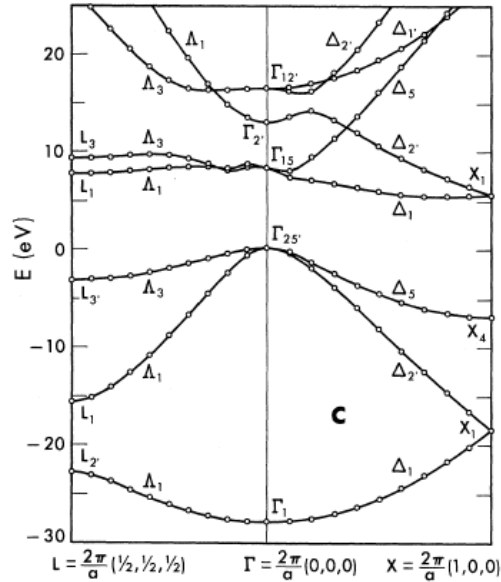


Figure4.1 Diamond crystal structure.

Table 4.1 Reference values of diamond

Density	$3.52 \text{ g/cm}^3$
Lattice constant	$1.54 \text{ \AA}$
Atomic density	$1.76 \times 10^{23} \text{ \AA}^3/\text{m}^3$
Thermal conductivity	$2000 \text{ (W/m.K)}$
Breaking strength	$400\text{-}600 \text{ MPa}$
Breakdown gradient	$4 \text{ MV/cm}$
Electron mobility	$2200 \text{ cm}^2\text{V}^{-1}\text{s}^{-1}$
Hole mobility	$1600 \text{ cm}^2\text{V}^{-1}\text{s}^{-1}$
Electron situated velocity	$27000000 \text{ cms}^{-1}$
Relative permittivity	$5.6$
Resistivity	$10^{13}\text{-}10^{16} \text{ \Omega cm}$

Diamond is an indirect band gap material. Its electron band structure is shown in Figure 4.2 [67]



**Figure 4.2 Diamond electron band structure.**

Figure 4.2 shows the maximum of valence band is at center of Brillouin zone ( $\Gamma_{25'}$ ) and the minimum of conduction band is at  $\Delta_1$  point. The minimum band gap of the diamond is  $\Gamma_{25'} - \Delta_1 = 5.4$  eV. For indirect band gap materials, the electron and hole cannot recombine by losing energy except gaining additional momentum.

The perfect diamond cannot trap charge carriers. However, in general, diamond has defects, which generate states with energy levels in the band gap. When charge carriers move through the diamond lattice, they would be trapped by these defects. The defects in the diamond can be detected by X-ray topography technique. Figure 4.3 shows X-ray topographies of two CVD grown diamond samples. The X-ray topography was carried on X19 beam line of NSLS.

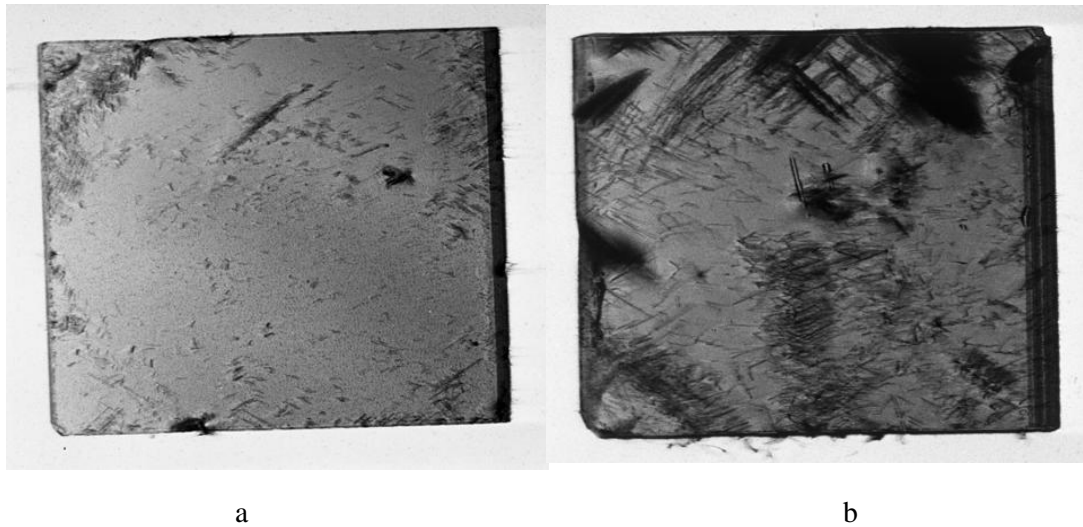


**Figure 4.3 The topographies of 110 face of two CVD diamond samples.**

The dark dots and lines are the defects on 110 face of the single crystal diamonds. The single crystal diamond samples are purchased from Element 6 Corp. This technique shows the bulk quality of the diamonds and provides us the criteria of choosing the diamond samples in advance.

#### 4.1.2. The concept of diamond amplifier

A diamond amplifier photocathode consists of a diamond amplifier and a photocathode. The diamond, functioning as a secondary emitter, amplifies the primary current of a few keV energy electrons that come from a laser-drive photocathode and a DC structure [68]. The surface of one side of the diamond is coated with a metal, like Pt, whilst its other side is hydrogenated to attain a negative electron affinity surface. Primary electrons penetrate the diamond through the metal coating, and excite electron-hole pairs, the number of which typically is about two orders of magnitude more than the number of primary electrons, depending on their energy. Secondary electrons drift across the diamond under the gun's electric field that penetrates the diamond. The holes drift back to the metal side and are absorbed by the ground as the secondary electrons reach the hydrogenated surface and exit into the vacuum through the diamond's negative electron affinity (NEA) surface. Figure 4.4 shows the diamond amplifier in the RF gun. The conversion of primary electrons into secondary electrons wipes out characteristics of primary electrons except for the current, bunch length and bunch size. The low emittance beam can be

generated with thermalization of the secondary electrons and the NEA surface combined with the high RF electric field.

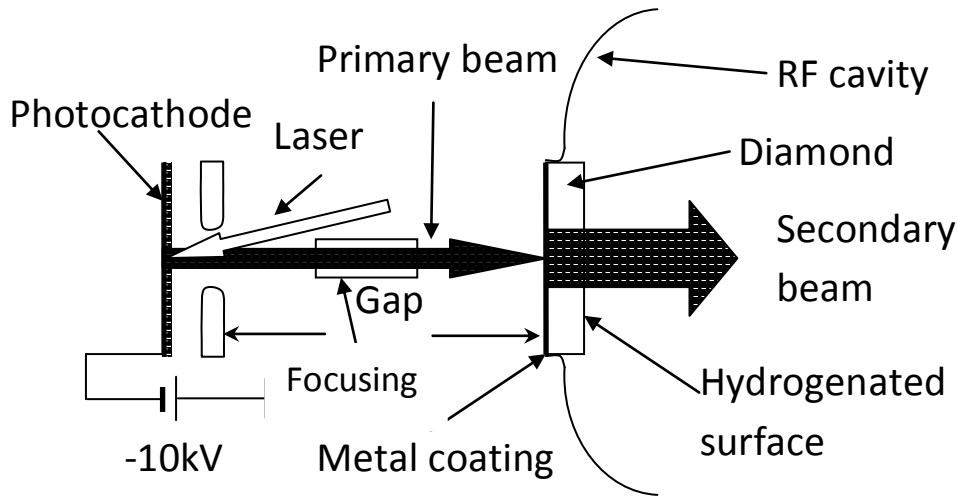


**Figure 4.4 Diamond amplifier in RF gun.**

The advantages of diamond amplifier photocathode are [69]:

1. The average current is not limited by the average power of the drive laser.
2. The diamond window insulated the SRF gun and semiconductor photocathode. The SRF gun thus avoids contamination by the materials coming from the photocathode such as Cs. The photocathode also is protected by the diamond window thus avoiding break by the particle back bombardment.
3. The beam with low emittance and short bunch length can be obtained from diamond amplifier.
4. The lifetime of the diamond amplifier is much longer than of high QE semiconductor photocathodes. The diamond amplifier can be transferred in the atmosphere. The load lock system isn't necessary for this cathode.

In previous transmission mode measurements by Dr. Chang and other scientists, they have found [70-72]:

1. Only synthetic high purity single crystal diamond is suitable for use as diamond amplifier. Natural diamonds and polycrystalline diamonds can trap many electrons in the bulk, which results in shielding of the external field.
2. The diamond can deliver up to an average current density more than  $100 \text{ mA/mm}^2$ . The peak current density greater than  $400 \text{ mA/mm}^2$  was obtained.

3. The gain is independent of the density of primary electrons in the practical range of diamond amplifier applications
4. The electrons deposit 3.3 keV in the 40 nm Ti/Pt metal coating.

The hydrogen termination diamond have NEA surface, however part of the secondary electrons is still trapped on the surface due to surface barrier and defects. These electrons shield the external field and lead the electrons and holes recombination after diffusion to the metal coating. The experiment shows that holes can neutralize the trapped electrons when the opposite voltage is applied. The holes are generated by the primary current hit the diamond in the positive voltage.

## 4.2. Diamond amplifier preparation

### 4.2.1. Metallization

The holes drift to the metal coating, which is in contact with the niobium and grounded. Primary electrons penetrate the metal layer and deposit part of their energy in the metal. The residual energy is contributed to secondary electron generation. The gain of secondary electron is given by

$$G = \frac{E_{primary} - E_{metal}}{E_{e-h}} \quad (0.40)$$

Where  $E_{primary}$  is primary electrons energy and  $E_{metal}$  is the energy deposited in the metal.  $E_{e-h}$  is the energy to generate one electron-hole pair.

The metal selection has to consider a good contact between the diamond and metal. Meanwhile, such contact must allow the holes to easily escape from the diamond. Based on metal selection, 30 nm platinum coating is adopted. The EMITECH K575X sputter is used for metal coating. Figure 4.5 shows a photo of diamond after metal coating.

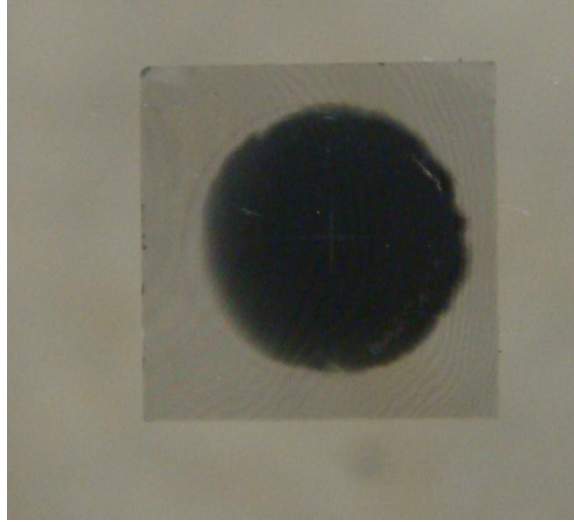


**Figure 4.5 The diamond sample after metal coating.**

#### 4.2.2. Hydrogenation

Hydrogenation is the process of applying hydrogen termination to the diamond amplifier emission surface [73]. The high-quality hydrogenation is one of the most important steps in diamond amplifier fabrication. This process determines the electron trapping probability on the surface and the gain of the diamond amplifier. There are two methods to terminate the hydrogen on the diamond. One is plasma hydrogenation, which is done under hydrogen plasma environment. Another is by hydrogen atom generated by gas cracker. When pure hydrogen is flowing through a thermal gas cracker (MANTIS MGC75), more than 90% of hydrogen molecules will be cracked into atoms [74]. We adopted the second way to hydrogenate the diamond. The hydrogenation experiments were carried out in a bakeable UHV chamber evacuated to  $1.7 \times 10^{-9}$  hPa by a turbo pump and an ion pump. The chamber was equipped with a residual gas-analyzer and a hydrogen-cracker. The diamond, biased to -50 V, was placed on a button heater to heat it to 800 °C. A thermocouple, in thermal contact with the sample's base monitored the temperature. The diamond was illuminated directly with a deuterium lamp that has a continuous emission spectrum between 190 and 300 nm. Figure 4.6 is a sketch drawing of the hydrogenation system.

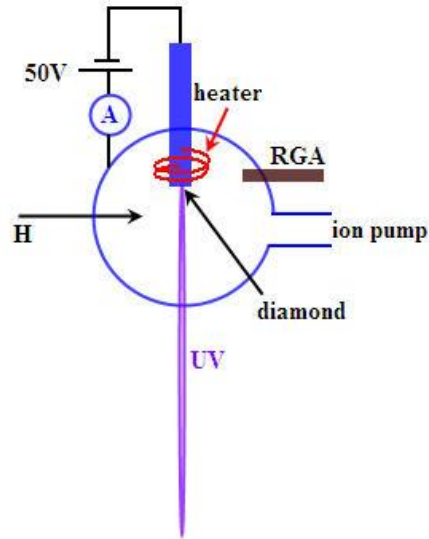


**Figure 4.6 The schematic plot of the hydrogenation system.**

The sample is stacked up as shown in Figure 4.7 at the center of the button heater. The sapphire mask with a 3 mm hole covers the diamond, which is in contact with the heater button. The surface to be hydrogen terminated cannot contact with any metal during handling.

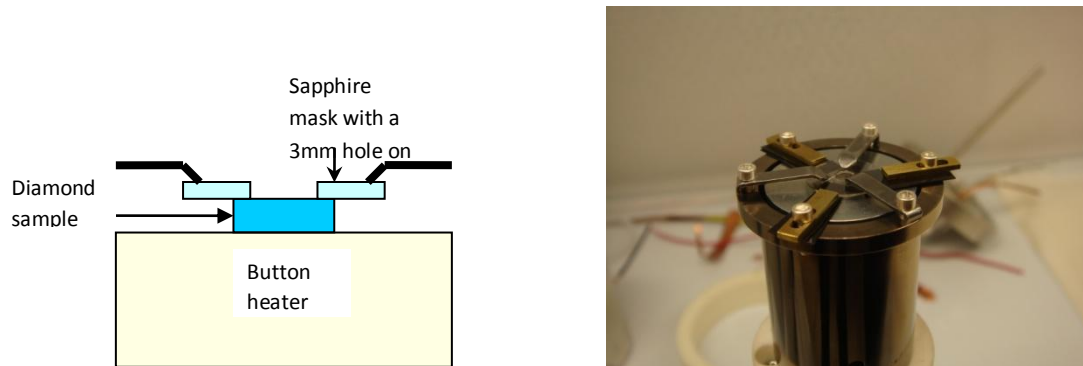


**Figure 4.7 Schematic plot of stacking the diamond sample on the button heater and photo of the assembled sample with auxiliaries.**

The steps in fabricating diamond amplifiers were:

1. The diamond sample was cleaned ultrasonically in acetone and then in 100% alcohol for 15 minutes.
2. 35 nm Pt was sputtered onto one side of the diamond wafer.
3. The diamond was heated to 800°C to clean its surface.

4. A UV light was shone on the prospective hydrogenated surface, and the photo current was measured.
5. The sample was exposed to a flow of hydrogen atoms generated by a commercial hydrogen cracker. The hydrogen pressure is higher than  $3 \times 10^{-7}$  torr read by RGA.
6. After the photocurrent reached its peak, the source of hydrogen atoms was turned off.
7. Fabrication of the diamond amplifier was complete after its temperature had dropped to room temperature.
8. The total yield was measured.

The hydrogenation process takes 40 minutes. The diamond amplifier can be exposed to the atmosphere.

### 4.3. Optimized hydrogenation procedure

#### 4.3.1. Spectral response of hydrogenated diamond

One important parameter of the hydrogenated diamond is its photoemission QE that is an indicator of the negative affinity of its surface. The band gap of diamond is 5.447 eV corresponding to 226.7 nm drive wavelength. The lamp (NAEWPORT Corp. 7340) was coupled to the UV monochromator (Oriel Cornerstone 260 1/4), enabling us to acquire the spectral dependence of photoemission in the same spectral range. Figure 4.8 shows the lamp spectrum after the monochromator. The strongest power is at 230 nm wavelength. The diameter of the UV light's spot was 3 mm, covering the entire hydrogenated surface of the diamond.

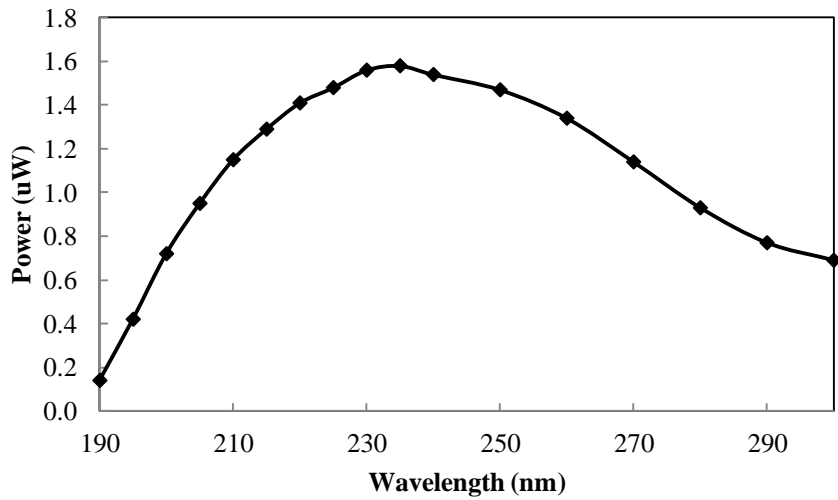


**Figure 4.8 The lamp spectrum after the monochromator.**

After two hours preheating, the output power of lamp is stable. Fig .4.9 shows the power fluctuation of 220 nm wavelength light in three hours.

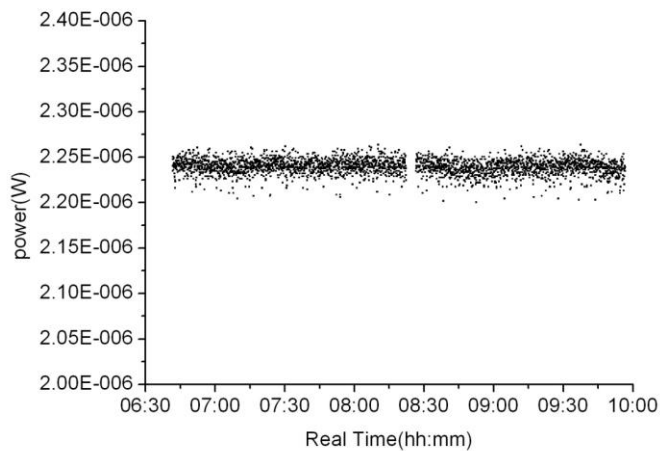


**Figure 4.9 The power fluctuation of 220 nm wavelength light in three hours after two hours preheating.**

The electrons excite to the conduction band and diffuse to the emission surface. These electrons easily emit out when the NEA surface is formed. Figure 4.10 compares the spectrum of hydrogen terminated diamond and normal diamond. QE of hydrogenated

diamond is two orders higher than before hydrogenation. That means the hydrogenation process is successful.

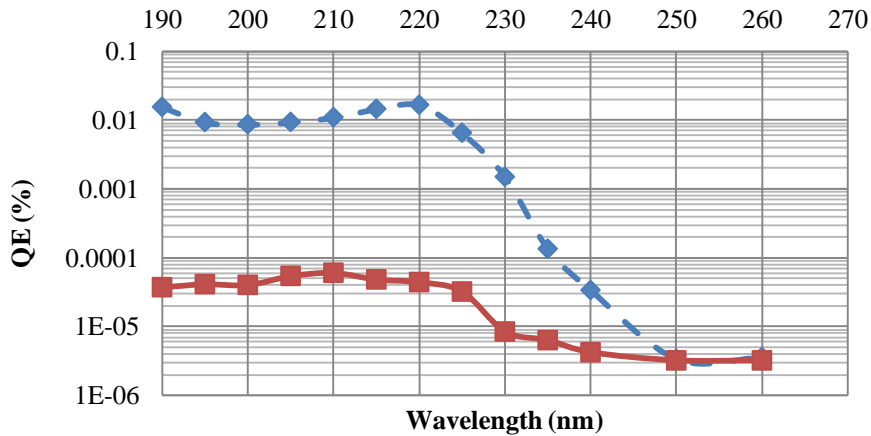


**Figure 4.10 Comparison of the emission spectrum of diamond with hydrogenation and without hydrogenation. The solid line represents the emission spectrum of diamond after 800 °C bake and the dash line represents the emission spectrum of hydrogenated diamond.**

#### 4.3.2. Hydrogen cracker power

The power of cracker determines hydrogenation speed. The crack rate is not high enough to hydrogenate the diamond when the power is less than 30 W. The tungsten tube was soft when the power is higher than 60 W. Our experience shows the cracker power between 30 W to 60 W should be used for hydrogenation. The hydrogenation takes 40 minutes when 50 W of crack power is chosen.

#### 4.3.3. Surface cleaning

The purpose of surface cleaning before hydrogenation is to eliminate the contamination such as oil stuck to the diamond in handling and transferring. These contaminations eliminate the diamond emission capability. We found that acetone and alcohol cleaning of the diamond in ultrasonic bath for 15 minutes can make the diamond surface clean.

For the diamond already metal coated, mechanical polishing is used for getting rid of the coating. Mechanical polishing is done at DDK Corp. Aqua regia is usually used for etching off the Pt coating, but does not clean it away completely. The emission spectrum shows that the hydrogenated diamond have a long wavelength response if it etched by Aqua regia, compared with mechanical polishing diamond (Figure 4.11).

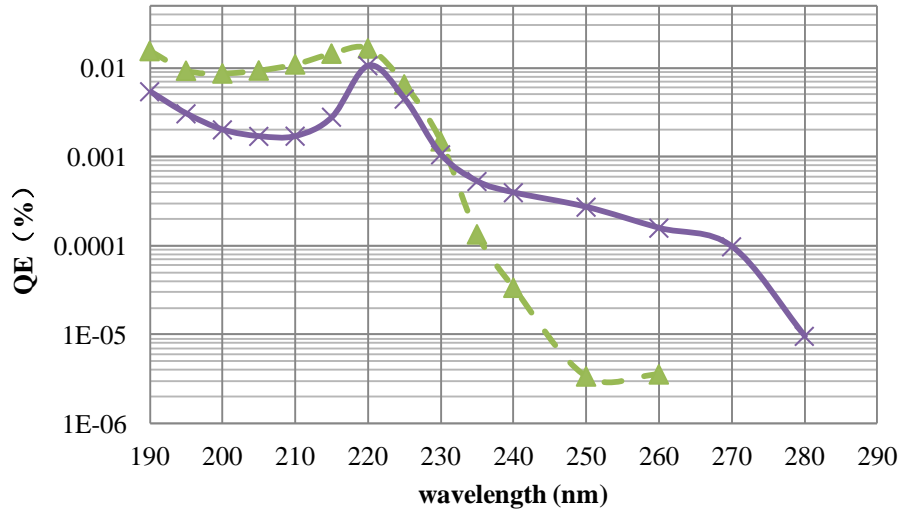


**Figure 4.11 The comparison of emission spectrum of diamond etched by Aqua regia (solid line) and diamond mechanical polished (dashed line).**

The Aqua regia etched diamond has good total yield, but fails to emit secondary electron. The long wavelength response may be caused by the platinum photoemission. In total yield process, the electrons diffuse to the emission surface. Even if the surface is contaminated by metal, the electrons still can emit if these electrons don't meet metal. However, for secondary electron emission, the electrons drift to the surface by applied high voltage. So these electrons will drift to the residual metal and become trapped on the surface. In our later diamond amplifier fabrication, we use mechanical polishing to get rid of platinum.

#### 4.3.4. High temperature hydrogenation

We compared four diamonds hydrogenated at room temperature with four others treated at high temperatures. For the latter, after temperature of the diamond reached 800 °C, the heater was turned off; hydrogenation was started, and continued as the sample's temperature decreased gradually to 320 °C. For room-temperature hydrogenation, the sample was allowed to cool down to 23 °C before starting hydrogenation. For both, we set the power of the hydrogen cracker at 50 W, and the hydrogen partial pressure was  $1.3 \times 10^{-6}$  hPa. The electron yield was monitored while the 220 nm, 2.25 uW UV ray was shone on the diamond.

Figure 4.12 shows a typical curve for photocurrent yield from the hydrogenated surface of sample treated at 800 °C (dark curve) and at 23 °C (gray curve).

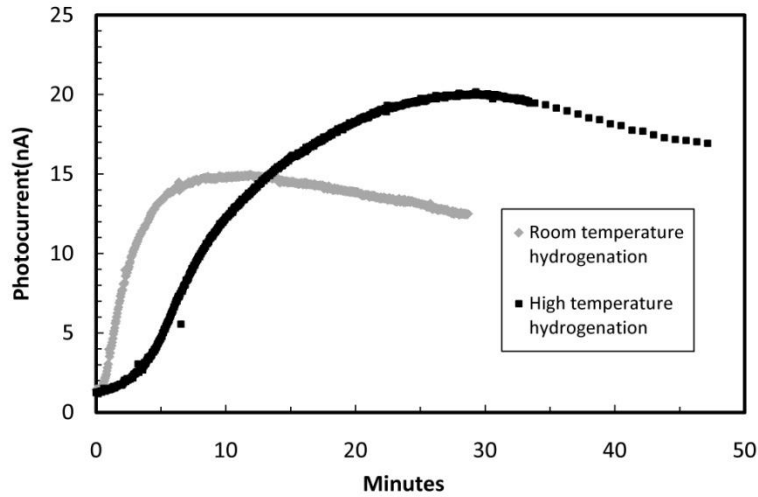


**Figure 4.12** The trend in the photocurrent during the hydrogenation process. Dark curve represents the trend during high-temperature hydrogenation, and the gray curve is that at room temperature.

As Figure 4.12 shows, the photocurrent took 30 minutes to reach a peak when the diamond was hydrogenated at high temperature; in contrast, during hydrogenation at 23 °C, the photocurrent peaked in 10 minutes. The hydrogenation process started immediately. The speed of hydrogen deposition differed at these two different temperatures. At high temperatures, hydrogen attaches to and detaches from the carbon atoms. Hence, it takes longer to reach optimum coverage than when the process is carried out at room temperature at which the detachment of hydrogen is insignificant. Further hydrogenation does not increase the coverage. However, it exposes the sample to contaminants released from the cracker that may cause impinge on the diamond’s NEA surface causing the photo current to decay. This reduction was unrecoverable by subsequent re-baking or re-hydrogenation. Figure 4.13 shows the QE decays of the high-temperature and room-temperature hydrogenation process. At the end of hydrogenation (after the cracker was turned off and the hydrogen pumped from the system), the change in QE over time was measured with 220 nm light. In 11 hours, the QE of the diamond processed at high temperature dropped 13%, while that of the diamond treated at room temperature declined 50%; thus, the NEA surface produced via high-temperature

hydrogenation is more stable than that created at room temperature. The high-temperature hydrogenation decay curve is best fit to the function  $12.68 + 2.787e^{-0.21*t}$ , while the best fit for the decay after room-temperature hydrogenation is a twin decay function,  $4.98 + 2.87e^{-0.21*t} + 2.211e^{-4.0*t}$ . Therefore, the decay curve of the latter has two components, one with a decay time of 0.25 hours, and a slow component where the decay time (~4.76 hours) is common to both processes curves. Such loss of QE can be recovered by baking the sample. Thus, after the decay of the QE in 11 hours, we baked the diamonds at 400 °C for 30 minutes. There was almost full recovery (99%) of the QE of the diamond that underwent high-temperature hydrogenation; the decay of the photocurrent under this condition is due to contaminants, such as water absorbed on the hydrogenated surface that are desorbed to the surface during baking [75]. However, the QE of the diamond hydrogenated at the room temperature exhibited only 65% recovery after baking, implying that baking can correct the slow decay, but not that lost during the fast decay.

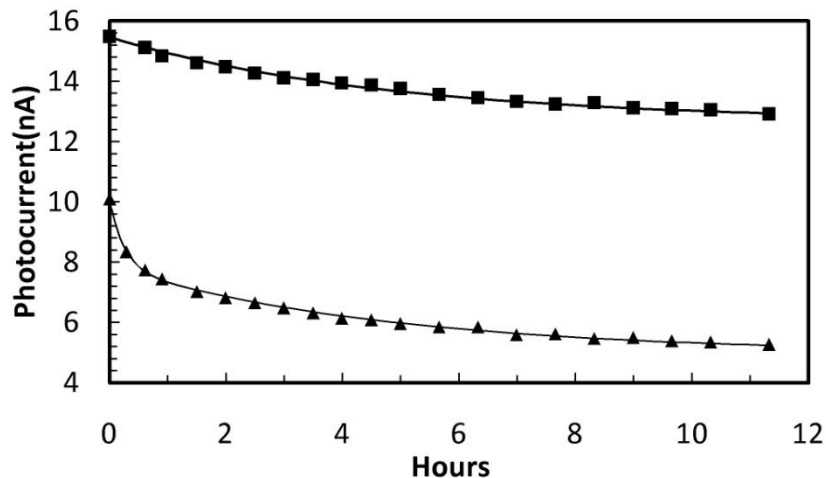


**Figure 4.13 The stabilization of the photocurrent of hydrogenated diamonds in 11 hours. The solid squares are for the photocurrent of the high-temperature-treated diamond; the solid triangles are for the photocurrent of hydrogenation decay at room temperature. The thin black curves are the best fit functions.**

#### 4.3.5. Lifetime measurement

Several factors might cause the QE decay of the hydrogenated diamond including interactions between the UV beam, residual gas, and the diamond surface, or the

contamination of the diamond's surface by residual gas. Surfaces contaminated by the back bombardment of the ions generated by the UV light decompose the residual gas, as similarly, does the back-bombardment of ions generated by photoemission electron ionization. Identifying the causes of photocurrent decay undoubtedly would improve the hydrogenation process. The power of the UV light was 2.25 uW at 220 nm, and the diamond was biased at -50 V. In this experiment, the base pressure of the high vacuum chamber was  $2 \times 10^{-9}$  hPa. Figure 4.14 shows the photocurrent decay under different conditions. During every cycle of the measurement, we first heated the diamond sample to 800 °C for 30 minutes to obtain a bare surface before following the high-temperature hydrogenation procedure. The decay in photoemission was measured under various conditions. The total decline of QE in 15 hours is 18%. We assumed, for simplicity that in the following the processes were additive. Then, we summed the effects and derived values for them individually to explain which contributed to causing a decay of 13.8%:

- a) When the UV light and the bias voltage were off; the residual gas contaminated the hydrogenation surface. Over 15 hours, the photocurrent dropped by 1.9%.
- b) When the UV light was on and there was no bias voltage, the residual gas and the UV light together affected the hydrogenated surface. In 15 hours, the photocurrent fell by 11.7%. After subtracting the decay due to residual gas described in (a) above, the photocurrent decrease due to the UV light was 9.8%.
- c) When the UV light was off and the bias voltage was on, the positive ions in the chamber were back- bombarded and impinged on this surface, and the residual gas contaminated it simultaneously so that in 15 hours, the QE dropped by 2.6%. After removing the decay due to residual gas as in (a) above, the photocurrent decayed by 0.7% due to the bias voltage.
- d) To study the effect of the UV light on the residual gas and its impact on the QE, the UV light was shifted to irradiate the holder and not the diamond surface, keeping the bias voltage on. Then the residual gas would be still ionized by UV, and the ions would bombard the diamond's surface. This process lowered the QE by 4%. After subtracting the decays described in (a) and (c) above, we conclude that the photocurrent fell by 1.4% due to the ions generated by the UV light, so leading to back bombardment.

Assuming that these reductions are additive, and taking into account the overlapping processes, and then the three processes detailed above explain a decay of 13.8%. The reason of the additional 4.2% decline in 15 hours was unknown.

To identify this yet unexplained reduction, we changed the background vacuum to  $3.8 \times 10^{-9}$  hPa; then, this unidentified part of the decay increased to 7.2%, and depends on the background vacuum. Therefore, this part of the decay in the photocurrent decay may reflect the back-bombardment of ions generated by the ionization of photoemitted electrons. If these different factors independently cause the decay of the diamond's QE, then we can identify the factors affecting its photocurrent decay (table 4.2).

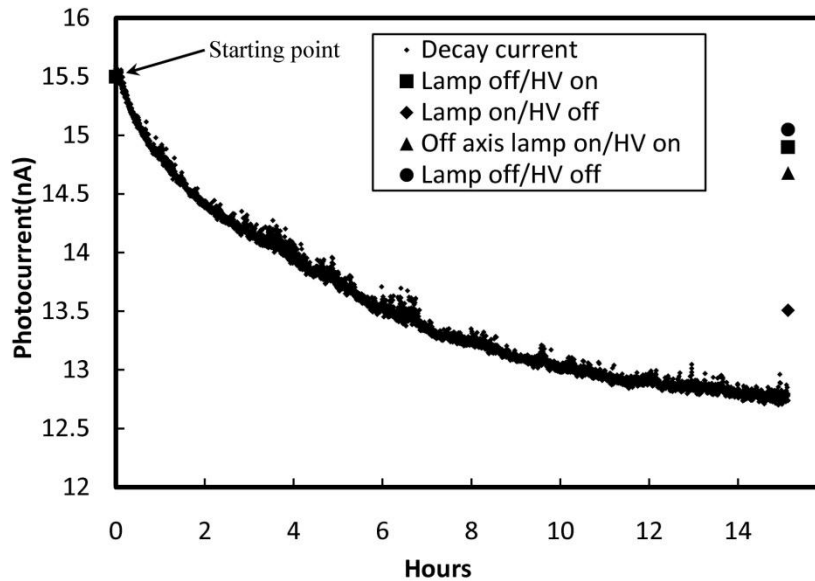


**Figure 4.14** The stabilization of the photocurrent measured in the diamond sample under different conditions.

**Table 4.2** Different causes of photocurrent decay

Decay factor	Decay rate of photocurrent (%)
Residual gas	1.9
UV light, no bias	9.8
UV light ionized gas back bombardment	1.4
Bias voltage	0.7
Probable emission electron ionization residual gas ion back bombardment	4.2

#### 4.3.6. Heat treatment

The diamond amplifier is extremely robust and is stable during exposure to air; the water vapor in the air inhibits electron emission from it. Heating diamonds exposed to the atmosphere removes water molecules from their surfaces. We explored the optimal temperature for such evaporation; the photocurrent of the diamond amplifier with a new hydrogenation surface is 17 nA. After exposure to air for 1 hour, the emission current falls to 2 nA. We then heated the diamond to the 200 °C for 30 minutes and left it to cool. Our measurement of the photocurrent shows the diamond's photocurrent rebounded to 10 nA. QE was scanned as a function of the temperature of the heat treatment: Figure 4.15 shows that the optimized temperature for heat treatment is 450 °C, after which the photocurrent recovered to 96% of that of an amplifier unexposed to the atmosphere. The findings prove that quality of hydrogenation is recovered by baking. Temperatures higher than 450 °C break the hydrogen- and carbon-bonds. At 800 °C, hydrogen atoms are removed from the diamond surfaces, leaving it bare.

After the diamond amplifier QE decayed, re-hydrogenation can be used to recover the QE. Following the hydrogenation standard operation procedure, re-hydrogenation can recover QE to 99% compare to the first time hydrogenation. 97% of first QE can be achieved after six times of re-hydrogenation. So the diamond amplifier can be re-hydrogenation without removal of metal coating after the QE decay.

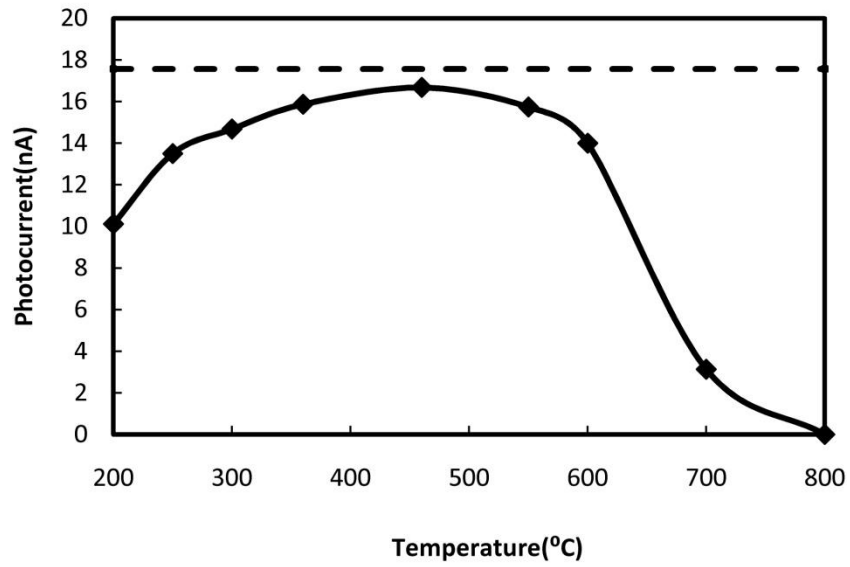


**Figure 4.15** Temperature scanning for optimizing heat treatment of the diamond. The dashed line is the photocurrent of a freshly hydrogenated diamond. The solid curve is the photocurrent after heating the sample to the temperature indicated and allowing it to cool down.

## Chapter 5. Emission mode measurement of diamond amplifier

### 5.1. Measurement setup

The emission mode measurements are designed to study the emission gain of the diamond. The measurement setup including a primary electron source, diamond holder with anode, HV push-pull circuits, drift tube for focusing, phosphor screen and a CCD. Figure 5.1 is a scheme of the emission mode measurements. All the measurement operates in the ultra high vacuum. One ion pump and one NEG maintain the vacuum of this chamber to  $2 \times 10^{-10}$  torr.

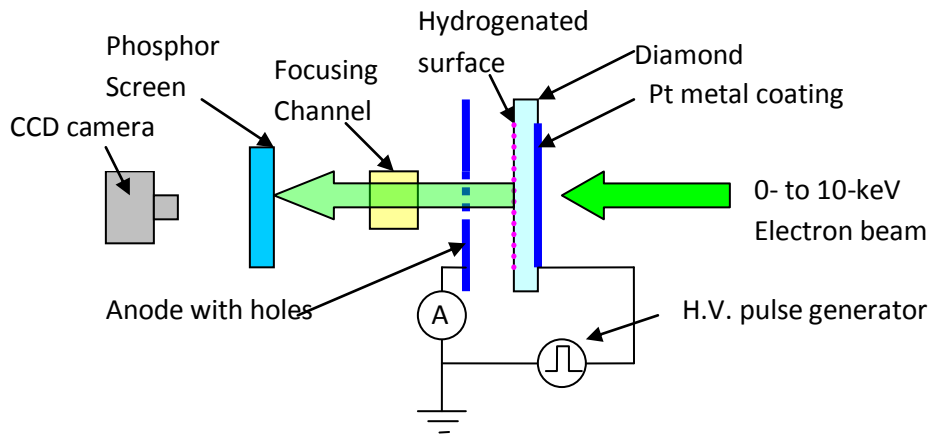


**Figure 5.1 Emission measurement diagram**

#### 5.1.1. Primary electron beam

The primary electrons are generated from a thermionic electron gun (EGG-3101). The cathode material is  $\text{LaB}_6$  with current from 1 nA to 10  $\mu\text{A}$ . The minimum spot size is 60  $\mu\text{m}$  with optimum working distance. The gun has up to 10 keV output electron energy. The gun provides DC beam and the pulse beam with pulsed blanking option, which is triggered by electric circuit. The minimum pulse length is 1  $\mu\text{s}$  [76].



**Figure 5.2 EGG-3101 thermionic electron gun from Kimball physics**

### 5.1.2. Diamond holder

The diamond holder is designed for supporting the diamond surface perpendicular to the primary beam and applies a high voltage to diamond metal coating. The stainless steel tube is pressed on the metal coating side and connected to a high voltage push pull circuits. There is a gap of about  $270\ \mu\text{m}$  between the hydrogenation surface of diamond and the anode. The anode has single hole, which is  $100\ \mu\text{m}$  in diameter on a  $1\ \text{mm}^2$  area at its center. The anode is grounded. A ceramic or sapphire washer and ceramic spacer insulate the diamond and anode. The diamond holder can be heated to  $350\ \text{C}$  by a heater from heating tube for surface cleaning. Figure 5.3 shows the drawing of the diamond holder.

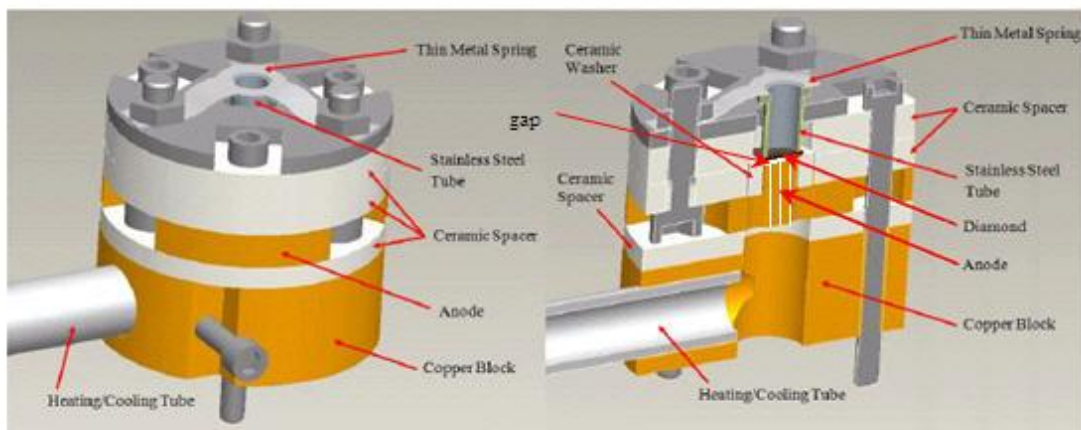


### Figure 5.3 Drawing of the diamond holder

#### 5.1.3. HV push-pull switch circuit

The negative HV pulse on the diamond is provided by a HV push-pull switch (MOSFEL HTS-201-03-GSM) with a rise and fall time of 20 ns. The HV's pulse width, amplitude and its repetition frequency were accurately controlled. The pulse structure is controlled by a 5 V signal from the function generator (FG 5010 TEKTRONIX) [77]. The minimum pulse length can provide by the circuit is 200 ns. A homemade low pass filter is connected to the diamond to block high frequency vibration when the voltage rises up.

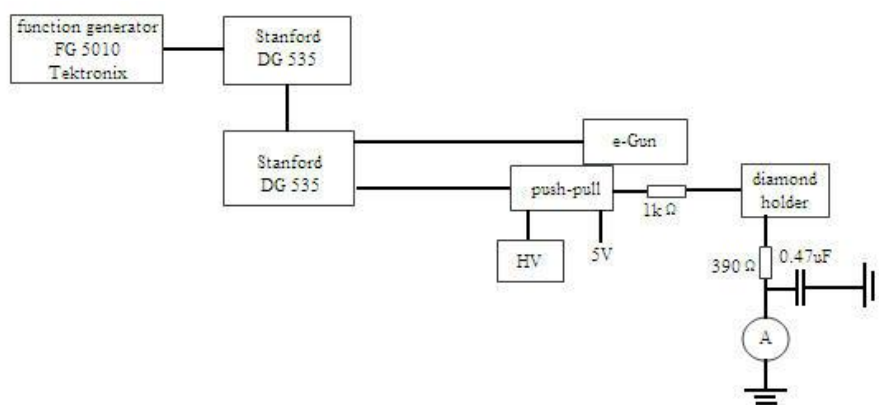


Figure 5.4 The sketch of the HV circuits

## 5.2. Secondary electron beam emission

### 5.2.1. Short pulse measurement

In previous emission measurement, the emission gain was very poor when applied a DC field between the anode and the diamond's metal coating [73]. One DC shielding mechanism was proposed to explain the poor emission in these measurements [78]. A lot of dangling bonds and impurities inevitably remain on the hydrogenation surface due to not perfect hydrogen termination. The secondary electrons or excess charge builds up over time on the surface and shields the external field. This process continues until the field is completely shielded. As calculated, 0.1% coverage of trap centers is enough to shield an external field which is a few hundred MV/m [79]. Previous experiment proved this idea and a pulsed HV was applied on the diamond [79]. When the voltage is pulsed, a field builds up inside the diamond and secondary electrons are generated and move to the

emission surface after primary current is on. The part of secondary electrons trapping on the emission surface takes place immediately when secondary electrons arrive at the hydrogenation surface. Figure 5.5 shows the electron trapping mechanism on the surface. The surface band bending is the main reason for trapping these electrons. When the applied field is turned off, these trapped electron recombine with the holes due to their self-induced field. Then, the trapped diamond returns to its original state and will emit when the next HV pulse comes.

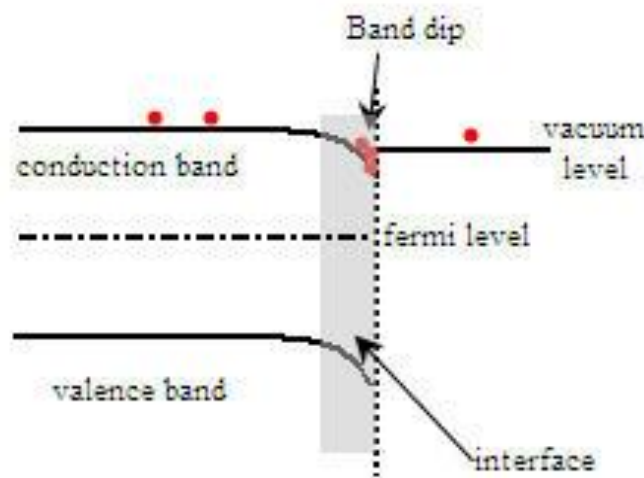


**Figure 5.5 Secondary electrons trapping near the emission surface**

A single-crystal synthetic diamond was metal coated and hydrogen terminated following the SOP described in the last chapter. Good total yield was achieved from the hydrogenation system. The hydrogenation chamber and emission mode gain test chamber are separate. Transferring the hydrogenated diamond exposes it to the ambient air for 20 minutes, during which the surface absorbs water molecules. The whole system baked to 200 °C and  $1 \times 10^{-10}$  torr vacuum was achieved. The thermionic gun was pre-heated for 3 hours to make the current stable. The diamond was heated up to 350 °C to clean the surface contaminations for 30 minutes. A 10 keV primary electron beam strikes the diamond on the central of metal coating side. The negative high voltage pulses are applied to the diamond's metal coating. The high voltage, pulse width and duty cycle can be accurately controlled. The unfocused secondary electrons were emitted out and the image caught by the phosphor screen is shown on Figure 5.6.

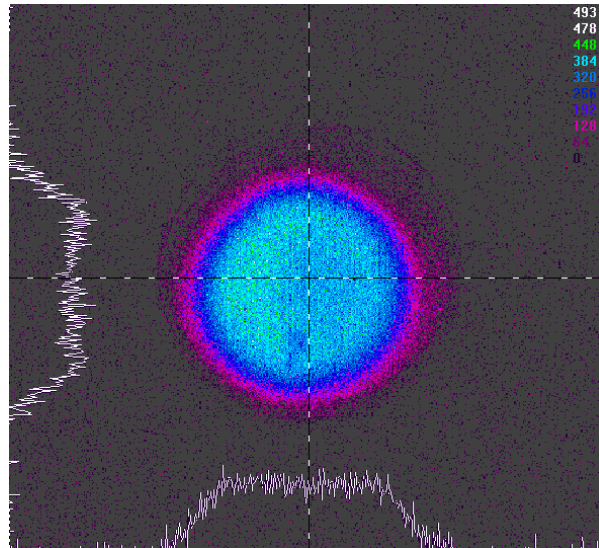


**Figure 5.6 The secondary current image on phosphor screen**

The parameters used on this measurement are listed as follows: repetition frequency is 1000 Hz, high voltage is 3000 V, pulse width is 10  $\mu$ s and the primary current is 329 nA. 169 nA of the secondary current was obtained. To obtain focused beam, the current density was reduced and a 3400 V electric focusing was applied on.

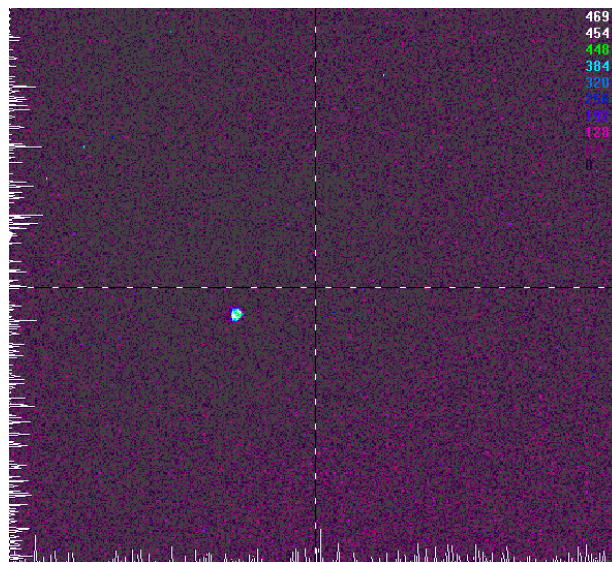


**Figure 5.7 The focused secondary current image on phosphor screen**

Figure 5.7 shows the beam image after electric focusing. The spot is the image of 100  $\mu$ m hole on the anode. The diameter of the spot is smaller than 0.4  $\mu$ m.

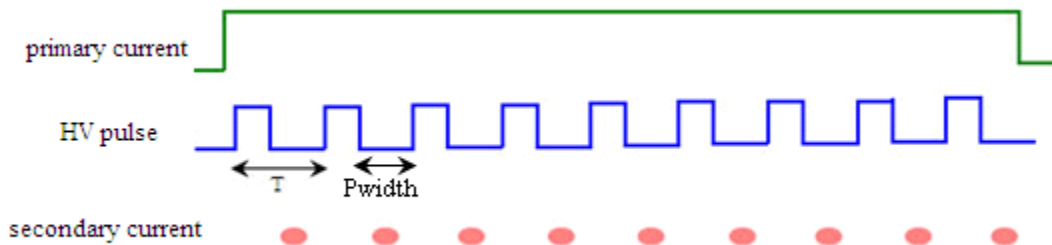
The gain of the diamond amplifier is defined as

$$G = \frac{I_e}{I_p} \quad (5.1)$$

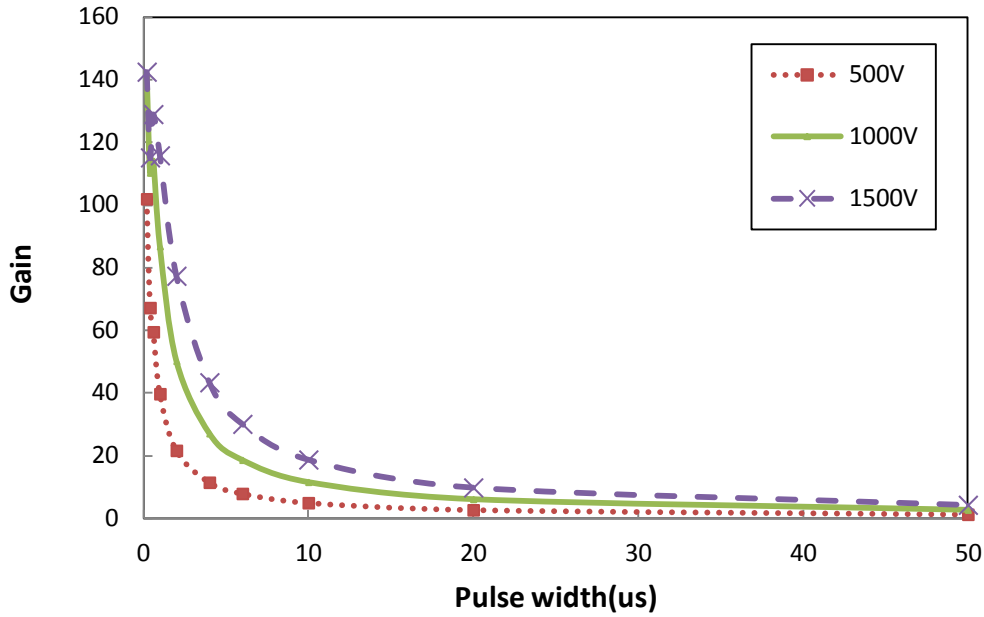
Where  $I_e$  is the instantaneous current emitted from the diamond and  $I_p$  is the DC current. In the experiment, we measured the average emission current by measuring the integrated anode current. The current collect by the anode also includes the leakage current ( $I_l$ ) and induction current ( $I_c$ ). The leakage current was measured when the primary current was on but no HV pulse and the induction current was measured when the primary current is off but the HV pulse is applied. Then the average gain of the primary electrons during the emission period is

$$G = \frac{(I_e - I_c - I_l)}{I_p} \times \left(\frac{T}{W}\right) \quad (5.2)$$

where  $T$  is the period of cycle and  $W$  is pulse width. In a very short high-voltage pulse width ( $\ll \mu\text{s}$ ), when the density of the surface-trapped electrons is insufficient to shield the external field, the average gain of the diamond is equal to instantaneous gain of the diamond. Fig 5.8 shows the secondary beam and pulse structure in emission mode measurement.

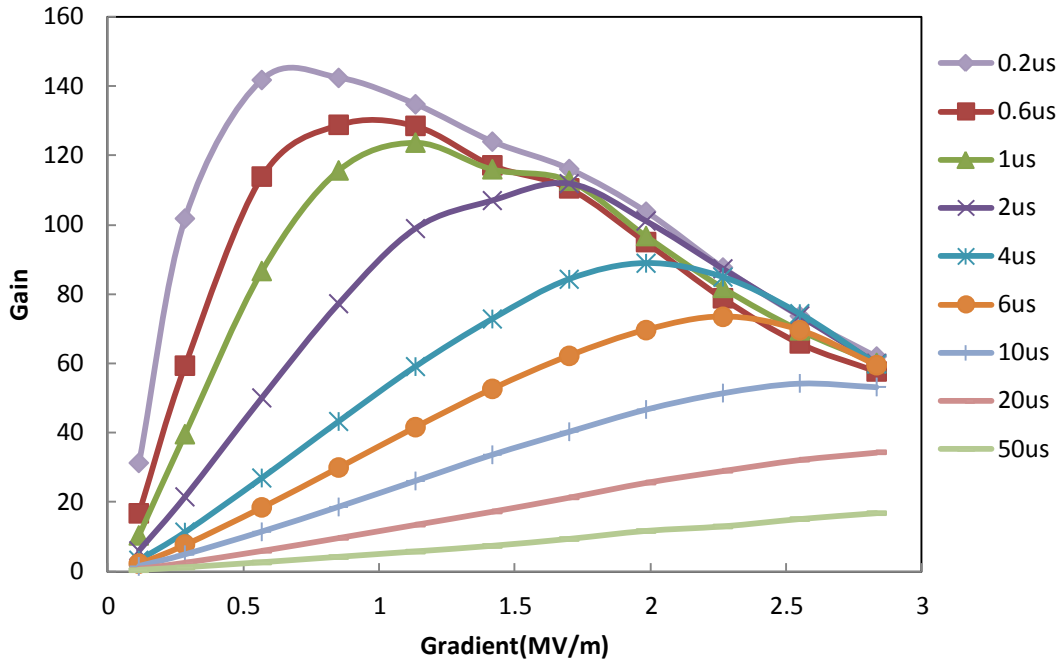


**Figure 5.8** The structure of primary current, HV pulse and secondary current



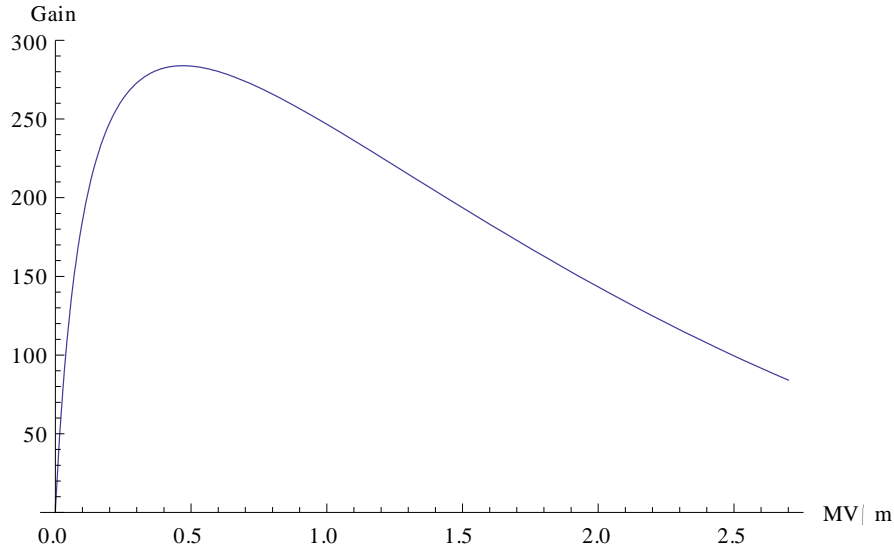
**Figure 5.9 The gain of the diamond vs pulse width.**

Figure 5.9 shows the average gain as a function of pulse width at voltage on the diamond of 500 V, 1000 V, and 1500 V during the pulses. The maximum gain was about 140 at a high-voltage pulse-width of 200 ns under a field of 1500 V. Each curve in Figure 5.9 shows a decrease at long pulse width. It is due to a reduction in the field gradient at end of the HV pulse caused by the trapping of the secondary electrons on H-surface. These trapped electrons were self-neutralized between the HV pulses.



**Figure 5.10 The average gain as a function of gradient inside the diamond**

The gain increase is due to the gradient increase until the saturation gain is reached. Then the saturation gain at short pulse is decreased with increasing field gradient due to the reduction of primary electron's energy. In the setup, the anode and phosphor screen is at ground potential, electron beam is 10 keV and the voltage on the diamond is various. So the primary electrons' energy will reduce when the voltage on the diamond increase. The maximum gain of 140 in this measurement is not the limitation of the diamond gain. It can be increased easily by increasing the primary electron's energy. In the transmission mode measurement, the maximum gain up to 270 was achieved. That means part of electrons is trapped on the surface. With the transmission mode measurement data, the gain as the function of gradient can be plotted as Figure 5.11 when no electrons are trapped on the surface.



**Figure 5.11 The average gain as a function of gradient inside the diamond without surface electron trapping.**

#### 5.2.2. Robustness of diamond amplifier

The semiconductor high QE photocathodes need load lock system to transfer it from preparation chamber to the gun. The C-H bond is very robust. One of advantages of the diamond amplifier is that it can be transferred in the atmosphere without emission decline. In our experiment, the hydrogenation chamber and emission-mode gain test chamber are separate. During transfer from the hydrogenation chamber to the test chamber, the freshly hydrogenated sample is exposed to ambient air for 30 minutes, during which the surface absorbs water molecules. The gain was measured at the center of the diamond amplifier after a 350°C heating/cooling cycle. Then it was exposed the amplifier to dry N<sub>2</sub> and to air at 1.01\*10<sup>4</sup> hPa for 30 minutes. Following another 350°C heating and cooling cycle, we noted that the gain dropped by 3% after N<sub>2</sub> exposure, and by 7% after exposure to atmospheric air. Then it was transferred from the hydrogenation chamber to the gain test chamber in a nitrogen environment instead of exposing it to air. This did not change the reduction in gain before heating.

Next, a freshly hydrogenated diamond amplifier, only briefly exposed to the air, was installed in the test chamber. It was heated to 200°C under an ultrahigh vacuum (~10<sup>-10</sup> hPa), held there for 40 minutes, and then allowed to cool to room temperature. The gain at the center of the amplifier was 95. Heating it there after for 40 minutes at 350°C (the

limit in our test chamber) gave a gain of 135 at the same location upon cooling. This result shows that the optimum temperature for heat treatment is much higher than 200°C.

The diamond, which gain was 135, declined to 90 after one month operation (~90 hours). It cannot be recovered by heat up treatment and might be due to anode discharge or NEG outgassing. This diamond went through the re-hydrogenation process and achieved to gain of 130 without polishing the metal coating.

The experiments above show that the diamond is very robust when during transferring and operation. Even with the long time operation, the gain decrease can be recovered by the re-hydrogenation easily without complicated polishing and cleaning process.

### 5.2.3. Uniformity of secondary electron emission

The uniformity of secondary electron emission determines the transverse distribution of beam and beam's quality. Diamond amplifiers are drift-dominated cathodes, so the diameter of secondary electron beam reaching the emission surface is the same as that of the primary bunch. We measured the current from the anode while scanning the primary electron beam at metal coating side. Then the map of transverse emission distribution can be obtained.

The primary electron beam diameter was minimized to 350  $\mu\text{m}$  / 355  $\mu\text{m}$ . The metal coating area is 2.8 mm. The primary current was deflected by changing the deflecting voltage. Every step was 175  $\mu\text{m}$  in scan. For entire emission area, 361 data points was obtained. The entire diamond scan was repeated three times to eliminate the primary current vibration. The average gain map is shown in Figure 5.12

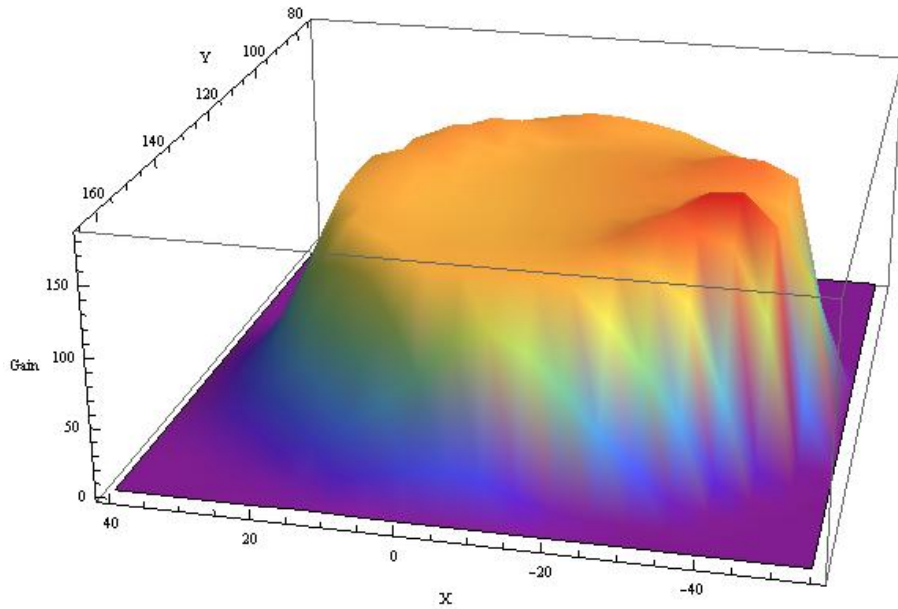


**Figure 5.12 Scan of the diamond amplifier’s secondary emission. The vertical axis Z is the gain number. X and Y are the coordinates of the position.**

The red color on the Figure 5.12 indicates the maximum gain location. The highest emission gain we measured was 178. The different gain at different locations within the whole piece could be due to the non-uniformity of the metal coating. The primary electrons will deposit part of their energy in the metal coating before penetrating the diamond. The lost energy varies with the thickness of the metal coating. The residual energy of primary electron affects the gain of the amplifier. Figure 5.13 shows the cross section of the gain distribution. The 96% uniformity was obtained if 0.5 mm edge area is disregarded.

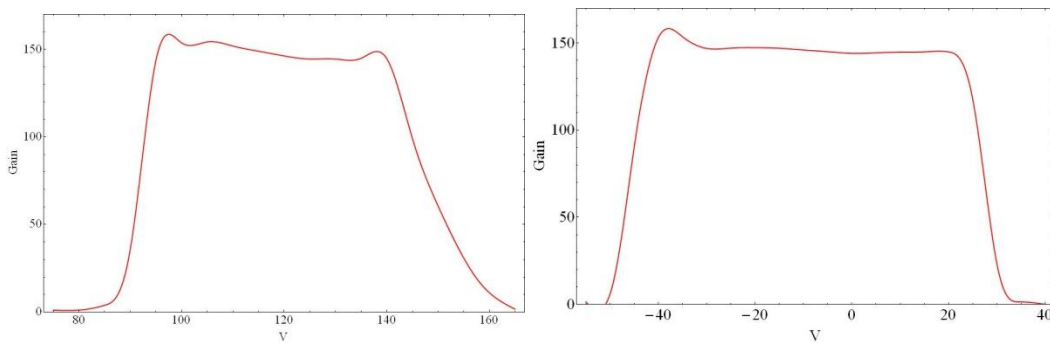


**Figure 5.13 The cross section of the gain distribution**

#### 5.2.4. Reproducibility

Our studies resulted in optimized parameters for hydrogenation and baking, giving us diamond samples with reproducible NEA surfaces, high QE, and high gain. We fabricated five more samples, and the gain in all of them reached more than 100. Figure 5.14 shows the gain in each of the five amplifiers we fabricated.

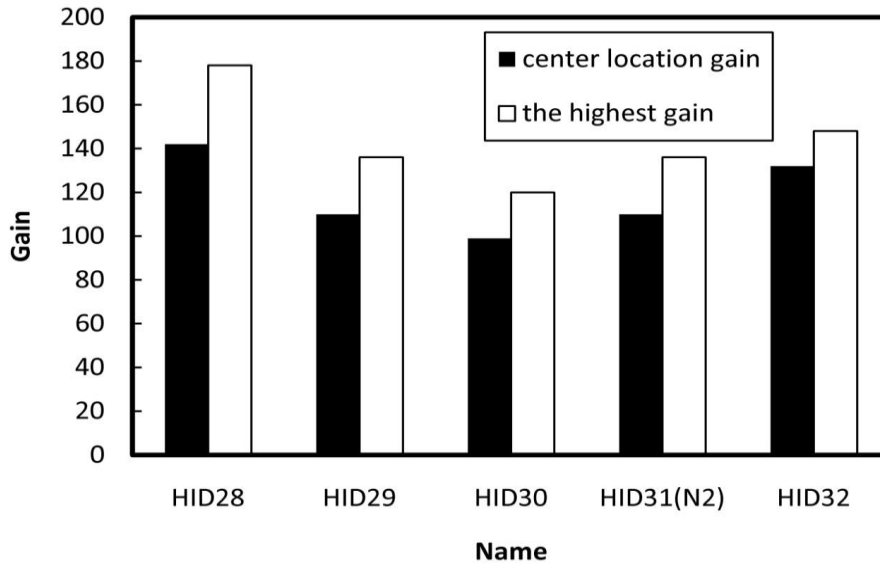


**Figure 5.14** The gain in five different diamond amplifiers. HID 31 was transferred in dry N<sub>2</sub> protection from the hydrogenation system to the gain test system. The black columns show the gain of the centers of the diamond amplifiers, and the white columns show the maximum gain on the samples.

### 5.3. Secondary electron surface trapping and emission

#### 5.3.1. Emission probability

The primary current, the primary electrons' energy, and the internal electric field determine the secondary electron current reaching the emission surface. In the following section, the model will be described to calculate the changes in the fields inside the diamond, and on the emission surface as a function of time due to the trapping of electrons, along with the impact of these changes on the fraction of the electrons emitted after arriving at the diamond's emission surface. We derived the time-dependent field inside the diamond as a function of instantaneous transmission gain and the emission

probability. The transmission gain was determined from earlier experimental data. The emission probability depends on the distribution of electron energy, and the surface potential barrier, which can be modified by the applied field and the field due to the image charges inside the diamond. The energy distribution and the surface barrier were calculated from the emission data from four samples. The time-dependent field, thus derived, was used to determine the instantaneous emission-current. The integrated emission current and average gain then were compared with the experimental results.

We start by defining various variables (Figure 5.15), wherein  $I_p$  is the DC primary current, and the generated average secondary electron current is  $I_s$ . The instantaneous secondary electrons current reaching the emission surface is  $I_i(t)$ . The instantaneous current emitted from the diamond is defined as  $I_e(t)$ . The measured average emission secondary electron current is

$$I_a = \frac{\int_0^w I_e(t) dt}{1/f} \quad (5.3)$$

where  $f$  is the pulse repetition frequency and  $w$  is the high voltage pulse width. The instantaneous transmission gain is defined as

$$G_t = \frac{I_i}{I_p}. \quad (5.4)$$

Further, define the average emission gain as

$$G_e = \frac{I_a}{I_p} \frac{1}{f \times w}. \quad (5.5)$$

We want to extract from the measurements of the average emission current  $I_a$  as a function of applied field and pulse length the instantaneous emission probability, defined as  $P = I_e/I_i$ . In a very short high-voltage pulse width ( $\ll \mu\text{s}$ ), when the density of the surface-trapped electrons is insufficient to shield the external field, the emission probability is equal to  $P = I_a/(I_i \cdot w \cdot f)$  or equivalently  $P = G_e/G_t$ .

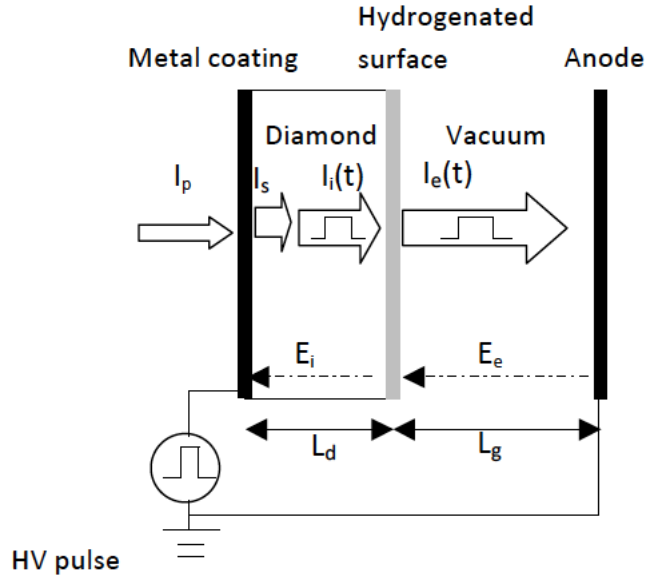


**Figure 5.15 The definitions of currents and fields in the diamond amplifier.**

### 5.3.2. Derivation of the time-dependent internal field

Based on these definitions, the time-dependent current of secondary electrons reaching the emission surface can be written as

$$I_i(t) = I_p \times G_t(E_p, E_i(t)) \quad (5.6)$$

where the transmission gain is a function of the energy of the primary electrons  $E_p$ , and the diamond's internal electric field,  $E_i$ . The time-dependence is induced by the variations in the internal electric field  $E_i(t)$  due to shielding by the trapped charge. The density of trapped electrons is given by

$$S(t) = \frac{1}{S} \int_0^t (1 - P) I_i(t) dt \quad (5.7)$$

where the  $S$  is the size of the secondary electron spot. Diamond amplifiers are drift-dominated cathodes, so the diameter of secondary electron beam reaching the emission surface of a thin diamond essentially is the same as that of the primary bunch, which we can measure experimentally.  $P$  is the emission probability, defined above.

The internal field is the vector sum of the external field and the field induced by the density of trapped electrons. For calculating the internal field in the surface-trapped diamond amplifier, we used the capacitor model. The internal field is given by

$$E_i(t) = \frac{E_e}{\varepsilon_r} - \frac{\sigma(t)}{\varepsilon} \quad (5.8)$$

Where  $E_e/\varepsilon_r$  is the internal field without surface trapping,  $\varepsilon_r$  is the relative permittivity of pure diamond and  $\varepsilon$  is the permittivity of the diamond. In our emission test setup, we applied a constant high voltage pulse to the diamond's metal coating, and the anode was grounded. The external field increases when the emission surface accumulates trapped secondary electrons. The external field is expressed by

$$E_e(t) = \frac{V - E_i(t) \times L_d}{L_g} \quad (5.9)$$

where  $V$  is the high voltage on the diamond's metal coating.  $L_d$  is the thickness of the diamond, and the  $L_g$  is the distance between the diamond's emission surface and the anode. The surface electron-trapping and the reduction in the internal field are described by

$$E_i(t) = \frac{E_e}{\varepsilon_r} - \frac{1}{\varepsilon \times S} \int_0^t (1 - P) \times I_p \times G_t(E_p, E_i(t)) dt \quad (5.10)$$

To solve this integral equation, we must know the amplifier's transmission gain  $G_t$  and the probability of emission  $P$ .

### 5.3.3. Transmission gain function

The transmission gain is defined as the ratio of the current of the secondary electrons reaching the emission surface to the primary-electron current. In our earlier transmission-mode experiment, we terminated both diamond surfaces with metal. Then, the measured transmission gain depends only on the primary electrons' energy and diamond's internal electric field [72]. The model of secondary electron generation and transmission in the diamond are discussed in the reference. However, the agreement with transmission experimental data is generally qualitative and not quantitative. In this paper, we find that

the gain fits rather well to a simple functional dependence, which includes the primary electron's energy and the field in the diamond as follows,

$$G_t(E_p, E_i(t)) = (a[1/keV]E_p[keV] - b)(1 - e^{-c[m/MV]E_i(t)[MV/m]}) \quad (5.11)$$

where  $E_p$  is the primary electron's energy, and  $E_i(t)$  is the time-dependent internal field. The points in Figure 5.16 show transmission gain as a function of internal field measured for a diamond sample. In the combined best fit of Eqn. 5.8 to the data, shown as solid lines in Figure 5.16, yields  $a = 52.5$ ,  $b = 173.2$ , and  $c = 4.1$ . If the curves are fitted individually, the coefficients  $a$  and  $b$  are the same as before and  $c$  is in the range from 4.1 to 4.4 for different primary electron energy but still within the experiment error. Therefore, we use the coefficients obtained from the combined best fit in the following simulations.

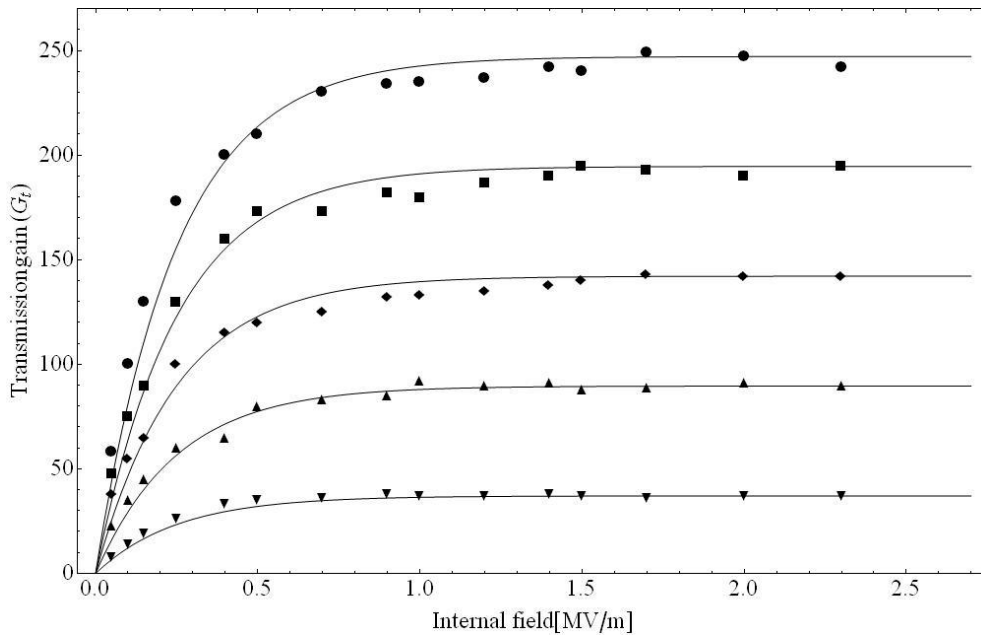


**Figure 5.16 Transmission gain ( $G_t$ ) curve of a synthetic high-purity single crystalline diamond. The points are the experiment results [72] and thin solid lines are the fitting function. The six lines response to the different primary beam energies.**

#### 5.3.4. Schottky effect on the effective negative electron affinity

The emission probability was obtained by using the Schottky model applied to the Negative Electron Affinity (NEA) of the hydrogenated diamond's surface. There are two

ways to model the NEA phenomenon; either in terms of true negative electron affinity or of effective negative affinity. The latter model is described as a combination of positive electron-affinity and the bending of the depletion band at the surface of the semiconductor. For true NEA, the vacuum level is lower than the minimum of the conduction band at the surface. Therefore, an electron at the Conduction Band Minimum (CBM) is free to leave the crystal because the barrier does not exist. In our experiment (measurements given below), we found that electrons are trapped at the emission surface, and furthermore, that the trapping rate is a function of the external field. The potential surface barrier prevent electrons with energy below this barrier from escaping the diamond and the modification of this barrier by the applied field changes the number of electrons that can escape, thus leading to a measurement of the electrons' energy distribution. This is in agreement with diamond (001)-(2x1):H surface structure calculation in other work [80].

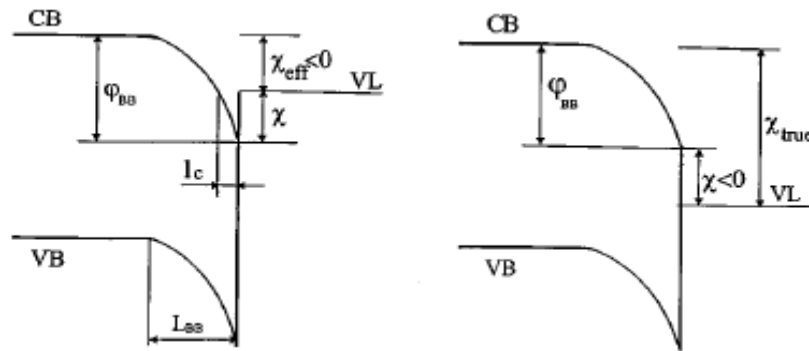


**Figure 5.17 The surface energy band of effective NEA and true NEA [81].**

We used four practically identical single-crystal, high-purity CVD diamonds [100] to fabricate four diamond amplifiers by applying a thin metal layer on one surface, and hydrogen termination of the other surface. The preparation of the amplifiers is detailed elsewhere [82].

We carried out the experiment by measuring the emission current as a function of the pulse's length and the strength of the applied field. Figure 5.18 shows the  $G_e/G_t$  of four diamonds as a function of the external field where we used a very small pulse width (200 ns). Under this very short pulse, and the primary current that we applied (200 nA),

the change in the internal field can be neglected, and the instantaneous emission probability,  $P$ , is equal to  $G_e/G_r$ .

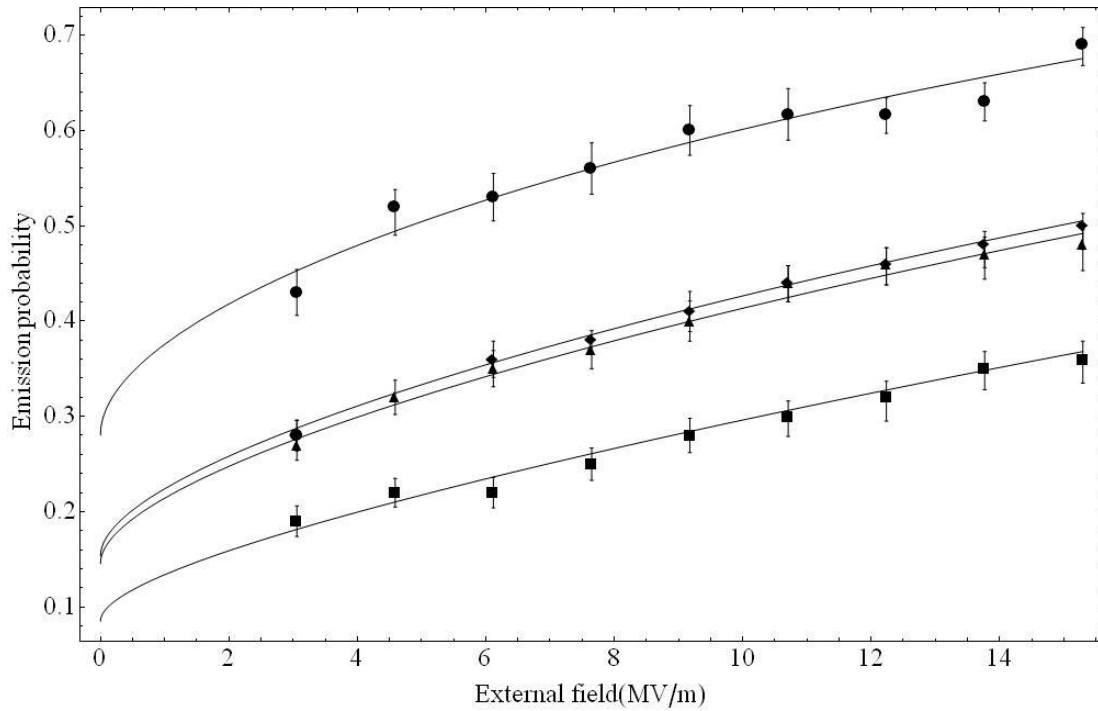


**Figure 5.18** The dependence of emission probability  $P$  on the external field when the pulse width is 200 ns. The points were measured from four different diamond samples. The four solid lines were generated by fitting to Eqn. 11, below.

We adopted the Schottky effect on the effective NEA surface to explain why emission probability depends on the external field. The diamond crystal is a dielectric. The external electric field and the force from image charges inside the diamond reduce the electron's potential energy according to the following expression [83].

$$V(x) = -\frac{e^2}{16\pi\epsilon_0} \left( \frac{\epsilon - \epsilon_0}{\epsilon + \epsilon_0} \right) \frac{1}{x} - eE_e x \quad (5.12)$$

where  $x$  is the distance from the emission surface,  $\epsilon$  is the permittivity of the diamond, and  $\epsilon_0$  is the permittivity of the vacuum. We compute the maximum value of the potential by setting  $dV(x)/dx$  to zero. The difference between the maximum value of the potential and the vacuum level then is given by

$$\phi_s = \sqrt{\frac{eE_e}{4\pi\epsilon_0} \left( \frac{\epsilon - \epsilon_0}{\epsilon + \epsilon_0} \right)} \quad (5.13)$$

The diamond's relative permittivity is 5.6, the Schottky potential simplifies to  $0.0318 (E_e(\text{MV/m}))^{0.5}$  [eV]. The Schottky effect reduces the surface potential barrier, thus allowing the emission of electrons with a lower energy. Figure 5.19 shows the diamond surface's band structure. As secondary electrons reach the emission surface, some get into the potential well between the conduction band and the Schottky potential. The minimum energy of the secondary electron is the same as that of the CBM at surface. We define  $\phi_I$  as the energy difference from the CBM to the vacuum level. The  $\phi_I$  reduce in the potential  $\phi_S$  due to Schottky effect. Electrons can escape the diamond either with energies great than  $\phi_I - \phi_S$ , or by tunneling through the barrier.

We find that fitting the current dependence on the applied field to an expression [84] used for tunneling does not lead to a good fit to the experimental data. On the other hand, we get a good fit making the assumption that only electrons above the Schottky barrier escape and neglecting tunneling altogether.

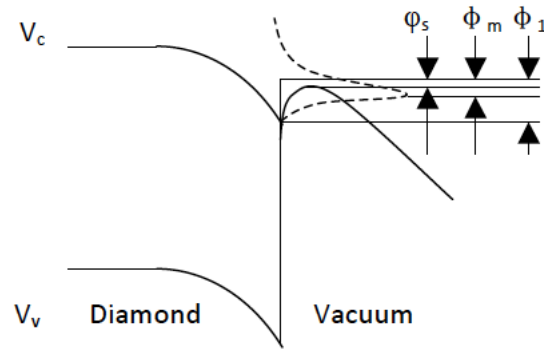


**Figure 5.19 Energy-level diagram of diamond amplifier/vacuum interface band structure. The dashed curve represents the internal distribution of the secondary electrons' energy.  $\phi_I$  is the energy difference from the CBM to the vacuum level and  $\phi_m$  is the energy difference between the mean of distribution of internal electron energy and the vacuum level.  $\phi_S$  is the reduction of the barrier by the applied field.**

### 5.3.5. Energy spread of secondary electron beam

The emission probability also is related to the energy distribution of electrons inside the diamond. This distribution is depends on the electron-transport process in the bulk. On the other hand, the energy distribution of the electrons emitted from a surface depends strongly on the position of vacuum level and the Schottky potential, which are related to the external field.

As a first approximation, we model the distribution of secondary electrons in diamond near the emission surface (close to the end of the band bending region) with a Gaussian given by

$$f(\varphi) = \frac{e^{-\frac{(\varphi-m)^2}{2\sigma^2}}}{\sqrt{2\pi\sigma^2}} \quad (5.14)$$

where  $\sigma$  is the variance, and we chose the mean as  $m$  relative to CBM at the surface.  $\varphi$  is taken as the energy above the CBM. For the electrons with energy lower than  $\varphi_l - \varphi_s$ , the probability of escape is assumed negligible.

Therefore, the probability of secondary-electron emission is

$$P = 1 - \int_{-\infty}^{\varphi_l - \varphi_s} f(\varphi) d\varphi \quad (5.15)$$

Combining equations 5.13-5.15 generates a simple expression for the emission probability in terms of the width of the energy distribution, the applied electric field, and the NEA:

$$P = 1 - \frac{1}{2} \text{Erfc}\left(\frac{\varphi_m + \varphi_s}{\sqrt{2}\sigma}\right) \quad (5.16)$$

where  $\varphi_m$  is the energy difference between the mean of distribution of internal electron energy and the vacuum level. The values of  $\sigma$  and  $\varphi_m$  now are found by fitting to the experimental data (Figure 5.18).

Since all four diamond samples were of the same thickness, crystal orientation, and purity, we assume that the internal distribution of secondary electrons is same in all of them under the same measurement conditions. However, the level of the NEA may differ among these samples, as is reflected by changes in  $\varphi_m$ . The internal energy-spread,  $\sigma$ , obtained from the best fit is  $0.12 \pm 0.01$  eV, in agreement with simulation showing that  $\sigma$

is 0.13 eV to 0.14 eV [85]. For the four diamonds, the values of  $\phi_m$  obtained from the fitting are -0.070 eV, -0.123 eV, -0.127 eV, and -0.165 eV. The vacuum level of the different samples might vary due to several effects, such as hydrogen coverage [81], surface-carbon orientation [86, 87], and the orientation of the C-H bond in the hydrogen-terminated surface [88]. Eqn. 5.16 gives the initial emission-probability response to the external field with a certain  $\sigma$  and  $\phi_m$ , regardless of how it is determined.

The band structure calculations of Watanabe et al. [89] shows that for applied fields lower than 10 MV/m, the normalized energy distribution per unit energy divided by the density of states (DOS) behaves as a non-normalized Boltzmann distribution with effective temperature (Figure 7(a) in their paper). However, their results are for electron transport in bulk diamond and do not take into account how the band bending region affects the distribution of electrons as a function of energy. We considered fitting the observed simulations data for the number of electrons per unit energy with a Boltzmann distribution times a model DOS given by  $\sqrt{E}$  but a better fit was obtained using a simple Gaussian distribution. A more detailed theoretical model is needed to obtain better understanding of the energy distribution of electrons near the emission surface that also takes into account the band bending effects.

### 5.3.6. Solving the Integral equation

Now that we have established the emission probability, Eqn. 5.10 can be solved numerically to obtain the pulse-length dependence of the emission current. The initial conditions we used in solving the equation are listed in Table 5.1.

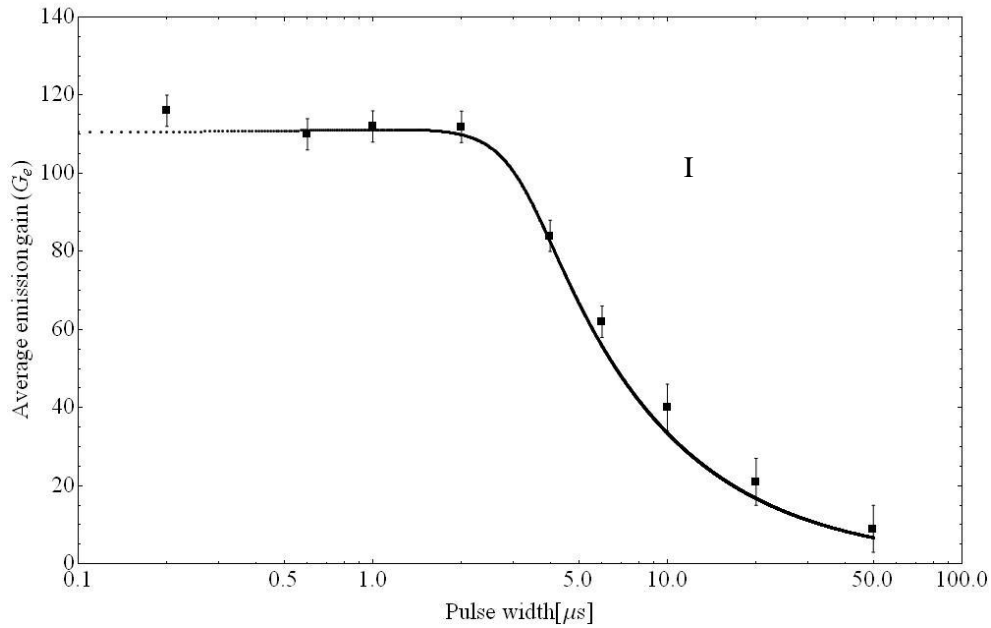
**Table 0.1 The initial parameters for solving Integral Equation 5**

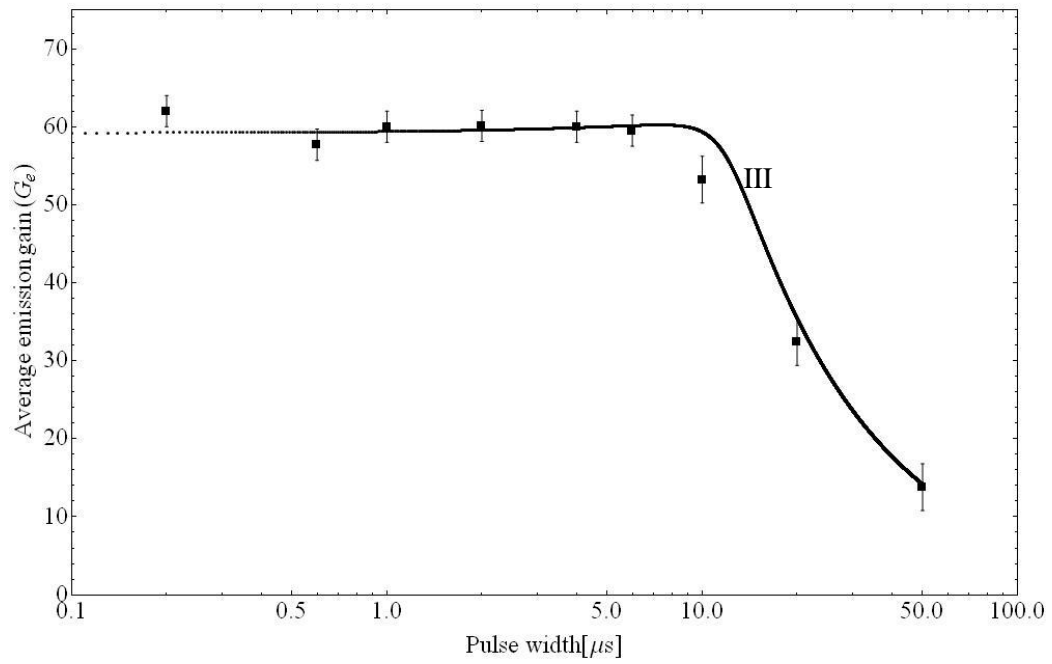
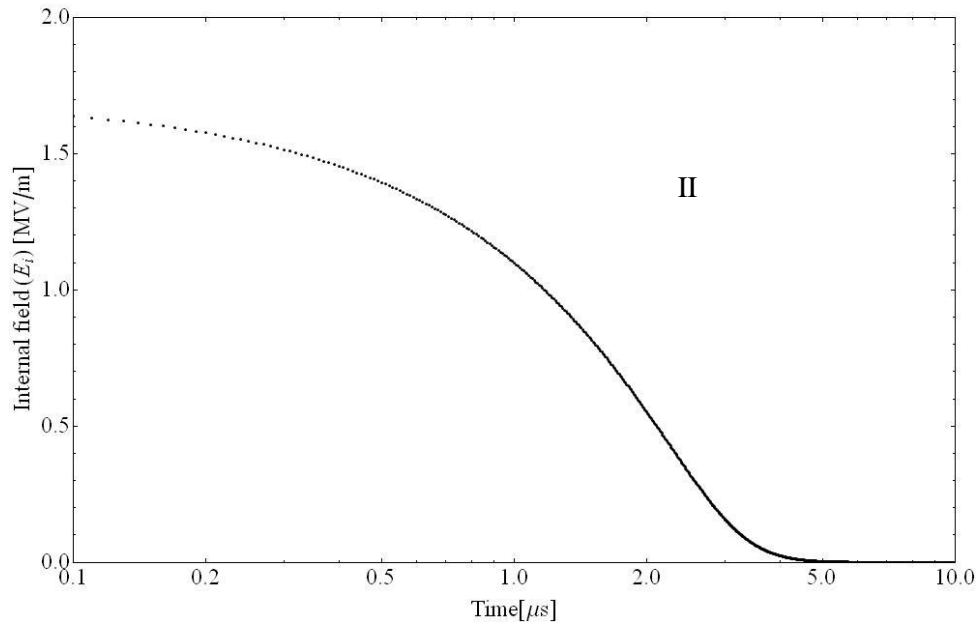
Spot Size	0.55 mm <sup>2</sup>
Voltage between metal coating and anode	3000, 5000 V
Frequency	1000 Hz
Diamond thickness ( $L_d$ )	300 $\mu$ m
Anode gap ( $L_g$ )	250 $\mu$ m
$\phi_m$	-0.07 eV
Primary current (DC)	200 nA

The measurable parameter in the experiment is the average secondary-electron emission current that engenders the average emission gain  $G_e$ . We obtain the average emission current by integrating the emission current over the pulse's width, and dividing this by the period:

$$I_a = \frac{\int_0^{width} I_p \times G_i(E_p, E_i(t)) \times P dt}{1/f} \quad (5.17)$$

We now insert the emission probability, Eqn. 5.16, and the transmission gain, Eqn. 5.8, into the integral Eqn. 5.10. The integral equation is solved numerically to generate the internal electric field as a function of time along the pulse length. Once this is known, average emission current and average emission gain can be calculated. Figures 5.20-I through 5.20-IV illustrate our results.





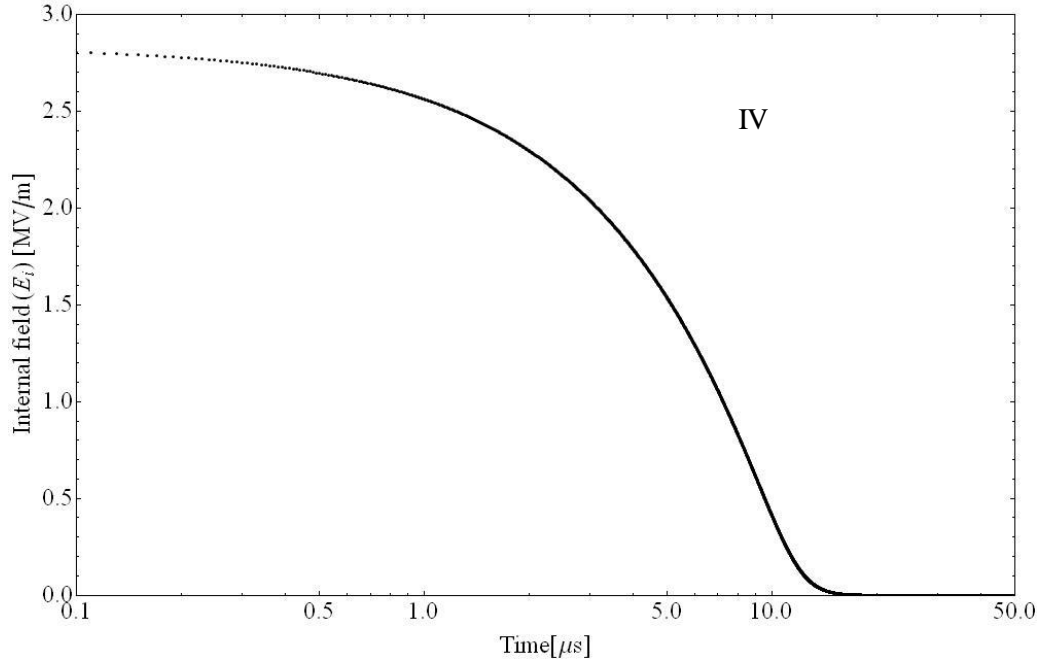


**Figure 5.20** The results of resolving equation (5). I and II, respectively are the average emission gain ( $G_e$ ), and the time dependence of internal field ( $E_i$ ) for an applied voltage of 3000 V. III and IV, respectively, are the average emission gain ( $G_e$ ), and the time dependence of internal field ( $E_i$ ) for an applied voltage of 5000 V. The solid squares are the experimental results accompanied by the estimated systematic error bars. The continuous curves are the solution of Eqn. 10.

We measured the sample wherein  $\varphi_m$  is -0.07 eV based on the initial conditions shown in Table 5.1. The set-up for measuring the secondary current is published elsewhere [78]. The normalized values for the secondary-electron emission gain, indicated by the points in Figure 5.20, match well the model's prediction.

The process leading to this behavior is a decrease of the internal field along the pulse's width due to the accumulation of trapped electrons on the surface and thus shielding of the external field. As the internal field decreases, the secondary electrons drift more slowly towards the emission surface and incur further recombination loss at the surface of the metal layer; therefore, the average emission-gain and normalized emission-rate decrease.

### 5.3.7. The energy spread due to the IMFP

The electron's energy spread near the emission surface is not determined by the energy of the nascent electrons; in drifting through the diamond, the electrons undergo a vast number of collisions, both elastic and inelastic. The energy spread of the electrons is the product of equilibrium between the small energy gain during their transit from the internal field, and their energy loss due to the frequent scattering they experience. The inelastic mean free path (IMFP) is energy-dependent; thus, the electric field affects the equilibrium temperature attained by the drifting electrons. The equilibrium value of random energy as a function of the inelastic mean free path is estimated as follows [90]:

$$\frac{1}{2} m V_e^3 = -e E v \lambda_i \quad (5.18)$$

where  $V_e$ ,  $m$ ,  $v$  and  $\lambda_i$  are, respectively, the electron's velocity, electron's effective mass, the electron's drift velocity and IMFP. The drift velocity is expressed by  $v = 10^5 \times (0.2 E_i[\text{MV/m}] + 0.55)$  [m/s]. For the IMFP, we use the semi-empirical formula of Seah and Dench

$$\lambda_i = [538 E_r^{-2} + 0.41 (x_m E_r)^2]^{-\frac{1}{2}} x_m \quad (5.19)$$

The  $x_m$  is the thickness of a monolayer in nanometers that, for diamonds, is 0.178 nm.  $E_r$  is the electrons' energy above the Fermi level and the units are eV. For the intrinsic diamond, the energy of the conduction band above the Fermi energy is 2.775 eV. By inserting Eqn. 5.19 into Eqn. 5.18, the equilibrium electron random energy is 0.04 eV, and IMFP is 12 nm when the internal field is 2 MV/m. This calculated random energy of the electron is much smaller than the measured width  $\sigma$  of the Gaussian distribution above the conduction band obtained from the Schottky model. Since the Seah and Dench model does not consider the band-bending region at the diamond's surface, the physics of the electron motion in this region offers an explanation for the discrepancy. The depth of the band-bending region was estimated from experiments to be about 0.1  $\mu\text{m}$  [85, 87], viz., several times larger than the IMFP. The electrons scatter with phonons and emit acoustic phonons several times in the varying energy level at the band-bending region. Meanwhile, since part of the electrons energy extends above 0.13 eV [89], optical phonon emission takes place in the band bending region. We propose these scattering to

be responsible for the increase in the electrons' energy spread inside the diamond and consider that the energy spread may be reduced by a modification of the length of the band-bending region.

The emission model currently implemented in the VORPAL code [85] considers only a stair-step potential at the emission surface. This is the simplest possible model for emission (and also the least complex to implement in the code). The results reported in [85] were with the stair-step model. The main deficiency of this model is that it does not take into account the effect of the applied field on the surface potential and thus is not expected to be accurate. We are currently exploring to add a more realistic surface potential in the simulation code and fully take into account the effect of applied field during emission.

Compared to the earlier model, there are three significant advances in this new model:

- i) The emission model derived by the VORPAL computational framework didn't consider the surface electron trapping which is described well in the model of this paper.
- ii) We observed experimentally that the emission probability depends on the external field. We introduce the Schottky effect on the effective NEA surface to explain this phenomenon, which cannot be explained by the model run in the VORPAL [85].
- iii) Some parameters such as  $\varphi_m$  and electron energy distribution of this emission model can be fitted by the experimental data from four diamond samples.

## Chapter 6. Conclusion

High quantum efficiency photocathodes has been identified as the most viable technology for high quality electron source for collider and light source in the future. Studies and tests of activated GaAs photocathode in SRF gun and studies of diamond amplifier are the central focus of this thesis.

By following building the UHV preparation chamber, the activity of GaAs cathode is satisfactory at BNL. Three different ways to activate the GaAs have been explored. With conventional activation of bulk GaAs, we obtained a QE of 10% at 532 nm with lifetime of more than 3 days in the preparation chamber and have shown that it can survive in load lock transport system from the preparation chamber to the gun.

A GaAs photocathode in the SRF gun was tested in the 2K. The results demonstrated the GaAs crystal generated the heat from the RF field. The heat load from the cathode reflects a combination of doping and dielectric heat load. My model shows that heavy doping generates much more heat than does dielectric tangent loss. Meanwhile, a recess photocathode holder was made to shield the sides of the bulk crystal from the RF field. Based on the simulation, the recess structure of cathode holder improves the quenching limit of the SRF gun.

The temporal response of GaAs photocathode is critical for use in the 1.3 GHz SRF gun. By solving the drift-diffusion equation, the tail of the electron bunch from GaAs photocathode that is a critical factor in the performance of a DC gun can be ignored in the RF gun.

Simulations of the multipacting effect on the NEA photocathode in the RF field reveals that the secondary electron emission yields which occur at different positions on the GaAs occasion different harmful effects on the Cs-O layer. To minimize the multipacting driven by the electron back bombardment, a procedure for judicious choice of the laser pulse with respect to the RF phase was proposed.

The effect of hydrogenation on the NEA surface of diamond amplifiers was studied systematically. The results revealed that high-temperature hydrogenation yields a higher quality NEA surface compared to the hydrogenation at room temperature. Hydrogenated diamond amplifiers are little affected by exposure to the atmosphere; any loss in electron yield can be recovered by subsequent heat treatment. The bake temperature was optimized to recover the maximum electron yield in both the hydrogenation chamber and in the test chamber. The treatments result in a reproducibly better performance of diamond amplifiers.

In the emission mode measurement, the continuous secondary electron beam was obtained. Following the procedure developed in this thesis, the gain of diamond amplifiers were all above 100 and the highest gain measured was 178. We measured the emission probability of the diamond amplifier as a function of the external field and modeled the process with the resulting changes in the vacuum level due to the Schottky effect. The effective NEA is deduced from the model and measurements. We demonstrated that the average decrease in the secondary-electrons' emission-gain was a function of the pulse width, and related this to the trapping of electrons by the effective NEA surface. Based on the measurement of four diamond samples with different

effective NEAs (but otherwise identical), the distribution of the secondary-electrons' internal energy,  $\sigma$ , was  $0.12 \pm 0.01 \text{ eV}$  in all four diamond samples.

## References:

- [1]. Pierce, D.T. and F. Meier, Photoemission of spin-polarized electrons from GaAs. Phys. Rev. B Physical Review B, 1976. 13(12): p. 5484.
- [2]. Poelker, M., et al., Polarized Source Performance and Developments at Jefferson Lab, in Workshop on Polarized Electron Sources and Polarimeters. 2000.
- [3]. Zwart, T., et al. Polarized electrons in the MIT-Bates South Hall Ring. in Particle Accelerator Conference, 2001. PAC 2001. Proceedings of the 2001. 2001.
- [4]. Aulenbacher, K., et al., Status of the polarized source at MAMI, in 15th International Spin Physics Symposium and Workshop on Polarized Electron Sources and Polarimeters. 2002.
- [5]. Sinclair, C.K., et al., Development of a high average current polarized electron source with long cathode operational lifetime. Phys. Rev. ST Accel. Beams, 2007. 10(2): p. 023501.
- [6]. Stutzman, M.L., et al., Characterization of the CEBAF 100 kV DC GaAs photoelectron gun vacuum system. Nuclear Instruments and Methods in Physics Research Section A: Accelerators, Spectrometers, Detectors and Associated Equipment, 2007. 574(2): p. 213-220.
- [7]. Garden, C.L., et al. Photocathode performance measurements for the SLC polarized electron gun. in Particle Accelerator Conference, 1993., Proceedings of the 1993. 1993.
- [8]. Poelker, M., et al., High Intensity Polarized Electron Sources. AIP Conference Proceedings, 2008. 980(1): p. 73-78.
- [9]. Liu, G., et al. Polarized electrons in the AmPS storage ring. in Particle Accelerator Conference, 1997. Proceedings of the 1997. 1997.
- [10]. Ptitsyn, V., et al., ERFIC Conceptual Design, in 42nd ICFA Advanced Beam Dynamics Workshop on High-Intensity, High Brightness Hadron Beams. 2008: Nashville, TN USA.
- [11]. ILC Reference Design Report. 2007.
- [12]. Ben-Zvi, I., Polarized Electron photocathode R&D at BNL, in Polarized Sources, Targets & Polarimetry 2009. 2009: Ferrara (Italy).
- [13]. Dowell, D.H., et al., Commissioning Results of the LCLS Injector, in 9th International Free Electron Laser Conference. 2007: Novosibirsk, Russia.
- [14]. Aleksandrov, A.V., et al. Experimental study of GaAs photocathode performance in RF gun. in Particle Accelerator Conference, 1999. Proceedings of the 1999. 1999.
- [15]. Fliller, R.P.I., et al., Progress on using NEA cathodes in an RF gun, in the proceedings of Particle Accelerator Conference (PAC 05). 2005: Knoxville, Tennessee.
- [16]. Clendenin, J.E., Development of a Polarized Electron Gun Based on an S-Band PWT Photoinjector. 2003, SLAC.
- [17]. Wang, J.W., et al., The RF Design of an HOM Polarized RF Gun for the ILC, in 2006 Linear Accelerator Conference. 2006: Knoxville, Tennessee.
- [18]. Todd, R., private communication.
- [19]. Xiang, R., et al., Cs<sub>2</sub>Te normal conducting photocathodes in the superconducting rf gun. Phys. Rev. ST Accel. Beams, 2010. 13(4): p. 043501.
- [20]. Neil, G.R., et al., Sustained Kilowatt Lasing in a Free-Electron Laser with Same-Cell Energy Recovery. Phys. Rev. Lett., 2000. 84(4): p. 662.
- [21]. Derbenev, Y. and A.N. Skrinsky, Sov.Phys.Rev, 1981(1): p. 165.
- [22]. I. Ben-Zvi, X.C., Secondary emission enhanced photoinjector. 2004, BNL.
- [23]. Togawa, K., et al. Pulsed hv electron gun with thermionic cathode for the soft x-ray FEL project at Spring-8. in Particle Accelerator Conference, 2003. PAC 2003. Proceedings of the. 2003.
- [24]. Akre, R., et al., Commissioning the Linac Coherent Light Source injector. Phys. Rev. ST Accel. Beams, 2008. 11(3): p. 030703.
- [25]. Dowell, D.H., et al., Cathode R&D for future light sources. Nuclear Instruments and Methods in Physics Research Section A: Accelerators, Spectrometers, Detectors and Associated Equipment, 2010. 622(3): p. 685-697.
- [26]. Wu, Q., Measurements and studies of secondary electron emission of diamond amplified photocathode. 2008, INDIANA UNIVERSITY.
- [27]. Oshiki, Y., et al., Saturation drift velocity measurement for CVD diamond by combination of a charge distribution measurement and a TOF method using a UV pulsed laser. Diamond and Related Materials, 2006. 15(10): p. 1508-1512.

- [28]. Xiangyun, C., et al. Recent progress on the diamond amplified photo-cathode experiment. in Particle Accelerator Conference, 2007. PAC. IEEE. 2007.
- [29]. Bohon, J., E. Muller and J. Smedley, Development of diamond-based X-ray detection for high-flux beamline diagnostics. 2010. 17(6): p. 711-718.
- [30]. Polarized RF Gun meeting Notes. 2005.
- [31]. Wang, X.J., et al., Experimental characterization of the high-brightness electron photoinjector. Nuclear Instruments and Methods in Physics Research Section A: Accelerators, Spectrometers, Detectors and Associated Equipment Proceedings of the 17th International Free Electron Laser Conference, 1996. 375(1-3): p. 82-86.
- [32]. Nakanishi, T., et al., Large enhancement of spin polarization observed by photoelectrons from a strained GaAs layer. Physics Letters A, 1991. 158(6-7): p. 345-349.
- [33]. Omori, T., et al., Large enhancement of polarization observed by extracted electrons from the AlGaAs-GaAs superlattice. Phys. Rev. Lett. Physical Review Letters, 1991. 67(23): p. 3294.
- [34]. Blakemore, J.S., Semiconducting and other major properties of gallium arsenide. J. Appl. Phys., 1982. 53: p. R123-R181.
- [35]. Kittel, C., Introduction to solid state physics. 2005: Wiley.
- [36]. S  ez, P.J., POLARIZATION AND CHARGE LIMIT STUDIES OF STRAINED GaAs PHOTOCATHODES. 1997, SLAC. p. 8-9.
- [37]. Spicer, W.E. and A. Herrera-Gomez. Modern theory and applications of photocathodes. in Photodetectors and Power Meters. 1993. San Diego, CA, USA: SPIE.
- [38]. Bell, R.L., Negative electron affinity devices [by] R. L. Bell. Monographs in electrical and electronic engineering. 1973, Oxford: Clarendon Press.
- [39]. Scheer, J.J. and J. van Laar, GaAs-Cs: A new type of photoemitter. Solid State Communications, 1965. 3(8): p. 189-193.
- [40]. Pierce, D.T., et al., The GaAs spin polarized electron source. Review of Scientific Instruments, 1980. 51(4): p. 478-499.
- [41]. Maruyama, T., et al., Systematic study of polarized electron emission from strained superlattice photocathodes. Applied Physics Letters, 2004. 85(13): p. 2640-2642.
- [42]. Grames, J., et al. Ion back-bombardment of GaAs photocathodes inside dc high voltage electron guns. in PAC 05. 2005. Knoxville, TN (US).
- [43]. Reiser, M., Theory and Design of Charged Particle Beams. 1999: Wiley-VCH.
- [44]. Pozdeyev, E., D. Kayran and V.N. Litvinenko, Cathode ion bombardment in rf photoguns. Phys. Rev. ST Accel. Beams Physical Review Special Topics - Accelerators and Beams, 2009. 12(4): p. 043501.
- [45]. Ben-Zvi, I., et al., AMPERE AVERAGE CURRENT PHOTOINJECTOR AND ENERGY RECOVERY LINAC, in 26TH INTERNATIONAL ERL CONFERENCE. 2004: TRIESTE (IT).
- [46]. RUNNING EXPERIENCE OF FZD SRF PHOTOINJECTOR, in FEL 2009. 2009: Liverpool, UK.
- [47]. Chang, X., et al., Emittance compensation of compact superconducting guns and booster linac system. Phys. Rev. ST Accel. Beams, 2006. 9(4): p. 044201.
- [48]. Cole, M., et al. RF Design and Operating Performance of the BNL/AES 1.3 GHz Single Cell Superconducting RF Photocathode Electron Gun. in Particle Accelerator Conference, 2005. PAC 2005. Proceedings of the. 2005.
- [49]. Hasan Padamsee, J.K., RF Superconductivity for Accelerators. 2008: Wiley-Vch.
- [50]. Powers, T., Theory and Practice of Cavity RF Test Systems, in 12th International Workshop On RF Superconductivity. 2006: Ithaca, New York.
- [51]. Chen, K.X., et al., Four-point probe measurement of semiconductor sheet resistance.
- [52]. Rogers, C.B., G.H.B. Thompson and G.R. Antell, DIELECTRIC CONSTANT AND LOSS TANGENT OF SEMI-INSULATING GaAs AT MICROWAVE FREQUENCIES. Applied Physics Letters, 1967. 11(11): p. 353-354.
- [53]. Metaxas, A.C., Foundations of electroheat: a unified approach. 1996: Wiley.
- [54]. R. Xiang, A.A.P.M., Low Emittance Polarized Electron Source Based on FZD Superconducting RF Gun., in SRF2007. 2007: Beijing, China.
- [55]. Hartmann, P., et al., Picosecond polarized electron bunches from a strained layer GaAsP photocathode. Nuclear Instruments and Methods in Physics Research Section A: Accelerators, Spectrometers, Detectors and Associated Equipment, 1996. 379(1): p. 15-20.

- [56]. Bazarov, I.V., et al., Thermal emittance and response time measurements of negative electron affinity photocathodes. *Journal of Applied Physics*, 2008. 103(5): p. 054901.
- [57]. C, C.P.E.A., Quantitative XPS surface chemical analysis and direct measurement of the temporal response times of glass-bonded NEA GaAs transmission photocathodes. *Journal of Physics D: Applied Physics*, 1984. 17(8): p. 1713.
- [58]. Blakemore, J.S., Semiconducting and other major properties of gallium arsenide. 1982. 53(10): p. 123-181.
- [59]. J. Pozhela, A.A.R., Electron transport properties in GaAs at high electric fields, in *Solid State Electron*. 1980. p. 927-933.
- [60]. Liu, H., Simulation studies on back bombardment of electrons in rf thermionic guns. *Nuclear Instruments and Methods in Physics Research Section A: Accelerators, Spectrometers, Detectors and Associated Equipment*, 1991. 302(3): p. 535-546.
- [61]. Baptiste, K., et al., A CW normal-conductive RF gun for free electron laser and energy recovery linac applications. *Nuclear Instruments and Methods in Physics Research Section A: Accelerators, Spectrometers, Detectors and Associated Equipment*, 2009. 599(1): p. 9-14.
- [62]. Hartung, W., et al. Studies of photo-emission and field emission in an rf photo-injector with a high quantum efficiency photo-cathode. in *Particle Accelerator Conference, 2001. PAC 2001. Proceedings of the 2001. 2001.*
- [63]. Hui-Han, J., et al., Dark Current and Multipacting in the Photocathode RF Guns at PITZ. 2005.
- [64]. Kewisch, J., et al., An SRF Injector for the ILC. 2009, SLAC National Accelerator Laboratory.
- [65]. Kobashi, K., *Diamond films: chemical vapor deposition for oriented and heteroepitaxial growth*. 2005: Elsevier.
- [66]. Sque, S., in <http://newton.ex.ac.uk/research/qsystems/people/sque/diamond/structure/>.
- [67]. Calzaferri, G. and R. Rytz, The Band Structure of Diamond. 1996. 100(26): p. 11122-11124.
- [68]. Ben-Zvi, I., et al.. 2004, Brookhaven National Laboratory: Upton.
- [69]. Chang, X., *Studies in Laser Photo-cathode. RF Guns*. 2005, Stony Brook University.
- [70]. Chang, X., et al. Measurement of the Secondary Emission Yield of a Thin Diamond Window in Transmission Mode. in *Proceedings of the PAC 2005*. 2005.
- [71]. Chang, X., et al., Electron Beam Emission from a Diamond-Amplifier Cathode. *Physical Review Letters*, 2010. 105(16): p. 164801.
- [72]. Chang, X., et al. Recent Progress on the Diamond Amplified Photo cathode Experiment. in *Proceedings of 2007 Particle Accelerator Conference*. 2007. Albuquerque, NM, USA.
- [73]. Qiong, W., *Measurements and Studies of Secondary Electron Emission of Diamond Amplified Photocathode*. 2008, Indiana University.
- [74]. in <http://www.mantisdeposition.com/ThermalGasCrackershome.htm>.
- [75]. Piantanida, G., et al., Effect of moderate heating on the negative electron affinity and photoyield of air-exposed hydrogen-terminated chemical vapor deposited diamond. *J. Appl. Phys.*, 2001. 89(12): p. 8259-8264.
- [76]. Kimball Physics, I., EGG-3101/EGPS-3101. 2004.
- [77]. GmbH, B.P.E., *Fast High Voltage Transistor Switches*. 2009.
- [78]. Chang, X., et al. First Observation of an Electron Beam Emitted from a Diamond Amplified cathode . in *PAC09, May 4-8. 2009. Vancouver, B.C., Canada*.
- [79]. Chang, X., et al., Electron Beam Emission from a Diamond-Amplifier Cathode. *Phys. Rev. Lett.*, 2010. 105(16): p. 164801.
- [80]. Sque, S.J., R. Jones and P.R. Briddon, Structure, electronics, and interaction of hydrogen and oxygen on diamond surface. *Physical review B*, 2006. 73(085313): p. [15 pages].
- [81]. Krainsky, I.L. and V.M. Asnin, Negative electron affinity mechanism for diamond surfaces. *Applied Physics Letters*, 1998. 72(20): p. 2574-2576.
- [82]. Wang, E., et al., Systematic study of hydrogenation in a diamond amplifier. *Physical Review Special Topics - Accelerators and Beams*, 2011. 14(6): p. 061302.
- [83]. Jackson, J., *Classical Electrodynamics Third Edition*. 1998: Wiley.
- [84]. Fowler, R.H. and L. Nordheim, Electron Emission in Intense Electric Field, in *Proc. R.Soc. Lond.* A May 1. 1928. p. 173-181.

- [85]. Dimitrov, D., R. Busby and D. Mithe, Modeling and simulations of electron emission from diamond-amplified cathodes, in Proceedings of 2011 Particle Accelerator Conference. 2011: New york, NY, USA, WEP161.
- [86]. Furthmuller, J., J. Hafner and G. Kresse, Dimer reconstruction and electronic surface states on clean and hydrogenated diamond (100) surfaces. Physical Review B, 1996. 53(11): p. 7334.
- [87]. Maier, F., J. Ristein and L. Ley, Electron affinity of plasma-hydrogenated and chemically oxidized diamond (100) surfaces. Physical Review B, 2001. 64(16): p. 165411.
- [88]. Zhang, Z., M. Wensell and J. Bernholc, Surface structures and electron affinities of bare and hydrogenated diamond C(100) surfaces. Physical Review B, 1995. 51(8): p. 5291.
- [89]. Watanabe, T., et al., Monte Carlo simulations of electron transport properties of diamond in high electric fields using full band structure. Journal of Applied Physics, 2004. 95(9): p. 4866-4874.
- [90]. Rao, T., et al., Diamond Amplifier For Photocathodes, in American Institute of Physics Conference Proceedings 737. 2004. p. 178-190.

## Acknowledgements

I sincerely appreciate the support and criticism given by the people from SRF group of Peking University and from Brookhaven National Laboratory (BNL). Without their help, this thesis could not be done.

In the first place, I would like to thank my supervisor Professor Kui Zhao for his guidance and expert advice during my early stage of SRF accelerator career. He gave me very good opportunity to experience the researches at KEK of Japan and BNL of USA. His diligence, experiences and passion always inspired me. I am honored to become one of his students and would like to give him respect and appreciate.

My Ph.D research has done at BNL. I would especially like to appreciate my local supervisor in BNL Professor Ilan Ben-zvi for providing such interesting projects to work on. As an experienced and genuinely talented scientist, he advised and discussed the problem along with me in detail with patience. He also modified and edited all my papers from language, layout to expression. I believe the benefit I received from him will continue on.

I would like to thank Dr. Jorg Kewisch and Dr. Xiangyun Chang for their guidance from theory and experiments. It is very pleased working with them. They gave the author lots of advices on this thesis.

Prof. Sergey Belomestnykh needs a special mention, I cannot thank him enough for the advices on the experiments and the thesis modifying and editing. Prof. Xiangyang Lu and Prof. Baocheng Zhao gave me many helps and advices on researches. I am grateful for the numerous illuminating discussions with them.

I would like to acknowledge Prof. Jiaer Chen and Prof. Kexin Liu for their regards along the author's researches. Particularly, thanks to Prof. Kexin Liu for his suggestions on this thesis writing.

I would also like to give my special thanks to Dr. Qiong Wu, Dr. Triveni Rao, Dr. Andrew Burrill, Dr. John Smedley, Dr Brian Sheehy, Dr Erik Muller, Dr. Yue Hao, Mr. Dave Pate, Dr. Guimei Wang, Dr. Chuyu Liu, Houjun Qian, Chaofeng Mi, Tianmu Xin who contribute in my studies and researches in BNL.

I would also thank to Dr. Shenwen Quan, Dr. Jiankui Hao, Lifang Wang, Dr. Shenlin Huang, Dr. Fen Zhu, Linlin, Dr. Fang Wang, Dr. Liming Yang, Dr. Fei Jiao who give me many suffusions during my first two year of Ph.D student in PKU. And I also like thank to all the students in the SRF group of PKU.

Lastly, I would like to thank my parents, my wife and son who are always there for me with encouragement and love.

## **CURRICULUM VITAE**

**Wang Erdong**

**PH.D In Physics, China**

Work address:

Bldg 911C Brookhaven national lab, Upton 11973, NY, USA

Phone: 631-344-8023(Office)

E-mail: [wedwrd@gmail.com](mailto:wedwrd@gmail.com)

[wange@bnl.gov](mailto:wange@bnl.gov)

### **EDUCATION**

9/2006-1/2012 Peking University, School of physics

Nuclear techniques and applications

Ph.D in physics

**THESIS: "High quantum efficiency photocathode for use in superconducting RF gun"**

9/2002-7/2006 Central University for Nationalities

School of physics and electronic technology;

B.Sc. in physics

Honor: Excellent Graduate of Beijing

1/2008-4/2008 Japan, High Energy Accelerators Research Organization(KEK).

Superconducting RF Test Facility for ILC group as research scholar.

9/2008-9/2011USA, Brookhaven National Lab Collide Accelerator Department  
as a exchange student.

### **PROFESSIONAL EXPERIENCE**

#### **9/2008-Present Brookhaven National Laboratory Collider Accelerator Department**

- Built a UHV vacuum preparation chamber and individually made the GaAs photocathode for the SRF gun. The highest QE of the photocathode reach to 10% @ 532nm laser.
- Tested the SRF gun in 2K and measured the heat generation of GaAs crystal in the SRF gun. Individually modeling GaAs crystal heat load in the RF field and design a new photocathode holder which minimize photocathode heat load in RF field.
- Wrote a differential equation and got the limitation of bunch length from GaAs photocathode in RF gun.
- Wrote a single particle tracking program which consider the electron drift in the GaAs crystal to simulate the electron back bombardment in the RF gun

- Tested the LLRF circuit to use in 2k GaAs SRF gun test with beam load.
- Studied the techniques of hydrogen termination for the diamond sample surface. Got a diamond amplify sample which secondary electron gain is over 178 which is the highest number we have ever got.
- Made a model to explain the electron emission from NEA cathode and estimated the electrons bunch energy spread.
- Did the diamond transmission mode measurement at beamline U13 and X15 of NSLS.
- Cooperating with other scientists on K<sub>2</sub>CsSb photocathode evaporation.

#### **10/2005-9/2008 Peking University and KEK**

- Elegant simulation chicane Magnet compressor for PKU-THz project (undergraduate thesis topic)
- Developed a new SRF cavity surface treatment method called Buffered Electro-polishing and got very good results.
- Higher order modes measurement on 2 cells SRF cavity. Design and made a coaxial line to measure the **higher order modes coupler RF characteristic.**
- Higher order modes coupler design and 9 cells ILC cavity tuning.

#### **TEACHING EXPERIENCE**

- 9/2007-1/2008 Teaching assistant of 6 undergraduate physics lab courses at Peking University. Duties cover explaining the experiment purpose and principle, solving real-time individual difficulties and grading the lab report.

#### **COMPUTER SKILL**

- Experienced in scientific software: Mathematica, Superfish, CST microwave studio, parmela, Astra, ANSYS, Solidworks, Autocad.
- Familiar with Elegant, Labview, CST particle studio.

#### **TALKS**

- Invited talk at IHEP(Institute of High Energy Physics),4/2008, Host: Prof. Gao Jie "ILC SRF baseline cavity developing at KEK and electro-polishing developing at Peking University"
- Invited talk at TSU(Tsing hua University), 11/2011, Host:Prof. Huang Wenhui "Diamond amplifier photocathode"
- Invited talk at IHEP(Institute of High Energy Physics),11/2011, Host: Dr. Wang Guangwei "Polarized electron SRF gun"
- Invited talk at SINAP(Shanghai Institute Of Applied Physics Chinese Academy Of Sciences),1/2012,Host: Dr. Gu Qiang "Diamond amplifier photocathode"

#### **PUBLICATIONS**

1. **Erdong Wang**,Ilan Ben-zvi et al  
Systematic study of hydrogenation in a diamond amplifier

**Phys. Rev. ST Accel. Beams** 14, 061302 (2011)

2. **Erdong Wang**, Ilan Ben-zvi et al  
Secondary-electron emission from hydrogen terminated diamond: Experiments and model

**Phys. Rev. ST Accel. Beams** 14,111301 (2011)

3. **Erdong Wang** , F. Wang , B.Zhang, et al  
Stop band character of TESLA cavity's coaxial-type HOM coupler  
**Chinese Physics C** 33 401

4. **Erdong Wang**, Jorg Kewisch, Ilan Ben-zvi et al  
Heat load of A GaAs photocathode in an SRF electron gun  
**Chinese physics C**, 35 387

5. Xiangyun Chang, Qiong Wu, Ilan Ben-Zvi, Andrew Burrill, Jorg Kewisch, Triveni Rao, John Smedley, **Erdong Wang**, Erik M. Muller, Richard Busby, and Dimitre Dimitrov  
Electron Beam Emission from a Diamond-Amplifier Cathode  
**Phys. Rev. Lett.** **105**, 164801

6. **Erdong Wang** , T. Xing , X. Lu , L.Yang ,L. Lin, et al,SRF 2007  
Study on the buffered electropolishing Jacquet layers on niobium cavity  
SRF2007 BeiJing,China,October 2007,

7. **Erdong Wang**, Jorg Kewisch,Ilan Ben-zvi et al  
Quantum Efficiency, Temporal Response and Lifetime of *GaAs* cathode in SRF Electron Gun  
IPAC'10 Kyoto,May 23-28.2010

8. **Erdong Wang**, Jorg Kewisch, Ilan Ben-zvi et al  
Heat load of a p-doped GaAs photocathode in an SRF electron gun  
IPAC'10 Kyoto,May 23-28.2010

9. **Erdong Wang**, Jinsong Wang,Ilan Benzvi  
Characterization of an SRF Gun:A fullwave simulation  
PAC11 Newyork Mar 30-Apr 2.2011

10. **Erdong Wang**, Xiangyun Chang,Ilan Benzvi  
Progress on diamond amplified photocathode  
PAC11 Newyork Mar 30-Apr 2.2011

11. **Erdong Wang**, Jorg Kewisch ,Ilan Ben-zvi et al  
Testing a GaAs cathode in SRF gun  
PAC11 Newyork Mar 30-Apr 2.2011
  
12. I.Ben-zvi, Andrew Burrill...**Erdong Wang**...et al  
Polarized electron photocathode R&D at BNL  
PST2009 September 07-11,2009
  
13. J.Smedley,T. Rao,**Erdong Wang**  
K<sub>2</sub>CsSb cathode development  
18<sup>th</sup> Int'l Spin physics symp pp.1062-1066(2009)
  
14. Jorg Kewisch , I.Ben-zvi...**E.Wang**.et al  
An Experiment to Test the Viability of a GaAs Cathode in a SRF Electron Gun,  
PAC 09 Vancouver,B.C.,Canada May4-8,2009
  
15. X.Chang, I.Ben-Zvi...**E.Wang** et al,  
First observation of an electron beam emitted from a diamond amplified cathode  
PAC 09 Vancouver,B.C,Canada May4-8,2009
  
16. Xiangyun Chang, Ilan Ben-zvi... **Erdong Wang** et al  
Rotating dipole andquadrupole field for a multiple cathode system  
PAC11 newyork Mar 30-Apr 2.2011
  
17. Jangho Park, Ilan Benzvi,...**Erdong Wang**  
Status of the polarized SRF photocathode Gun Design  
PAC11 newyork Mar 30-Apr 2.2011
  
18. Dimitre Dimitrov, Ilan Benzvi... **Erdong Wang**  
Modeling and simulations of electron emission from diamond amplified cathodes  
PAC11 newyork Mar 30-Apr 2.2011
  
19. Xiangyun Chang,Ilan Ben-zvi,...**Erdong Wang**  
A multiple cathode gun design for the eRHIC polarized electron source  
PAC11 newyork Mar 30-Apr 2.2011
  
20. Dimitre Dimitrov, Richard Busby...**Erdong Wang**  
Simulations of surface effects and electron emission from diamond amplifier cathodes  
IPAC11 San Sabastian, Spain, Sep.4-Sep.9,2011
  
21. Tianmu Xin,Ilan Ben-zvi...**Erdong Wang**, et al

Design of the fundamental power coupler and photocathode inserts for the 112MHz superconducting electron gun  
SRF2011 Chicago,USA,July 25-29,2011

22. Triveni Rao, Sergey Belomestnykh...**Erdong Wang**, et al  
Progress at BNL towards development of efficient, robust photocathodes for high average current operation  
ERL2011 KEK,Japan, 16-21October,2011

23. C.Liu, F.Wang, **Erdong Wang**, S.Quan, et al  
Impact on the magnetic compressor due to CSR  
Chinese Physics C, 2008 32 (08): 665—667

24. Wang fang, **Wang Erdong**, Zhang Baocheng, Zhao kui  
Measuring the performance of the coaxial HOM coupler on a 2-cell TESLA shape copper cavity  
Chinese Physics C 2009 33 (06): 440-443

25. Wang Fang, Lu Xiang-Yang, **Wang Er-Dong** and Zhao Kui  
Study on the RF performance of 2-cell superconducting cavity  
Chinese physics C 2009 33 74

26. Lu xiangyang, Quan shengwen, ...**Wang Erdong** et al,  
The First Nine-Cell TESLA cavity made in China  
CHIN.PHYS.LETT. Vol.25,No.11(2008)3940

27. Song jin, Lin lin, Limin Yang,**Erdong Wang** Xiangyang Lu, Kui Zhao  
Niobium sample surface treatment by buffered electropolishing ;  
Proceedings of SRF 2007, Beijing ,China